

AN ABSTRACT OF THE DISSERTATION OF

Martín Hoecker-Martínez for the degree of Doctor of Philosophy in
Ocean, Earth, and Atmospheric Sciences presented on August 20, 2015.
Title: Turbulence and biophysical fluxes in the near surface ocean.

Abstract Approved:

William D. Smyth

Vertical transports of plankton, momentum, heat, and turbulence are modeled. A novel integration of high resolution turbulence and biophysical modeling is used to show the influence of a Kelvin-Helmholtz instability on the vertical migration of simple gyrotactic organisms. A viscous limit on mixing driven by shear turbulence is proposed. Large eddy simulations are used to investigate the developing turbulence under a strong westerly wind burst observed in the equatorial Indian ocean.

©Copyright by Martín Hoecker-Martínez
August 20, 2015
All Rights Reserved

Turbulence and biophysical fluxes in the near surface ocean

by
Martín Hoecker-Martínez

A DISSERTATION
submitted to

Oregon State University

in partial fulfillment of
the requirements for the
degree of

Doctor of Philosophy

Presented August 20, 2015
Commencement June 2016

Doctor of Philosophy dissertation of Martín Hoecker-Martínez presented August 20, 2015.

APPROVED:

William D. Smyth, representing Ocean, Earth, and Atmospheric Sciences

Dean of the College of Earth, Ocean, and Atmospheric Sciences

Dean of the Graduate School

I understand that my dissertation will become a part of the permanent collection of Oregon State University libraries. My signature below authorizes release of my dissertation to any reader upon request.

Martín Hoecker-Martínez, Author

ACKNOWLEDGEMENTS

Thank you to my committee members past Kelly Benoit-Bird, Debora Pence, Souabh Apte, and Murray Levine as well as present Martin Storksdieck, Jim Moum, Simon DeSzorke, Kip Shearman, Eric Skyllingstad, and my adviser Bill Smyth for helping me form this amalgam of ideas. My work benefited tremendously from the weekly meeting organized by Alexander Kurapov, and attended by Roger Samelson, Bob Miller, Jon Osborne, Rodrigo Duran, and the others who gave up their lunch to discuss modeling. CEOAS support staff and faculty Lori Heartline, Mary Hitch, Linda Lamb, and Tom Leach among others helped keep the wheels greased, the ink flowing and the power on. My prose benefited from the comments and proof reading of Ata Suanda, Robert Ireland, Peter Gaube, Aurélie Moulin, and others. I am grateful to the CEOAS faculty for helping me refine my understanding of abstruse oceanographic and atmospheric phenomena. Thanks to my wife Beth and daughter Lucila for their constant love, support and understanding.

TABLE OF CONTENTS

	<u>Page</u>
1 Introduction	1
1.1 The Mixed Layer	1
1.2 Forcing	1
1.3 Stratification	3
1.4 Turbulence Transition	7
1.4.1 Turbulence and Motile Organisms	7
1.5 Scale Separation	10
2 Trapping of gyrotactic organisms in an unstable shear layer	13
2.1 Introduction	14
2.2 Methods	17
2.2.1 Flow model	17
2.2.2 Biological modeling	18
2.2.3 Simulation parameters	26
2.3 Results	26
2.3.1 Particle tracking results	26
2.3.2 Continuum model results	30
2.3.3 Pathways to trapping	30
2.3.4 Model comparison	33
2.3.5 Dependence of aggregation rate on initial conditions	35
2.4 Discussion	35
3 Kelvin-Helmholtz Overturn Boundary in Viscous Flows	39
3.1 Introduction	39
3.2 Idealized Shear Layer	40
3.3 The Instability	43
3.3.1 Overturns	43
3.3.2 Initial Perturbations	43
3.3.3 Limiting Cases	44
3.4 Conclusions	46
4 Oceanic Turbulent Energy Budget using Large Eddy Simulation of a wind event during DYNAMO	47
4.1 Introduction	48
4.2 Initial ocean state and air-sea fluxes during the wind burst	52
4.3 The LES Model	57
4.4 Simulation Results	58
4.4.1 Spatial Organization of Turbulence	58
4.4.2 Turbulent Kinetic Energy	59
4.4.3 Marginal shear instability below the mixed layer	66
4.4.4 Turbulent Fluxes	70
4.5 Comparison with the COARE wind burst	75
4.6 Conclusions and Discussion	76
5 Conclusions	78

TABLE OF CONTENTS (CONTINUED)

5.1 Biological Convergence	78
5.2 Instability and Turbulence	79
Bibliography	80
Appendices	90
A Trapping of gyrotactic organisms in an unstable shear layer	91
B Large Eddy Simulation Turbulence Closure	100
C Eddy Perturbations on Ekman Pumping	102
D Front Tracking	107

LIST OF FIGURES

Figures	Page
1.1 Mixed Layer Depth in January, April, July, and October	2
1.2 Maximum stratification in January, April, July, and October	5
1.3 Depth of maximum stratification in January, April, July, and October	6
1.4 Maximum stratification in January, April, July, and October	8
1.5 Maximum stratification in January, April, July, and October	9
2.1 Forces acting on a gyrotactic organism	19
2.2 Steady state profiles	22
2.3 Initial simulation parameters	25
2.4 Particle positions and orientations	27
2.5 Gyrotactically trapped organism track	28
2.6 Trajectory of a vortex trapped organism	29
2.7 Concentration and orientation field	31
2.8 Mean concentration field	32
2.9 Concentration in horizontally averaged bins	34
2.10 Aggregation rates	36
3.1 Background flow profiles	42
3.2 Limiting curves for K-H overturns	45
4.1 Schematic of the upper ocean forcing and mixing processes	50
4.2 Upper ocean conditions prior to the wind burst	54
4.3 Surface fluxes used as upper boundary condition for LES	55
4.4 Stokes drift, Buoyancy fluxes, Hoenikker number and Langmuir number	56
4.5 Surface stress, $\langle tke \rangle_{x,y,z}$, and w snapshot	60
4.6 Turbulent kinetic energy and depth averaged sources and sinks	63
4.7 Sources and sinks of turbulent kinetic energy	64
4.8 Turbulent kinetic energy and fluxes	65
4.9 Isopycnals, stratification, shear, and Richardson number	67
4.10 Distributions of Richardson number	69
4.11 Resolved heat flux, temperature, mixed layer depth	72
4.12 Resolved salt flux, salinity, mixed layer depth	73
4.13 Momentum flux, zonal velocity, mixed layer depth	74
A.1 Growth rates	94
A.2 Effective diffusivity	95

LIST OF TABLES

<u>Tables</u>		<u>Page</u>
1.1	Typical time constants of oceanic oscillations	10
2.1	Initial simulation parameters	25

1 INTRODUCTION

In my mind the most interesting direction in the ocean is the vertical. In particular the gradients of velocity, temperature, salinity, light are oriented nearly vertically Schmidtko et al. (2013). Taken to an extreme this suggest viewing a stratified ocean as layers (Pedlosky, 1998). All layers are not cerated equal, the topmost is privileged by emitting and absorbing radiation, and exchanging momentum, heat and fresh water with the atmosphere (Julian et al., 1970; Koshyk and Hamilton, 2001). This dissertation focuses on these strong gradients and how properties and organisms transit between layers, and the fluid motions that facilitate or impede that transport.

1.1 THE MIXED LAYER

The ocean mixed layer is the first stop for all of the surface fluxes. The thickness of the top layer varies globally and seasonally. There are various definitions for the ocean mixed layer using criterion based of density, temperature, and the their gradients which are all qualitatively similar statements of uniformity (Brainerd and Gregg, 1995; Birol et al., 2000). One convenient definition used by Schmidtko et al. (2013) incorporated data from the International Argo Program to create a global climatology of mixed layer depth (figure 1.1). The global picture of mixed layer depth shows variation from a few meters to hundreds of meters with a significant seasonal component. The large patterns of mixed layer depth are influenced both by local vertical transport of heat and salt as well as large scale motions where fluid is transported laterally, typically along isopycnals, reaching the mixed layer elsewhere. The interplay between the large scale motion and local vertical transports is the larger context in which many physical oceanographic questions reside. My interest is in the smaller scale motions and how they change the vertical, or diapycnal, transport.

1.2 FORCING

My preference for small scale phenomena is at odds with the length scales of oceanic forcing which skew toward large time and length scales. Atmospheric forcing is strongest at length scales $> 1/10^{\text{th}}$ the circumference of the earth (Julian et al., 1970; Koshyk and Hamilton, 2001) and periods from a day to a year (Vinnichenko, 1970). Strong rains in the the Inter-Tropical Convergence Zone

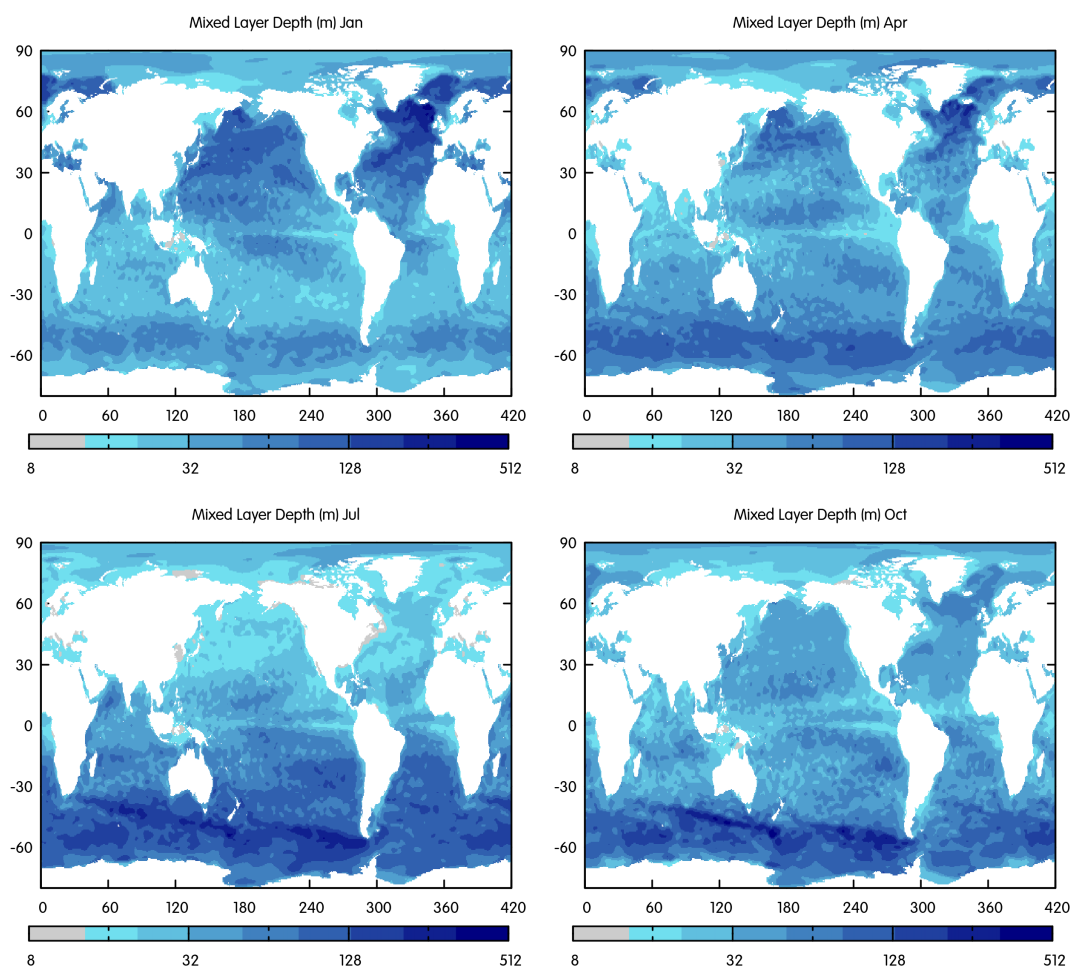


Figure 1.1: Mixed Layer Depth in January, April, July, and October (Schmidtke et al., 2013)

(ITCZ; You, 1995; Cronin and McPhaden, 2002), and the dry conditions at the Horse latitudes ($30^\circ - 38^\circ$ N/S) impose similar large length scales to the fresh water flux.

In addition to the atmosphere the ocean are also driven by the tides (Wunsch, 1998; Wunsch and Ferrari, 2004). The gravitational pull penetrates the full depth of the ocean affecting all the layers. By their astronomical nature tides have narrow spectral peaks at periods of a solar or lunar day (~ 24 hrs) and the associated harmonics with wavelengths the size of the ocean basins or large fractions thereof (Egbert et al., 1994).

The large scales of the principal atmospheric and astronomical forcing suggest the world ocean could be well described in terms of processes at the same time and length scales. This hope is further bolstered by the energy content of oceanic motions (Ferrari and Wunsch, 2008) and the near two dimensional nature of the ocean basins and that in two dimensional domains energy is preferentially transferred to larger scale (Fjørtoft, 1953; Batchelor, 1969; Pedlosky, 1987; Scott and Wang, 2005). In finite aspect ratio domains energy moves to both larger and smaller scales (Ferrari and Wunsch, 2008; Boffetta and Ecke, 2011) requiring understanding three dimensional dynamics. It is the transfer of energy to the smaller scales that will be the focus of the bulk of this dissertation.

Interaction with the ocean bottom is a good example of the three dimensional nature of ocean flows. Viscous drag removes momentum and has a small contribution to the oceanic heat budget. In particular regions of steep topography or geothermal vents cause the bottom's influence felt throughout the water column. Some of the energy deposited by the tides near high relief topography radiates as internal waves which dissipate in the interior of the ocean or break upon encountering more high relief topography. These flow interactions are localized, most of the world ocean floor is flat with little heat and momentum exchange. Furthermore the total heat flux at the bottom is negligible, compared with other sources of energy (Wunsch, 1998; Wunsch and Ferrari, 2004).

1.3 STRATIFICATION

The flow-topography interactions communicate with the interior through disturbances in the overlying stratification. Schmidt et al. (2013) provide a useful reanalysis of the Argo data set for exploration of distributions of heat and salt throughout the world ocean. From the profiles of

temperature and salinity a global distribution of buoyancy frequency

$$N^2 = -\frac{g}{\rho_0} \left. \frac{\partial \rho}{\partial z} \right|_P \quad (1.1)$$

quantifying the stability of the density ρ distribution (1.1) as a function of gravity g , and a representative density ρ_0 can be calculated. Much work has gone into quantifying the energy transfer from large scale motions into internal waves (e.g. Van Meurs, 1998; Alford, 2003). I will avoid the complication of topography in the particular questions I will explore but mention it here for completeness.

Away from boundaries shear is the only source of kinetic energy for smaller scale motions. Stratified shear instability has been examined in idealized form by many others (Miles, 1961; Howard, 1961; Hazel, 1972; Patnaik et al., 1976; Smyth and Peltier, 1993; Staquet, 1995; Jacobitz and Sarkar, 1999; Drazin, 2002) in closed domains (Özgökmen et al., 2009; Ilıcak, 2014), using unstable stratification (Asai, 1970; Clever and Busse, 1992; Cox, 1996; Domaradzki and Metcalfe, 1988), changing the initial perturbations (Jacobitz and Sarkar, 1998; Hwang et al., 2006; Brucker and Sarkar, 2007), and varying the background shear (Inoue and Smyth, 2009). Of particular interest to me is the view in terms of wave-wave interactions (Lvov and Yokoyama, 2009; Carpenter et al., 2013), and how that touches secondary instabilities (Smyth, 2003) and the transition to turbulence.

In reference to shear instability it is useful to examine where density is changing fastest (i.e. N^2 is at a maximum, figure 1.2). This pycnocline depth is shown in figure 1.3. Although the distribution of pycnocline depths (figure 1.3) is similar to the mixed layer depth of Schmidtko et al. (2013) (figure 1.1) it shows some small differences. The low values of the maximum N^2 (figure 1.2) highlights regions of deep convection in the Northern and Southern polar regions during their respective winters.

Sources of stratification leave an impression in the individual contributions of temperature (1.2)

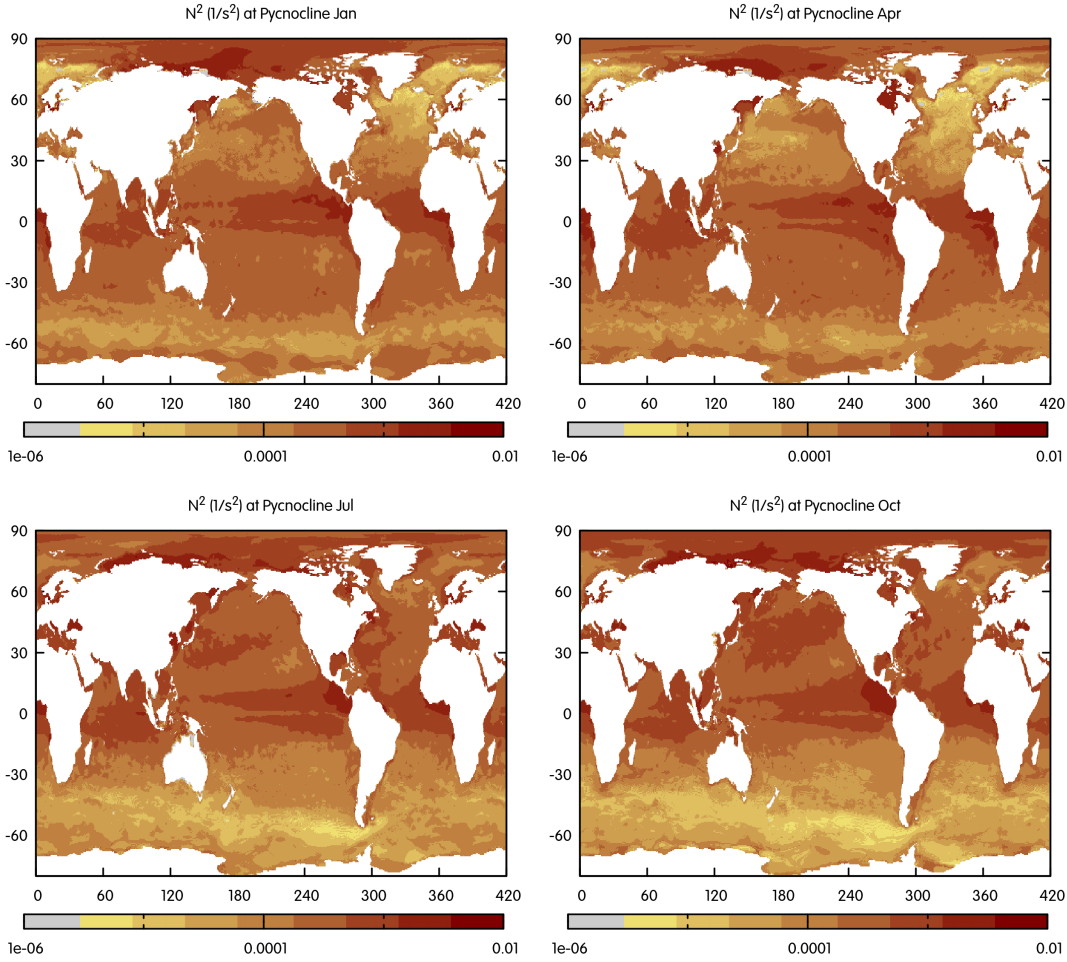


Figure 1.2: Maximum stratification in January, April, July, and October

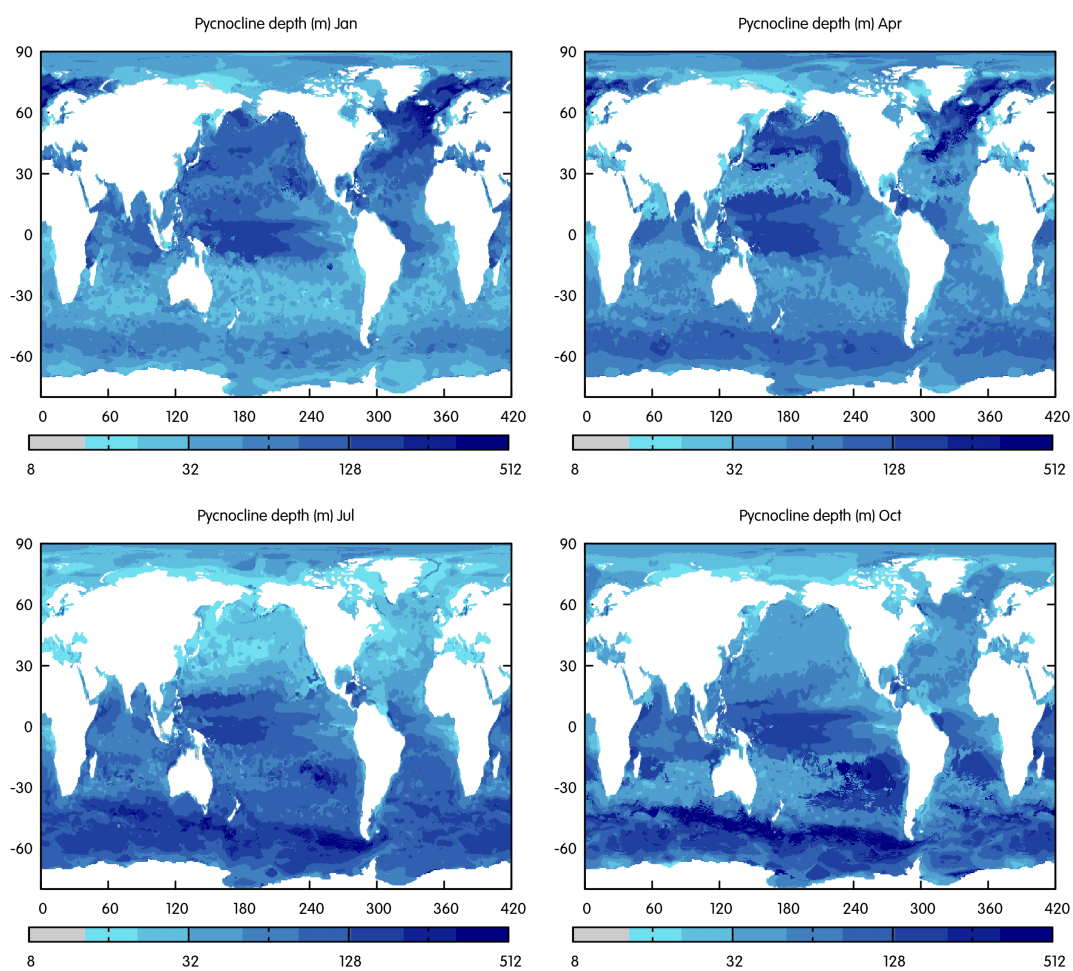


Figure 1.3: Depth of maximum stratification in January, April, July, and October

and salinity (1.3)

$$N_T^2 = +g\alpha \left. \frac{\partial T}{\partial z} \right|_P \quad (1.2)$$

$$N_S^2 = -g\beta \left. \frac{\partial S}{\partial z} \right|_P \quad (1.3)$$

to stratification, where α and β are the respective coefficients of expansion for temperature T and salinity S . The distribution of temperature stratification (figure 1.4) being strong year round in the tropics, and more seasonal toward the poles agrees with the solar forcing. The salt stratification distribution (figure 1.5) is less straight forward, the strongest features (in the Arctic Ocean) are beyond the scope of the discussion. Of particular importance here is the saline stratification in the eastern Indian Ocean which is relevant to the results in chapter 4 as the added stability from the halocline impacts vertical transports of heat.

1.4 TURBULENCE TRANSITION

To understand the transition from two dimensional flow to turbulent three dimensional flow it is useful to focus on the relevant instability mechanisms. The averaged influence of waves and wind create an additional instability in the motions of the mixed layer. The influence of convection and Langmuir circulations are tied to the surface. Interaction of the wave shear with fluctuations of cross wind velocity give rise to Langmuir circulations, helical flow structures parallel to the wind. The stratified water column below the mixed layer is well described by the interaction of shear and stratification. In the stratified region below the mixed layer the only source of instability is vertical shear. The strength and nature of the underlying stratification has a strong influence on which mechanism dominates the turbulent kinetic energy *tkc* budget. Close to the surface shear instability, convection, and Langmuir circulations all connect the surface fluxes with the stratified fluid at the base of the ocean mixed layer.

1.4.1 Turbulence and Motile Organisms

The transit of small organism through the water column is modulated by the turbulent mixing in and below the ocean mixed layer. How organisms interact with turbulence effects how their traversal of the water column affects their distribution. Small organisms which are able to orient

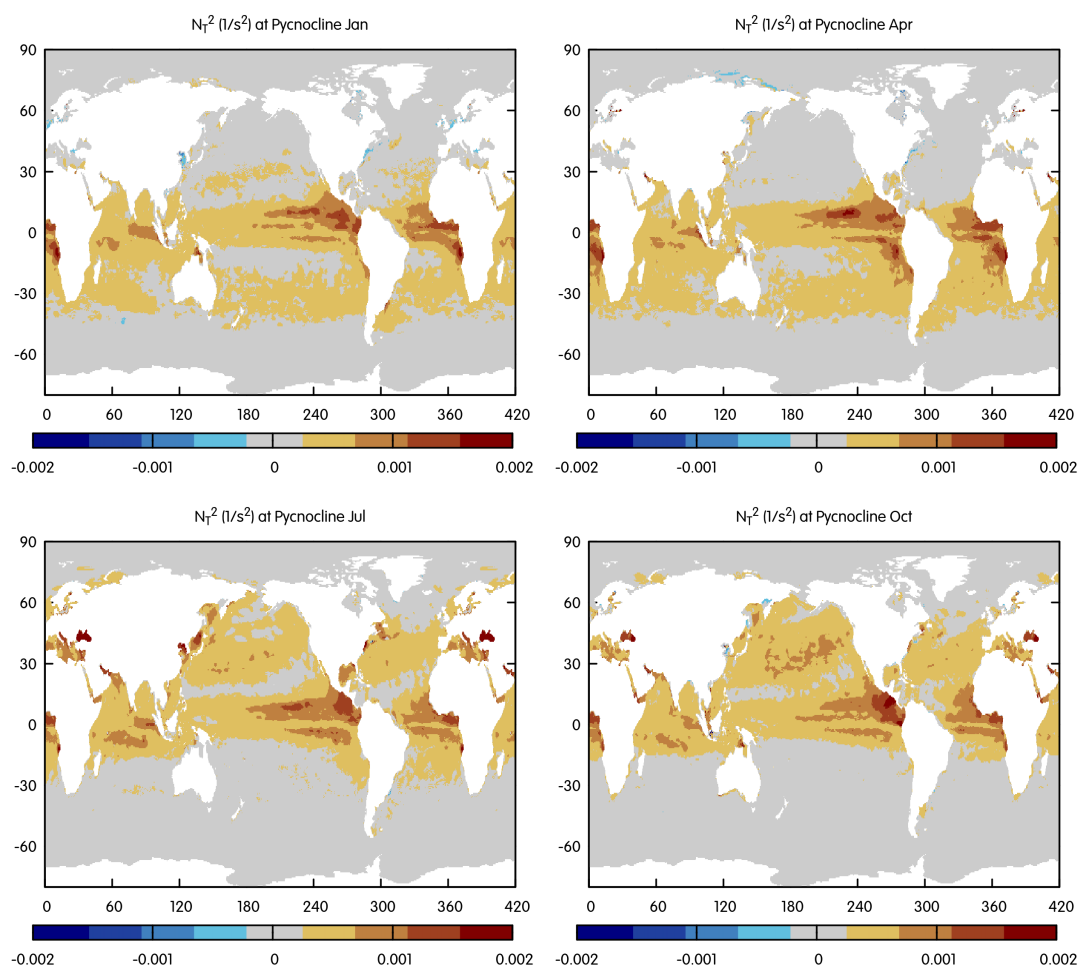


Figure 1.4: Maximum stratification in January, April, July, and October

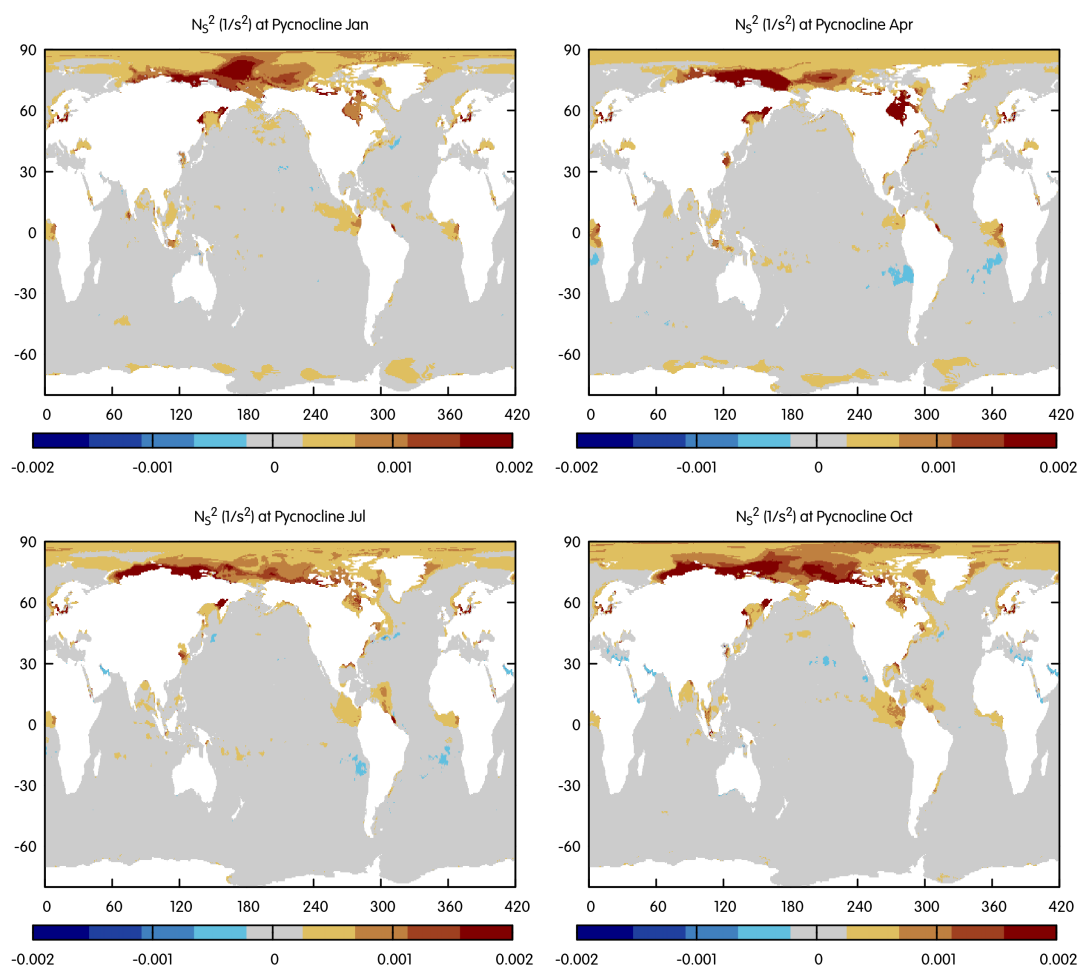


Figure 1.5: Maximum stratification in January, April, July, and October

Phenomena	Period	Wavelength
Sound waves	10^{-6} – 10^0 sec	10^{-3} – 10^3 m
Surface waves	10^0 – 10^1 sec	10^{-2} – 10^2 m
Internal waves	10^2 – 10^3 sec	10^{-3} – 10^3 m
Convection	10^2 – 10^3 sec	10^{-3} – 10^2 m
Viscous damping	10^1 – 10^{12} sec	10^{-3} – 10^3 m
Inertial motions	10^4 – 10 sec	10 – 10^7 m

Table 1.1: Typical time constants of oceanic oscillations

themselves in still water may have their swimming speed or ability to orient overwhelmed by turbulent motions. The loss of orientation creates a convergence in the net velocity of the organisms despite the underlying flow remains divergence-less.

The interaction of turbulence with vertically swimming organisms in the oceans constrain their abilities to take advantage of strong vertical gradients. By moving a few tens of meters vertically the environment changes drastically, the light dims, the composition of dissolved gases shifts, the current changes in magnitude and direction, temperature and salinity radically change (figures 1.4 and 1.5). This proximity of different habitats is taken advantage of by organisms too small to navigate the vast distances across ocean basins, the largest example of this is the diel vertical migration observed throughout the world ocean (Miller and Wheeler, 2012).

1.5 SCALE SEPARATION

The governing equations of fluid motions are an approximation given a set of axiomatic assumptions (Müller, 2006). This is true for layer models of the ocean, or the Boussinesq approximation. In the ocean mixed layer there are a broad array of relevant time and length scales, from breaking surface waves with periods of seconds to inertial with periods of order a day. Some mechanisms reach a quasi equilibrium during an organisms diel vertical migration, overnight convection, or the initial response of the surface to a storm front, long before mechanisms which rely on planetary rotation can influence dynamics. Separation allows the separate analyses of sound, surface waves, convection, Langmuir cells, shear instabilities, inertial waves, tides, etc when they are grouped into sets with shared length and time scales.

Taking advantage of this separation I choose to focus on turbulence mechanisms that are

independent of the influence of rotation. Similarly I seek to parameterize sound and surface wave influences in favor of internal gravity waves which dominate the stratification below the mixed layer. The rapid motions of the surface are well described by wave averaged quantities such as the Stokes drift. Sound waves are parameterized by the imposition of incompressibility $\nabla_i u_i = 0$. Disregard of tides and planetary rotation limits predictions periods of order a day. Use of wave averaged quantities for sound and surface waves disallow any dynamics at timescales shorter than that of a few seconds (table 1.1). Wave averaging distills relevant wave dynamics, and is used in the deep ocean Leibovich (1983) as well as in the near-shore Battjes (1988).

Eliminating the fastest and slowest time scales from consideration is not sufficient to model the range of fluid motions accurately at even this intermediate scale. Acoustic waves are much faster than oceanic currents (Mach number $\ll 1$) and the interaction between sound waves and fluid motion is well described by incompressibility. Surface waves are also typically faster than ocean currents (Froude number $\lesssim 1$) but unlike sound the scale separation is not as extreme. Any averaging which removes surface waves will average fluid motions at the same time and length scales. I use two techniques to accommodate the incomplete separation of surface waves and internal motions of the fluid. Large Eddy Simulation (LES) explicitly averages over the smallest scales of turbulence allowing for wave averaged quantities, like Stokes drift, to be introduced consistently into the equations of motion therefore mixed layer dynamics are modeled using LES (Skylingstad et al., 1999). Wind and waves stir the ocean near the surface but their influence rapidly decreases away from the surface and at sufficient depth their influence may also be safely ignored. By restricting the region of interest below wave motion the smaller scales typical of turbulent dissipation can be directly modeled.

For simulations away from the wave driven surface two and three dimensional Direct Numerical Simulations of stratified fluid (Winters et al., 2004) are used driven by vertical gradients in buoyancy, and vertical momentum fluxes. Embedded in the DNS is an individual based (Lagrangian) models of gyrotactic behavior (Hopkins and Fauci, 2002; Durham et al., 2009) which is immune to numerical diffusion and includes non-single valued fields (i.e. swimming orientation) without any additional approximation. The Lagrangian models inefficiently reproduces concentration distributions and a parallel continuous (Eulerian) concentration model is also used to better describe

concentration gradients.

This dissertation covers sheared stratified turbulence and how it modifies vertical fluxes of biophysical quantities. Small gyrotactic organisms transiting a growing shear instability is modeled in chapter 2. Chapter 3 proposes a limiting condition on the formation of density overturns by the shear instability modeled as part of chapter 2 instabilities. Ocean dynamics involve shear instability as well as buoyant and surface wave effects are modeled in chapter 4 where the turbulent kinetic energy budget in a LES is driven using observations of a westerly wind burst in the Indian Ocean. Some general conclusions about vertical fluxes and turbulence are presented in chapter 5

2 TRAPPING OF GYROTACTIC ORGANISMS IN AN UNSTABLE SHEAR LAYER

Martín S. Hoecker-Martínez,

William D. Smyth

Continental Shelf Research

Journals Customer Service

3251 Riverport Lane

Maryland Heights, MO 63043, USA

#36

To explore new mechanisms for planktonic thin layer formation, particle and continuum models of gyrotactically swimming phytoplankton are embedded in simulations of a dynamically unstable stratified shear layer. Two trapping mechanisms are observed in the developing Kelvin-Helmholtz (K-H) billow train. Within the K-H billows, a particle can remain preferentially in downwelling regions, canceling its upward swimming motion. In the braids that separate the billows, intense shear defeats the gyrotactic stabilization mechanism and causes cells to tumble. Particle and continuum models are compared statistically to reveal both consistencies and weaknesses in each. A scaling based on Reynolds number and swimming speed is used to predict the maximum concentration generated by an instability event. Although K-H billows are short lived in comparison with planktonic thin layers observed in the coastal oceans, the resulting trapping causes rapid aggregation. We conclude that trapping in a growing K-H instability could contribute to the development of the observed cell concentrations.

2.1 INTRODUCTION

Shear flows can disorient motile phytoplankton, in some conditions causing them to aggregate (Durham et al., 2009). Dense biological layers of thickness ~ 1 m have been observed in fjords (Deksheniaks et al., 2001) as in more open coastal areas (Cheriton et al., 2007; Churnside and Donaghay, 2009; Benoit-Bird et al., 2009; Steinbuck et al., 2009; Sullivan et al., 2010a). Spatial and temporal distribution patterns of phytoplankton determine which grazing behaviors will be successful at higher trophic levels. They also affect the planning and interpretation of biological sampling efforts, which include implicit assumptions about the distribution. Distributions are controlled by the surrounding flow and by swimming behavior: speed and orientation. One mechanism of orientation is gyrotaxis, wherein a gravitational torque acts as a restoring force and flow vorticity acts to twist the organisms away from a vertical orientation (Kessler, 1986; Durham et al., 2009, 2011). Development of stratified shear flow is often understood through the evolution of unstable Kelvin-Helmholtz (K-H) modes (Miles, 1961; Hazel, 1972; Corcos and Sherman, 1984; Klaassen and Peltier, 1985, 1991; Caulfield and Peltier, 1994, 2000; Smyth and Moum, 2001; Smyth et al., 2011). In this study we focus on the interaction of a motile gyrotactically orienting organism with a growing Kelvin-Helmholtz billow train.

The ability of micro-organisms to propel themselves through the fluid can create complex patterns and interactions between the underlying flow field and the concentration. For phytoplankton, the magnitude of the swimming velocity V_s is much smaller than the flow velocity, so that the relative motility $V_b = V_s/U$ is much less than one, where U is a characteristic fluid velocity. The low relative motility does not preclude vertical migration in the water column, as oceanic flows are dominated by horizontal motions. Nonzero V_s distinguishes the types of aggregation possible (Childress et al., 1975; Kessler, 1986; Pedley et al., 1988; Torney and Neufeld, 2007) from the analogous trapping of sinking inert particles (Stommel, 1949; Fung, 2000). For a uniform concentration and orientation in non-divergent flow, there can be no accumulation or rarefaction. Only if orientation is allowed to vary can aggregations emerge from a uniform background.

The aggregation of small organisms into coherent structures has been observed at many scales. In the coastal ocean large layer structures have been observed. There is not yet a consensus definition of biological thin layers, though there are commonalities among the differing definitions. In an overview of the Layer Organization in the Coastal Ocean (L.O.C.O.) project Sullivan et al. (2010b) summarize the diverse definitions into three qualitative rules:

“(1) The layer structure must persist over time and space; (2) the layer vertical thickness must be below some maximum, and there must be an objective, clearly defined method for calculating the vertical thickness; and (3) the layer maxima must meet a minimum signal strength (e.g., 2 or 3 times greater than background values).”

Here, we investigate the possibility that Kelvin-Helmholtz instability could lead to a layer which satisfies these criteria.

Under controlled conditions at laboratory scales the aggregation mechanisms of particular species have been studied (e.g., Kessler, 1986; Durham et al., 2009). Initial studies focused on cases with no background flow (Kessler, 1986; Childress et al., 1975; Pedley et al., 1988). More recently, Durham et al. (2009) showed how an imposed shear can cause the aggregation of the model gyrotactic organism *C. nivalis* into laminar structures in a tank. These experiments suggest a possible mechanism for the formation of concentrated layers of motile species as they traverse a flow field.

The flow geometry we examine is that of a shear layer including the influence of stratification.

This system is an idealized representation of the shear at the base of the surface mixed layer (e.g., Woods, 1968; Spigel et al., 1986; Dale et al., 2008). In strong shear there is a dynamic Kelvin-Helmholtz instability, which causes the shear layer to coalesce into a series of Kelvin-Helmholtz billows connected by thin regions of intense shear. Fine scale observations of displacements consistent with Kelvin-Helmholtz billows have been observed in the seasonal thermocline (Woods, 1968) tidal flows (Geyer and Smith, 1987; Seim and Gregg, 1994), internal solitary waves (Moum et al., 2003), and in the deep ocean (van Haren and Gostiaux, 2010). Little is known of the horizontal scales of these events. Moum et al. (2011) observed K-H billow trains with ~ 10 billows in the along stream direction and Thorpe (2002) has observed a knotting in the cross stream direction which occurs at ~ 4 times the down stream spacing before more complex flow patterns emerge. Additional regions where the Richardson number is at or below $1/4$, and where K-H billows can therefore grow (Miles, 1961; Howard, 1961), have been observed associated with biological layers (Deksheniaks et al., 2001) and elsewhere in the coastal ocean (e.g Suanda, 2009). Turbulence statistics in mixing patches observed in the thermocline compare favorably with those drawn from direct numerical simulations (DNS) of Kelvin-Helmholtz billows (Smyth et al., 2001).

The coupling of shear flows and plankton population dynamics to form laminar structures have most often been modeled assuming only advective and diffusive forcings (Franks, 1995; Stacey et al., 2007; Birch et al., 2008). These mechanisms rely on shear to steer a plankton aggregation into a planar shape. Durham et al. (2009) model gyrotactic stability as a critical point in a continuum model where the transition to gyrotactic instability is discontinuous and the orientation is replaced with a null vector if the ratio of viscous to gravitational torques exceeded the stability criterion in the steady shear flow. Others (Pedley and Kessler, 1990; Lewis, 2003; Thorn and Bearon, 2010) use a probability distribution of orientation. Hopkins and Fauci (2002) use the full torque balance including inertial terms and solve the second order differential equation for orientation in their particle model. The torque balance without the inertial term is used by the particle model of Durham et al. (2009).

In the present study we use a two dimensional direct numerical simulation of stratified flow to examine the distribution of simple gyrotactic organisms in the presence of an unstable shear layer. The two-dimensional model is restricted to the early stages of the K-H instability, shortly

after the appearance of overturns a Rayleigh-Bernard convective instability in the billows causes the flow to become fully three-dimensional (Klaassen and Peltier, 1985, 1991; Smyth and Moum, 2001). Organisms are modeled both as individual particles and as a continuous concentration field to study the trapping and aggregation of gyrotactic organisms in the developing shear instability.

The detailed description of the relevant dynamics for small gyrotactic particles in stratified shear flow are elaborated in section 2.2 and we describe the numerical methods to simulate these phenomenon. Results are given in section 2.3 and our interpretation is given in section 2.4. Appendices give further information on numerical methods and physical assumptions made in the design of the models.

2.2 METHODS

Here we describe our model for the flow physics as well as individual and continuum models for the biology.

2.2.1 Flow model

The fluid is modeled using the Boussinesq approximation. For notational simplicity buoyancy $b = -(g/\rho_0)(\rho - \rho_0)$ and reduced pressure $p = P/\rho_0$ are used instead of density ρ and pressure P . The constants ρ_0 and g represent mean density and gravitational acceleration respectively. This reduces the Boussinesq equations to

$$\frac{\partial u_i}{\partial t} = -u_j \nabla_j u_i - \nabla_i p + b \delta_{3i} + \nu \nabla^2 u_i \quad (2.1)$$

$$\frac{\partial b}{\partial t} = -u_j \nabla_j b + \kappa \nabla^2 b \quad (2.2)$$

$$\nabla^2 p = -(\nabla_i u_j)(\nabla_j u_i) + \frac{\partial b}{\partial x_3} \quad (2.3)$$

where (2.3) follows from (2.1) and the continuity condition $\nabla_j u_j = 0$. The simulation domain is horizontally periodic and free slip in the vertical. Details of the numerical methods and code validation are given in A.1.

The initial state of the fluid is a two layer shear flow with no vertical velocity. At the boundary there is no horizontal stress, no vertical flow, and the buoyancy is held fixed. The initial profiles

of velocity and density are given by

$$u = \Delta U \tanh z/h \quad (2.4)$$

$$b = \Delta b \tanh z/h + b_{\text{noise}} \quad (2.5)$$

where h represents the half-thickness of the shear layer and ΔU and Δb are half of the velocity and buoyancy difference across the layer (Hazel, 1972; Klaassen and Peltier, 1991; Smyth and Peltier, 1993). This choice of scaling gives a simple form for the initial Reynolds number $\text{Re} = \Delta U h / \nu$ and Richardson number $\text{Ri} = \Delta b h / \Delta U^2$ which govern the stability of the flow (Miles, 1961; Howard, 1961; Tennekes and Lumley, 1972).

The initial density profile (2.5) includes a random noise field whose amplitude is chosen so that no overturns (Thorpe, 1977) are created by the perturbation. This is accomplished by defining

$$b_{\text{noise}} = r \times \Delta z \frac{\partial b}{\partial z}, \quad (2.6)$$

which is the product of a uniform random variable $r \in (-0.5, 0.5)$ and a first order estimate of the difference in buoyancy b between adjacent levels. The uniform random variable r ensures that potential energy is placed into all available horizontal wave numbers equally.

2.2.2 Biological modeling

The organisms in this study are assumed to be neutrally buoyant and smaller than the Kolmogorov scale. This allows for a simplification of the governing equations. Particles smaller than flow features act as though they have no inertia and follow the flow trajectories (Crowe et al., 1996). Similarly the moment of inertia may be neglected for particles much smaller than the smallest vortices in the fluid, and we may assume the vorticity is uniform in the vicinity of the particle. This line of reasoning follows Kessler (1986) where the two principal torques are (1) the viscous torque $\vec{\tau}_\nu$ of the fluid motion, opposing the relative rotation of the particle, and (2) the gravitational torque $\vec{\tau}_g$ which acts to restore the orientation of the particle (Figure 2.1). The action of $\vec{\tau}_g$ is called gyrotactic reorientation. The equation of motion for the angular motion of

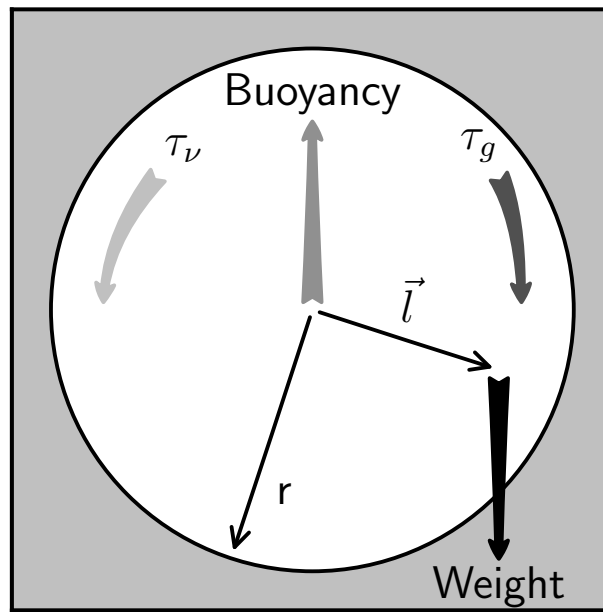


Figure 2.1: Forces acting on a gyrotactic organism

the particle has the form

$$\mathbf{I}\vec{\alpha} = \underbrace{4\pi\rho\nu r^3}_{\vec{\tau}_\nu} \left(\vec{S} - 2\vec{\Omega} \right) + \overbrace{\frac{4\pi}{3}r^3\rho}_{\vec{\tau}_g} \left(\vec{l} \times \vec{g} \right) \quad (2.7)$$

where $\vec{\alpha}$ is the angular acceleration, $\vec{S} = \vec{\nabla} \times \vec{u}$ is the vorticity, and $\vec{\Omega}$ is the angular velocity of the particle, (Kessler, 1986; Hopkins and Fauci, 2002). If we assume a small particle we may ignore the inertial term, and find an equation for the angular velocity directly (Kessler, 1986; Pedley and Kessler, 1987, 1990, 1992; Jones et al., 1994; Lewis, 2003; Durham et al., 2009)

$$\vec{\Omega} = \frac{1}{2}\vec{S} - \frac{1}{2B}\hat{l} \times \hat{k} \quad (2.8)$$

where $B = 3\nu/lg$ is identified as the gyrotactic reorientation time. In A.3 we constrain the size range in which (2.8) may be used instead of (2.7). The balance of gravitational and viscous torques can be used to define another non-dimensional number the gyrotactic stability $BS = B\|\vec{S}\|$. A body is gyrotactically unstable when the product $BS > 1$.

To model particle orientation, we use (2.8). A full discussion of the validity of this simpler model for oceanic parameter ranges over the higher order models is given in A.3. We further simplify our equations by treating gyrotactic organisms as spherical objects whose moment of inertia may be ignored following Kessler (1986). The details of the spherical assumption and its validity in unstable sheared flow is shown in A.2. Modeling the dynamics of small organisms can be done as an ensemble of individuals or in terms of concentrations. As the number of individuals in a model increases, the collective statistics will converge to the concentration model if the two models are consistent. Individual models can yield information about trajectories and trapping mechanisms while the concentration model is more suited to showing distribution patterns. Because of these disparate strengths and weaknesses both types of models are developed for gyrotactic organisms in a shear flow.

2.2.2.1 Particle Model

The particle tracking model uses bilinear interpolation (Press et al., 1992) of the velocity \vec{u} and vorticity \vec{S} to propagate the position \vec{x} and orientation \vec{p} of each organism. The position is advected by fluid flow and by the organism's motility, while the orientation is dictated by the balance of viscous and gravitational torques in (2.8). These give rise to

$$\frac{d\vec{x}}{dt} = \vec{u} + V_s \vec{p} \quad (2.9)$$

$$\frac{d\vec{p}}{dt} = \left(\frac{1}{2} \vec{S} - \frac{gl}{6\nu} \vec{p} \times \hat{x}_3 \right) \times \vec{p} \quad (2.10)$$

where the term in parentheses is the rate of rotation of the particle (Durham et al., 2009). Since \vec{p} represents an orientation and (2.10) preserves magnitude, $\|\vec{p}\| \equiv 1$.

2.2.2.2 Continuum model

The concentration of the organisms is governed by advection by the fluid, their own motility and diffusion. This is expressed through a flux conservation equation

$$\frac{\partial c}{\partial t} + \nabla_i (u_i c + V_s p_i c) = \nabla_i (D \nabla_i c). \quad (2.11)$$

The left hand side of (2.11) is the sum of local aggregation, fluid advection, and biological advection rates. This sum is equal to the divergence of a diffusive flux on the right hand side of (2.11). The particle model has no analog for this diffusive flux; it is added to maintain numerical stability in regions of steep concentration gradients.

To distinguish between the effects of a mean shear on the motile species and the dynamically unstable flow condition modeled later it is useful to begin by considering static shear flow (2.4) with gyrotactically stable orientation ($BS < 1$) and no diffusion, viscosity or stream-wise variability. This reduces (2.11) to a one dimensional conservation equation

$$\frac{\partial c}{\partial t} = -V_s \frac{\partial}{\partial z} p_z c. \quad (2.12)$$

If we further assume the organisms cross the shear layer slowly compared to the shear timescale,

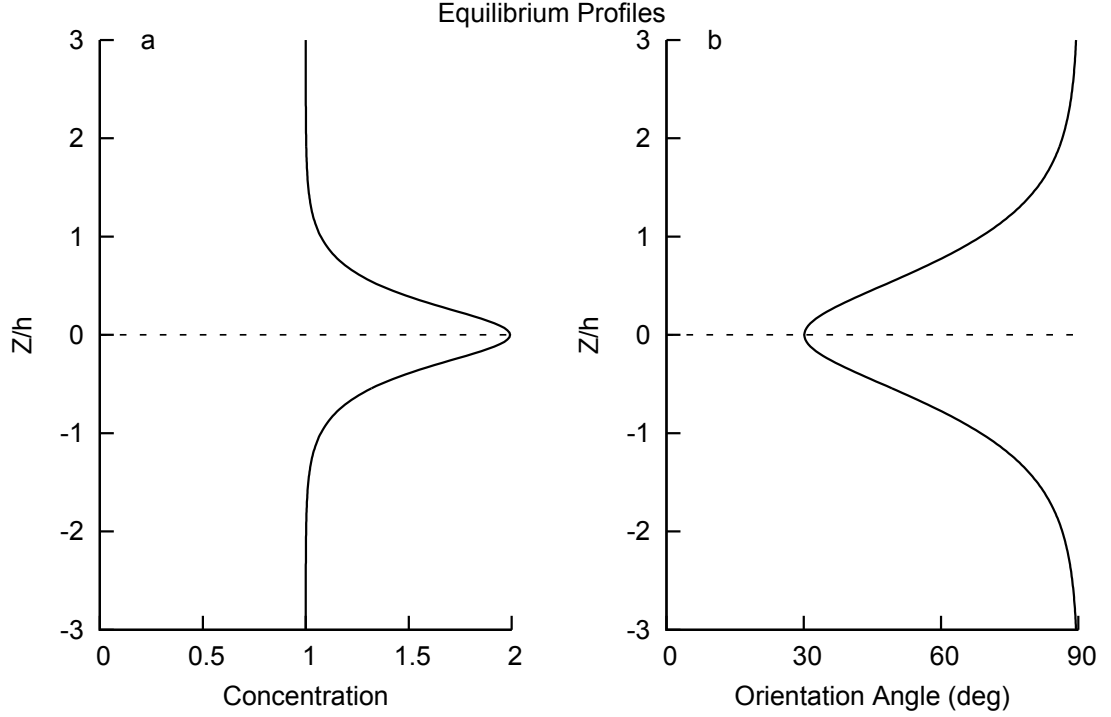


Figure 2.2: Steady state profiles of normalized concentration, and orientation. The gyrotactic stability parameter is $BS_{\max} = 0.865$ and the background concentration is $c_0 = 1$

equivalently $V_b \ll 1$, then \vec{p} may be assumed to be the equilibrium value of (2.10)

$$\vec{p} = \hat{x} BS_{\max} \operatorname{sech}^2 \frac{z}{h} + \hat{z} BS_{\max} \sqrt{(BS_{\max})^{-2} - \left(\operatorname{sech}^2 \frac{z}{h}\right)^2} \quad (2.13)$$

where B is the reorientation time and $S_{\max} = U/h$ is the maximum shear. Seeking a steady state solution of (2.12) assuming a background concentration c_0 yields

$$c = \frac{c_0}{\sqrt{1 - (BS_{\max} \operatorname{sech}^2 \frac{z}{h})^2}}. \quad (2.14)$$

The vertical profiles of concentration and swimming orientation are illustrated in Figure 2.2.

The solution (2.13) and (2.14) relies on steady flow and gyrotactic stability $BS_{\max} < 1$. Though

these assumptions are not valid for the time varying flow considered later, the solution is informative. It shows the nature of the transition from stable to unstable orientation and highlights BS_{\max} as a critical non-dimensional quantity. Diffusive and advective effects will shift the orientation away from the equilibrium value with the local vorticity. The transition will likely occur at $BS_{\max} > 1$ when these effects are included but this simple model suggests a smooth increase in the peak concentration with increasing shear in the stable regime.

We now relax the assumptions of steady flow and gyrotactic stability. To allow tumbling organisms and dynamic flow we model the mean swimming orientation over a grid box p_i and assume the swimming speed may be taken to be constant V_s and the concentration flux $V_s c p_i$ obeys the continuous analog of (2.10)

$$\begin{aligned} \frac{\partial}{\partial t}(V_s c p_i) + \nabla_j (u_j V_s p_i c + V_s^2 p_j p_i c) \\ = V_s c \epsilon_{ijk} \Omega_j p_k + D \nabla^2 (V_s p_i c) \end{aligned} \quad (2.15)$$

where Ω_j is the rate of rotation given by (2.8) and the diffusivity D is assumed constant. By tracking both concentration and orientation we can follow the system through the transition to gyrotactic instability where $BS > 1$. Equations (2.11), and (2.15) can be solved for the Eulerian time evolution for the concentration and orientation fields

$$\begin{aligned} \frac{\partial c}{\partial t} = & - (u_j + V_s p_j) \nabla_j c \\ & - V_s c \nabla_j p_j + D \nabla^2 c \end{aligned} \quad (2.16)$$

$$\begin{aligned} \frac{\partial p_i}{\partial t} = & \epsilon_{ijk} \Omega_j p_k - (u_j + V_s p_j) \nabla_j p_i \\ & + D \nabla^2 p_i + \frac{2D}{c} (\nabla_j c) (\nabla_j p_i). \end{aligned} \quad (2.17)$$

Together (2.16) and (2.17) form a continuum model of gyrotactic organisms. These equations are highly non-linear, in particular the final term in (2.17) is proportional to $1/c$. We are seeking to model large variations in the concentration and cannot a priori dismiss these interactions. Despite the complex nature of the diffusive terms there is a Laplacian term for both the concentration and orientation that suggests the use of Fourier decomposition for an exact solution similar to

equations (A.6) and (A.7). If p_i is to serve as a unit vector representing orientation we must preserve its unit length. Equation (2.17) does not conserve magnitude exactly. The unitary nature of the orientation is preserved in a separate normalizing step

$$p_i = \frac{p_i^*}{\sqrt{p_j^* p_j^*}} \quad (2.18)$$

where p_i^* is the result of stepping (2.17) forward in time.

The boundary conditions of the flow suggest boundary conditions for the concentration and orientation. Far from the shear layer the orientation is vertical $p_i = \delta_{i3}$ and the concentration is a background value c_0 . The background value is arbitrary and we may normalize by c_0 . These far field conditions argue for constant boundary conditions in the vertical and corresponds to an expansion into a sine series in the vertical with the boundary values of c and p_i subtracted. The variables which enter into the Fourier transform are a reduced concentration $c' = (c/c_0) - 1$ and orientation $p'_i = p_i - \delta_{i3}$.

$$\begin{aligned} & e^{-Dk^2 t} \frac{\partial}{\partial t} \left(e^{Dk^2 t} \mathcal{F}(c') \right) \\ = & -\mathcal{F} \left((u_j + V_s (p'_j + \delta_{j3})) \nabla_j c' \right) \\ & -\mathcal{F} \left(V_s (1 + c') \nabla_j p'_j \right) \end{aligned} \quad (2.19)$$

$$\begin{aligned} & e^{-Dk^2 t} \frac{\partial}{\partial t} \left(e^{Dk^2 t} \mathcal{F}(p'_i) \right) \\ = & -\mathcal{F} \left((u_j + V_s (p'_j + \delta_{j3})) \nabla_j p'_i \right) \\ & +\mathcal{F} \left(2D \frac{(\nabla_j c') (\nabla_j p'_i)}{c'+1} \right) \\ & +\mathcal{F} \left(\epsilon_{ijk} \Omega_j (p'_k + \delta_{k3}) \right) \end{aligned} \quad (2.20)$$

We assume at vertical boundaries the organisms maintain their initial concentration and orientation. A uniform initial state is used for concentration and orientation with the assumption that a near steady state will develop in the biology before the flow instability has grown significantly.

	Ri_0	Re_0	$V_s/\Delta U_0$	L_x/h_0	L_z/h_0	$N_x \times N_z$
a	0.10	500	0.015	27.9	20.925	1024×768
b	0.13	500	0.015	27.9	20.925	1024×768
c	0.13	750	0.015	27.9	20.925	1536×1152
d	0.15	750	0.015	13.95	20.925	768×1152
e	0.15	750	0.010	13.95	13.95	512×512
f	0.17	1500	0.006	13.95	13.95	1024×1024
g	0.17	1500	0.006	13.95	13.95	1152×1152
h	0.17	1250	0.006	13.95	13.95	960×960
i	0.15	1250	0.015	13.95	13.95	1280×1280
j	0.17	1250	0.015	13.95	13.95	1280×1280
k	0.17	1500	0.015	13.95	13.95	1536×1536

Table 2.1: Initial simulation parameters. Richardson number Ri_0 , Reynolds number Re_0 , relative motility $V_s/\Delta U_0$, domain width relative to layer thickness L_x/h_0 , domain height relative to layer thickness L_z/h_0 , horizontal resolution N_x , and vertical resolution N_z .

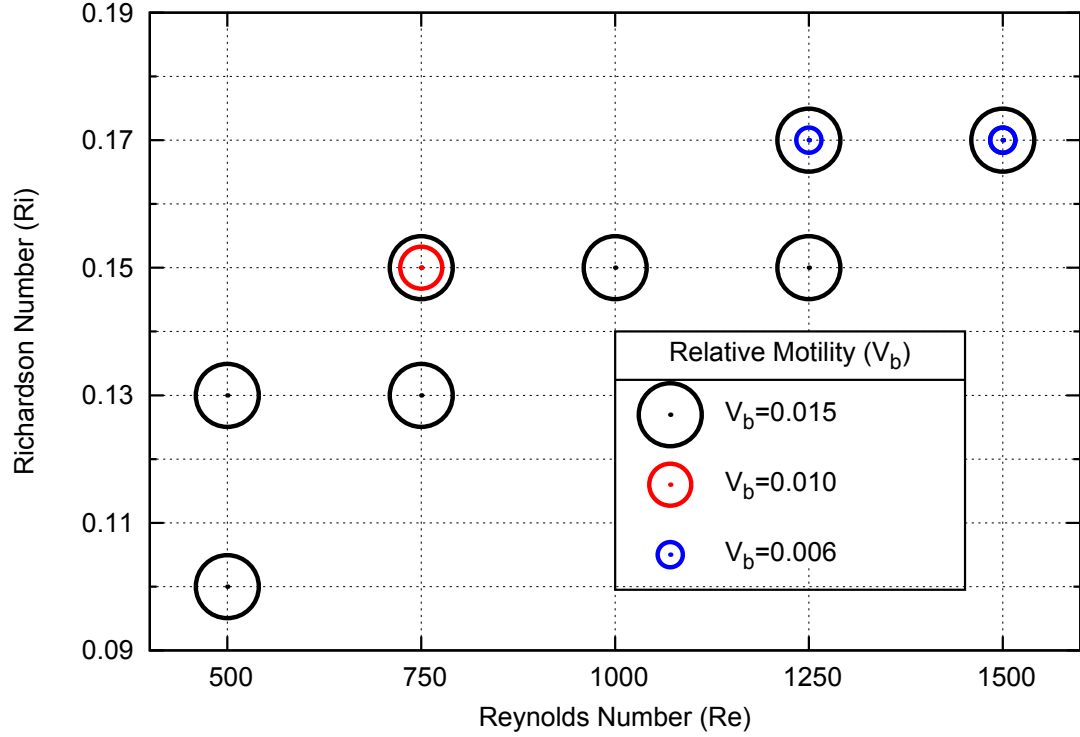


Figure 2.3: Initial simulation parameters

2.2.3 Simulation parameters

Simulations were made at various points in the multi-dimensional phase space (Table 2.1, Figure 2.3). The Reynolds number was chosen for computational tractability. A Prandtl number of 1 was used instead of the oceanic value ~ 7 for all runs to allow for faster computation. For the K-H instability to create overturns the Richardson number must be below $1/4$. Low Reynolds numbers further depress the threshold as the increased viscosity damps the growing instability. To mimic oceanic flows, Richardson numbers are chosen to be as close to the stability limit $1/4$ as numerically feasible.

The diffusivity for the biological quantities was taken to be the same as the thermal diffusivity of each run. To keep the dimensionality of parameter space manageable gyrotactic reorientation time is chosen to be $B = h_0/\Delta U_0$ so that $BS \leq 1$ everywhere in the initial flow. The parameters of each run are summarized in Table 2.1 and Figure 2.3. For the organisms to be considered plankton $V_b \ll 1$. The range of relative motility is further constrained from above by resolution requirements $V_b < h_0/\text{Re}\Delta x$ and from below by the requirement that the biology reach a steady state before billow formation $V_b > 1/200$. The domain size is chosen to match the wavelength of fastest growing mode in a Kelvin-Helmholtz instability found by Hazel (1972) $L_x/h \approx 13.95$ with the weak Richardson number dependence ignored following Smyth (2003). Simulations are halted after overturns occur as the flow can no longer be modeled two dimensional flow.

2.3 RESULTS

Our main focus will be on case k (Table 2.1) for both biological models as it is closest to an oceanic parameter regime. Concentration and individual organism tracks are used to show the interaction of the flow and the gyrotactic organisms.

2.3.1 Particle tracking results

The evolved state of an initially uniform random seeding of particles in the domain reflects the shape of the shear instability (Figure 2.4). The enhanced shear in the braids can exceed the limit of gyrotactic stability, causing organisms to tumble. This is most clearly evident in the dotted curve in Figure 2.5, which shows the evolution of a sample particle's orientation. After $t\Delta U/h \sim 220$, the

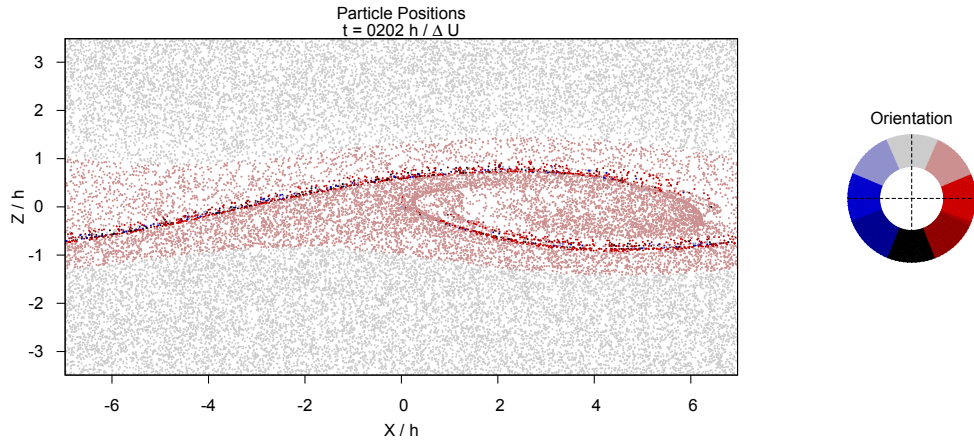
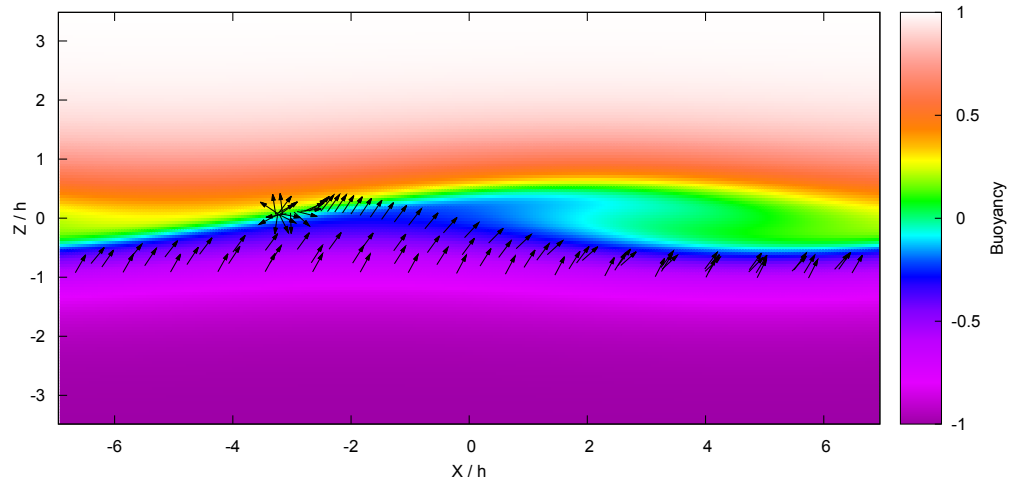


Figure 2.4: Particle positions and orientations at the time of fastest aggregation from run k. The region shown includes only the central half of the vertical domain.

particle rotates rapidly. The inverted organisms appear first in the braid region. The individual particle track in Figure 2.5 and the inverted organisms (dark red and blue) in Figure 2.4 illustrate the necessary conditions for entrapment as the organism travels through the growing instability. In Kelvin-Helmholtz billow trains, high vorticity fluid is moved from the braids to the billows. A particle which enters the braid region begins to rotate, and thereafter more closely follows the trajectory of a fluid parcel. The particle in Figure 2.5 is essentially a tracer after scaled time 220, when it travels along the braid instead of across it (solid curve in Figure 2.5b). By this mechanism, organisms are steered away from the braids and into the rotating billows.

Within the billow, vorticity is lower than in the braids and the particle may maintain a stable orientation as exemplified by the gray dotted curve in Figure 2.6b. A stable orientation in the billow may not be sufficient for the particle to cross the shear layer, however. The vertical velocities in the circulating billow can exceed the swimming velocity V_s , in which case the trapping mechanism of Stommel (1949) can come into play (Figure 2.6). The cell follows a quasi-elliptical trajectory that is offset horizontally from the center of the billow, such that it spends an increased fraction of its cycle in regions of downward flow. This asymmetry cancels the upward swimming motion, with the result that the cell remains trapped in the billow.

(a)



(b)

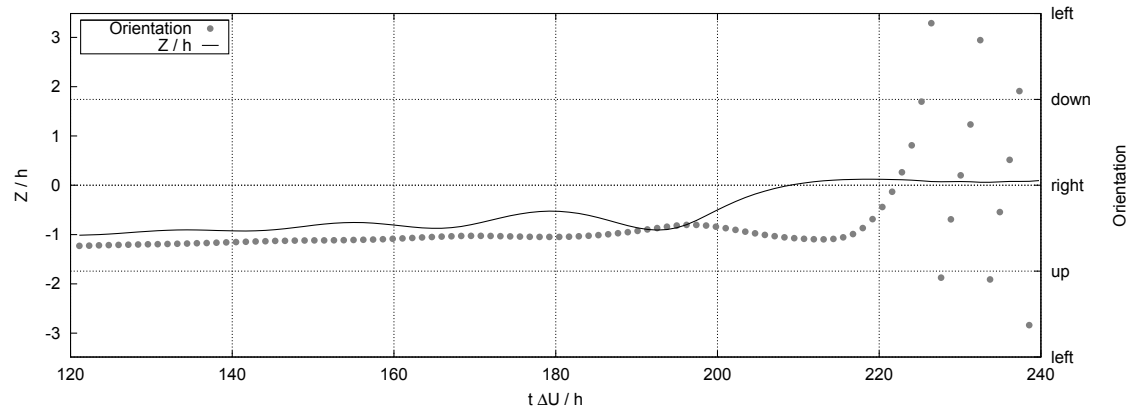
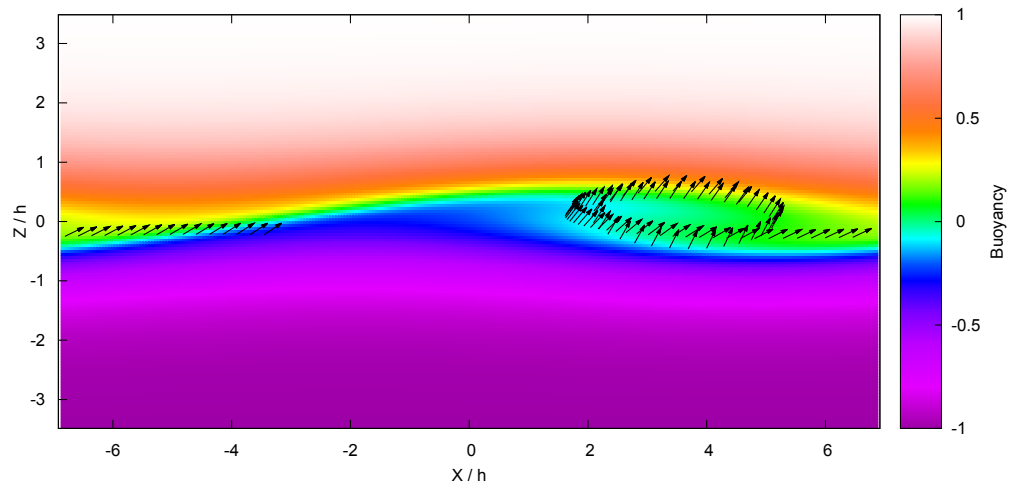


Figure 2.5: (a) Trajectory of a gyrotactically trapped organism in run k superimposed on the buoyancy field from $t = 180h/\Delta U$. (b) Vertical position Z/h (solid) and orientation (dotted) versus time for the same trajectory. The region shown includes only the central half of the vertical domain.

(a)



(b)

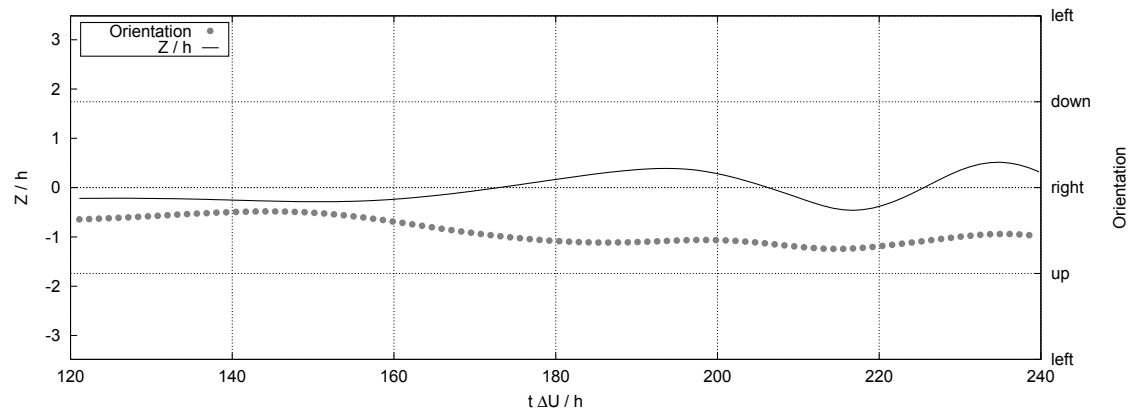


Figure 2.6: (a) Trajectory of a vortex trapped organism in run k superimposed on the buoyancy field from $t = 180h/\Delta U$. (b) Vertical position Z/h (solid) and orientation (dotted) versus time for the same trajectory. The region shown includes only the central half of the vertical domain.

2.3.2 Continuum model results

As the instability grows, local concentration maxima are generated around the edge of the recirculating billow region and the strained braid region. The concentration field has much smaller scales than the underlying fluid flow since the biological advection admits divergent motion, unlike the physical flow field. Figure 2.7a shows a snapshot of the concentration after the instability has caused unstable stratification in the billows. At this time the maximum value of concentration is $2.7c_0$.

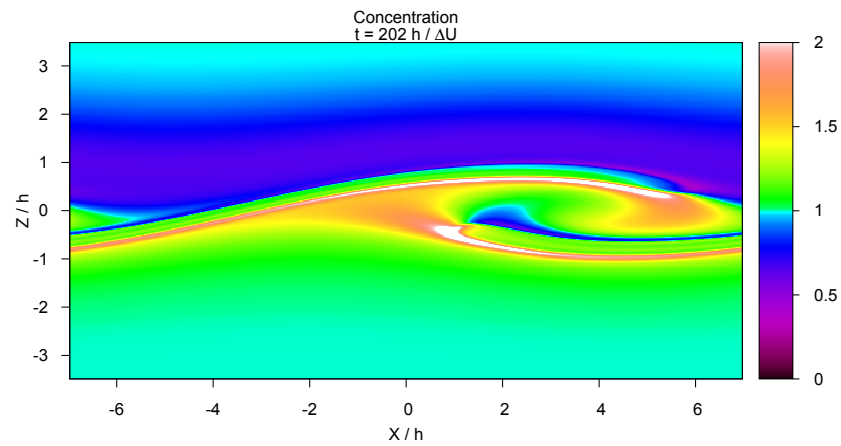
The concentration maximum in the braid region is a direct analogue of the quasi steady state (2.14) in the initial shear layer. When the concentration of shear in the braid causes gyrotactic instability $BS > 1$, the mean orientation field oscillates, causing small scale convergences and divergences in the biological flux. During the initial growth of the Kelvin-Helmholtz instability, the vorticity field has a clearly defined maximum in the braid regions, and the resulting rotation appears in Figure 2.7b as expanding rings of rapidly changing orientation.

In contrast, the maximum concentration in the billow is not dependent on the value of BS exceeding a threshold. Trapping inside the billows depends on the circulation velocity exceeding V_s . Vorticity in the billows is sufficiently uniform that the orientation of organisms trapped inside remains close to the equilibrium value given by (2.8). This situation is analogous to the trapping mechanism described by Stommel (1949).

2.3.3 Pathways to trapping

The organism distribution adjusts first to the initial flow, and then to the developing instability. The orientation in the shear layer rapidly adjusts, causing a convergence of biological flux below the center of the shear layer and a divergence above. The initial uniform distribution of organisms first equilibrates to the mean flow (2.4), which for gyrotactically stable condition ($BS \leq 1$) resembles Figure 2.2 with a transient rarefaction that is advected upward with velocity V_s . The area of increasing concentration remains at a constant depth while the area of rarefaction moves upward and is broader (Figure 2.8). As the area of decreased concentration moves away from the shear layer the vertical profile of concentration becomes similar to the steady state solution (2.14). Figure 2.8 shows a fit to the approximation. The area of rarefaction above the shear layer is due to the initial

(a)



(b)

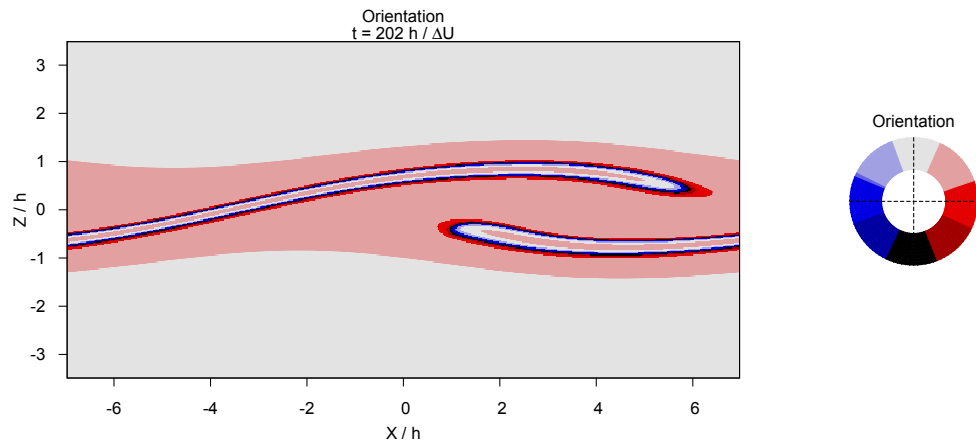


Figure 2.7: Concentration(a) and Orientation(b) fields from run k at the time of fastest aggregation. Dark blue outlines the region in which cells are rotating due to gyrotactic instability. The region shown includes only the central half of the vertical domain.

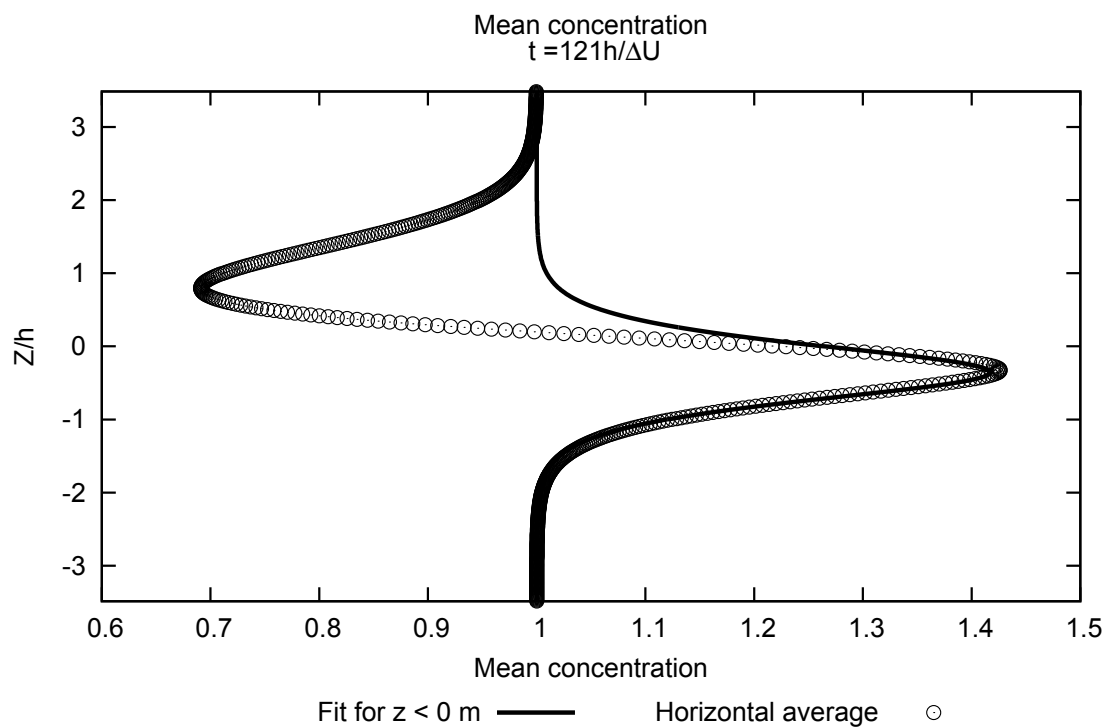


Figure 2.8: Mean concentration field \bar{c} from continuum run k once it has reached a pseudo-steady state, fit with the steady state solution (2.14). Fit is only for the profile below the center of the shear layer $z = 0$. Fit parameters are gyrotactic instability $BS = .7085(5)$, layer width $h = 0.920(4)/h_0$, and a vertical offset $z_0 = 0.1(5)/h_0$. The region shown includes only the central half of the vertical domain.

concentration and orientation differing from the equilibrium distributions of the initial flow. In real flows the shear would be developed over time instead of being imposed instantly, this spin-up would diminish the rarefaction as the flux imbalance at the top and bottom of the shear layer would be smaller during the acceleration phase.

Subsequently trapping can occur via either of two distinct mechanisms. As the billows overturn there is an increase in the vorticity in the braid region (Corcos and Sherman, 1976; Smyth, 2003). When the vorticity at the braid is sufficient to cause gyrotactic instability ($BS > 1$), the organisms tumble and are advected toward the billows by the strained velocity field. Once the billows overturn they form vortices which trap organisms by virtue of their vertical velocity as described in section 2.3.2.

2.3.4 Model comparison

Figures 2.4 and 2.7 show the concentration and orientation computed at the same time via two different biological models (see section 2.2.2.1, and 2.2.2.2). Qualitatively, the results of the two models agree quite strongly. Both exhibit an initial equilibration to the laminar shear layer similar to the steady state approximation. As the instability grows there is a further concentration of organisms. The geometry of the Kelvin-Helmholtz billow train is highlighted in both the particle and continuum models with the thinnest regions coinciding with the braids and a region of vortex trapping slightly offset from the billows.

For a quantitative comparison of the two biological models, a vertical concentration profile is constructed using binned averages (Figure 2.9). The particle counts are discrete events and Poisson statistics (Bevington and Robinson, 1969) are used to estimate the uncertainty of the amount in each bin. In contrast, the continuum model is averaged to the same resolution with uncertainty given by standard deviation of the mean. Both show a 30% increase in the horizontally averaged concentration at the center of the shear layer (Figure 2.9). The two low-concentration bands, as well as the higher mean concentration at the center of the shear layer are easily seen in the average, and support the interaction of gyrotaxis with a growing Kelvin-Helmholtz instability as a plausible mechanism of concentrated layer formation.

The continuum model includes an artificial diffusion term that is not present in the particle model. The regions of (statistically) significant discrepancies coincide with the regions where there

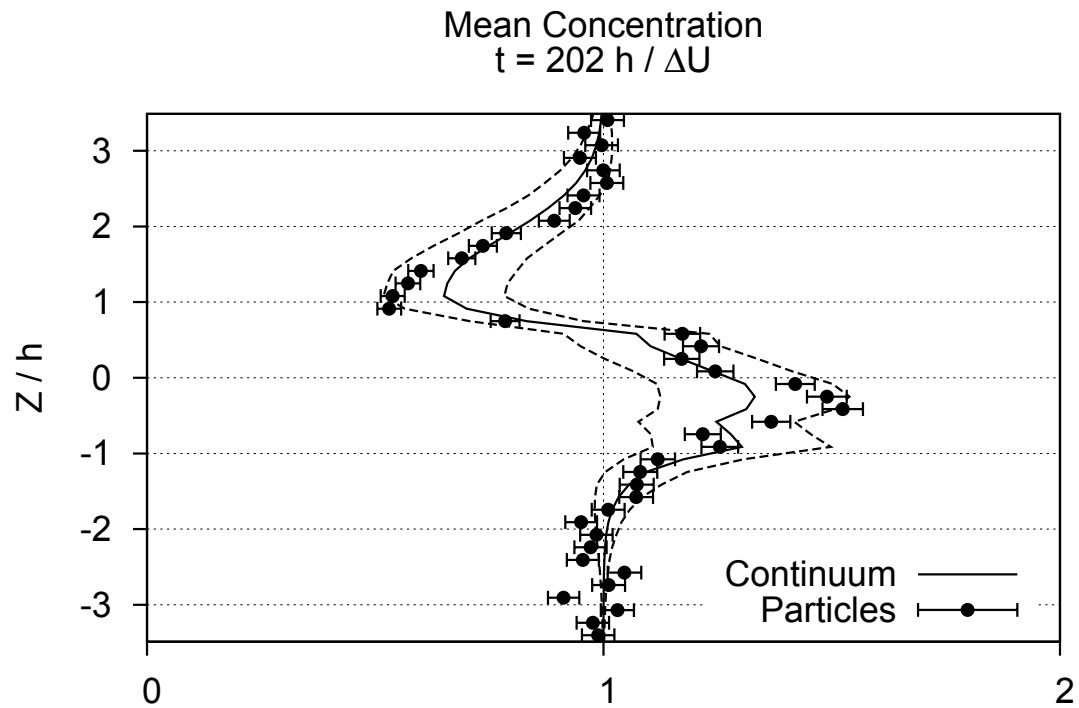


Figure 2.9: Concentration in horizontally averaged bins for particle and continuum models from run k at the time of fastest aggregation. The region shown includes only the central half of the vertical domain.

are large gradients in the mean concentration $\partial\bar{c}/\partial z$ and result from this diffusive term.

2.3.5 Dependence of aggregation rate on initial conditions

The figure of merit we chose to follow the evolution of the biological concentration is the maximum concentration c_{\max} over x and z at a given time. The aggregation rate $dc_{\max}/d\tau$, where time has been scaled by the shear $\tau = t\Delta U_0/h_0$, has a local maximum near the first overturn of the growing Kelvin-Helmholtz billow. The aggregation of the gyrotactic organisms is driven by a convergence in the biological flux field.

$$\frac{dc_{\max}}{d\tau} \sim h_0 \nabla_i c V_b p_i \quad (2.21)$$

This convergence occurs in the smallest biological features where up-gradient flux due to motility is countered by diffusive fluxes. The resultant convergence may be scaled as

$$\frac{dc_{\max}}{d\tau} \sim V_b^2 \text{Re}. \quad (2.22)$$

By translating the graphs of aggregation rate by the time of maximum aggregation and scaling by $V_b^2 \text{Re}$, the various curves can be made to collapse (Figure 2.10). This composite curve shows that the total change in concentration over the Kelvin-Helmholtz event is a factor of order $10 \times V_b^2 \text{Re}$. For oceanic values $V_b \sim 10^{-3}$ and $\text{Re} \sim 10^6$ the predicted layers show concentration increasing by a factor of 10. This concentration factor easily satisfies criterion 3 of Sullivan et al. (2010b).

2.4 DISCUSSION

In this series of simulations we have shown that a pre-turbulent Kelvin-Helmholtz instability enhances the ability of a shear layer to retain gyrotactic organisms. A continuum model is introduced which can smoothly evolve the orientation through gyrotactic instability with the addition of a diffusivity to ensure numerical stability. Comparison with a diffusionless particle model shows that the evolution of the concentration in the continuum model is not significantly altered by diffusivity (Figure 2.9).

As the Kelvin-Helmholtz instability develops, the models reveal two distinct trapping mecha-

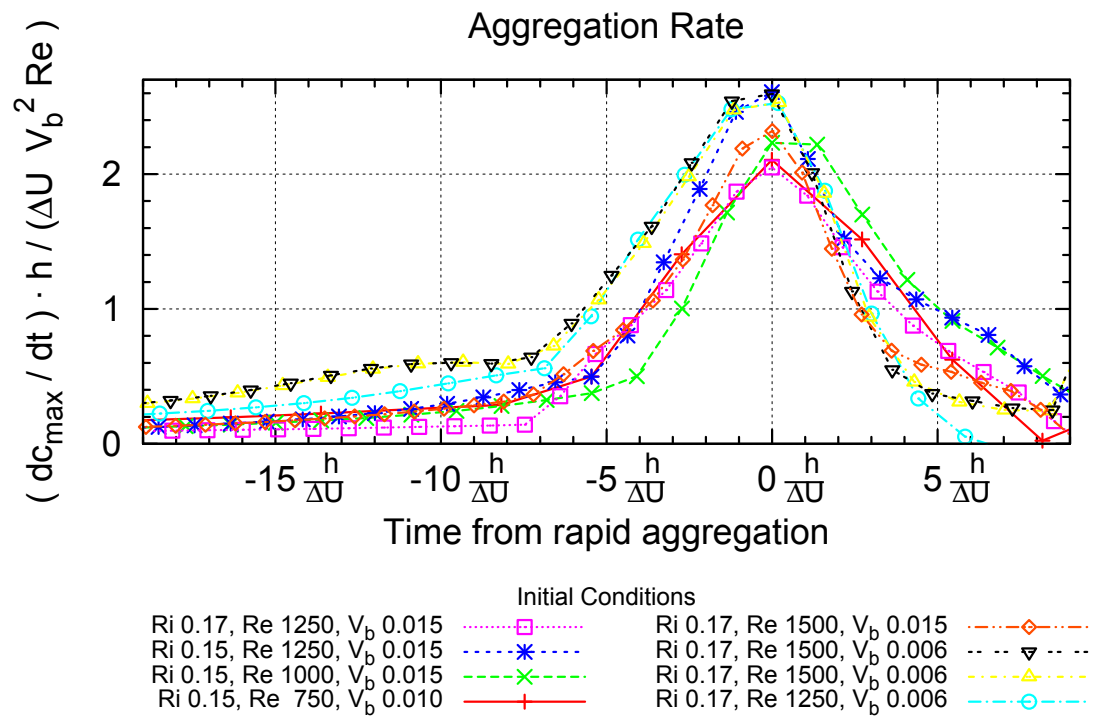


Figure 2.10: Aggregation scaled by $V_b^2 Re$ where time is scaled by the shear $\tau = h/\Delta U$ and measured from the time of fastest aggregation

nisms that act in different regions of the shear layer.

1. Shear in the braids causes the organisms to become gyrotactically unstable (Durham et al., 2009), thus creating thin layers of highly elevated concentration.
2. Large vertical velocities within the billows detain the upward progress of organisms via the suspension mechanism of Stommel (1949)

A scaling relationship (2.22) is derived such that the aggregation rate, scaled by the maximum shear, is proportional to the Reynolds number Re and the square of the relative motility V_b . The net increase in concentration is estimated as $10ReV_b^2$. This is motivated by an approximation of (2.21) as $V_b h_0 \|\vec{\nabla} c\|$ where the gradient $\vec{\nabla} c$ is set by the balance between diffusive $\Delta U_0 V_b c$ and advective $D\vec{\nabla} c$ fluxes. The concentration c is assumed to be of order 1.

This model assumes the organisms are smaller than the Kolmogorov scale η . The size of organisms for which the model assumptions hold is $\ll 1$ mm (A.3). Near the surface of the ocean, observed dissipation rates $\epsilon \lesssim 10^{-4}$ W/kg (e.g., Soloviev and Lukas, 2003) imply $\eta \gtrsim 1$ mm. The findings are more generally applicable as a result of the weak influence of an organism's ellipticity on its orientation in a growing Kelvin-Helmholtz instability (A.2).

We close by summarizing some quantitative aspects of our results in the context of the Sullivan et al. (2010b) criteria for thin layer identification cited in the Introduction to this paper.

1. The phase of the K-H life cycle in which braids grow, and hence concentration in braids increases rapidly, extends over a time $\sim 10h/\Delta U$. For example, if $h = 0.1$ m and $\Delta U = 0.01$ m/s, the braid growth phase lasts for only a few minutes. Trapping within the billows persists over a similarly short time. These are, of course, examples of brief intervals in a much longer mixing event throughout which thin layers might be created, reinforced, or dispersed.
2. Vertical layer thickness starts off at h_0 . The shear layer ultimately thickens, and equilibrates at a thickness $0.32h_0/Ri_0$ when the turbulence extinction criterion $Ri = 0.32$ is reached (Thorpe, 1973; Smyth et al., 2001). If Ri starts off at 0.16, for example, and the initial layer thickness is 0.1 m, the thickness will double to 0.2 m. In the braids, however, this thickness decreases to h_0/\sqrt{RePr} , or about 1 mm.

3. The maximum local concentration increase at the time of fastest aggregation is a factor of 2.7 (Figure 2.7) Horizontally averaged concentration increases by a factor of 1.5 at the time of most rapid aggregation (Figure 2.9), and increases to 2 in the second half of the aggregation phase ($0 < t < 10h/\Delta U$ in Figure 2.10). Therefore locally and in the horizontal mean the criterion suggested by Sullivan et al. (2010b) is marginally satisfied. When extrapolated to oceanic parameter regimes the concentration increase is $O(10)$.

The aggregation events modeled here are only brief episodes in a considerably longer process that will be amenable to direct simulation in the near future. The net effect of many episodes of billow and braid growth can not be simply extrapolated from these simulations as the decay of the K-H instability is inherently three-dimensional. To compare these results with observed aggregations, the spin-up of the shear layer and the anisotropic mixing during the decay of the instability must be addressed. In particular, the turbulent mixing following the initial K-H instability could cause sufficient vertical dispersion that the aggregation criterion of Sullivan et al. (2010b) are not met.

3 KELVIN-HELMHOLTZ OVERTURN BOUNDARY IN VISCOUS FLOWS

Here I explore the conditions where instability grows despite the stabilizing influence of viscosity and diffusion. I propose a criterion for mixing which requires instabilities attain sufficient magnitude that they can engender smaller instabilities. I use diffusion of the mean flow, assuming uniform diffusivity, to constrain the growth time. Results from linear stability analysis give the rate at which an initial perturbation will grow. Typical sizes for initial perturbations are based on the Kolmogorov and Ozmidov length scales.

3.1 INTRODUCTION

Vertical mixing in the world ocean modifies the flux and distribution of small organisms (chapter 2), closes large scale circulation (Munk and Wunsch, 1998; Talley, 2003; Ferrari and Wunsch, 2008) and determines how fresh water inputs are incorporated (Geyer et al., 2010). Near the surface waves and diurnal cycles of heating and cooling maintain a mixed layer but their penetration depth is limited. Away from extended cooling near the poles convection is halted each day with the return of strong solar heating. wave influence is limited by their wavelength. In contrast with the daily cycling of heat flux momentum fluxes in the ocean can persist for days at the ocean surface. Away from the equator varying winds couple with near inertial waves transferring energy and momentum into the stratified interior (Van Meurs, 1998; Alford, 2003). The difficulty of surface buoyancy forcing reaching the interior is exemplified by the extreme, nearly singular, conditions found where this is not the case (e.g. in polynyas Smith et al., 1990; Mundy and Barber, 2001; Moore et al., 2002).

In free stratified shear layers there is a well studied family of linear instabilities which grow exponentially (Miles, 1961; Howard, 1961). When the stratification is sufficiently weak relative to the shear the flow is unstable to perturbations in a range of wave numbers (Hazel, 1972). As time progresses the exponential growth quickly causes the fastest growing wave number to dominate the flow. The growing perturbation kinetic energy becomes comparable to the initial state, at least for a given range of depths. If it grows large enough the perturbation itself gives rise to secondary instabilities (Caulfield and Peltier, 2000; Smyth, 2003). The details of this transition

are in and of themselves interesting involving both a self interaction causing successive doubling of wave number as well as the creation of an orthogonal convective instability. A discrete energy cascade is a possible explanation for the intricate flow geometries observed in geophysical shear flows before they become fully turbulent (Geyer et al., 2010). Whatever the details may be, the rapid increase in wave number associated with secondary instabilities relies on the growth of the initial instability beyond the limits of the linear theory from which it is derived.

When analyzing observed profiles it is useful to distinguish between flows which will and will not undergo mixing. One necessary condition for mixing is the growth of shear instability, this is the foundation of the concept of marginal instability which draws conclusions from the observed distribution of Richardson number (Thorpe and Liu, 2009; Smyth and Moum, 2013). Similar ideas are used to estimate turbulent mixing by comparison with a critical Richardson number (Large et al., 1994). Here we seek to find a stronger limit for the onset of mixing that will include the effect of changing shear layer thickness. To that end I will examine a free shear layer far from vertical boundaries.

3.2 IDEALIZED SHEAR LAYER

A stratified shear layer is idealized as jumps in velocity and density centered at a common depth and undergoing diffusion. The source of the density change may be temperature, salinity, or any other quantity which satisfies a diffusion equation. In the interest of generality all influenced on density ρ will be treated generically as buoyancy

$$b = -g \frac{\rho - \rho_0}{\rho_0} \quad (3.1)$$

where ρ_0 is a representative density and with a constant diffusivity κ . Before discussing two dimensional dynamic instability it is useful to examine the evolution of the one dimensional profiles of velocity and buoyancy assuming constant, though not necessarily equal, diffusion coefficients for momentum ν and buoyancy κ . In this idealized shear layer all the changes in velocity and density are concentrated in well defined region. The initial vertical extent of this region defines a vertical length scale h_0 . The difference in velocity and buoyancy each have scales ΔU and ΔB respectively.

The five parameters are sufficient to determine the form of the profiles of velocity and buoyancy

$$u(z, t) = \Delta U \operatorname{erf} \frac{\sqrt{\pi}}{2} \frac{z}{h_u(t)} \quad (3.2)$$

$$h_u(t) = h_0 \sqrt{1 + \frac{\pi \nu}{h^2} t} \quad (3.3)$$

$$b(z, t) = \Delta B \operatorname{erf} \frac{\sqrt{\pi}}{2} \frac{z}{h_b(t)} \quad (3.4)$$

$$h_b(t) = h_0 \sqrt{1 + \frac{\pi \kappa}{h^2} t} \quad (3.5)$$

for the mean flow. In an attempt to reduce the parameter space I reduce the problem in terms of non-dimensional parameters (Tennekes and Lumley, 1972), in this case using Prandtl number $\operatorname{Pr} = \nu/\kappa$, initial Reynolds number $\operatorname{Re}_0 = \Delta U h_0/\nu$, and initial Richardson number $\operatorname{Ri}_0 = \Delta B h_0/(\Delta U)^2$. To take full advantage of the non-dimensional quantities it is useful to define non-dimensional time $t' = t\Delta U/h$ and distance $z' = z/h$. In terms of these dimensionless quantities equations 3.2-3.5 become

$$u'(z', t') = \operatorname{erf} \frac{\sqrt{\pi}}{2} \frac{z'}{h'_u(t')} \quad (3.6)$$

$$h'_u(t') = \sqrt{1 + \frac{\pi}{\operatorname{Re}_0} t'} \quad (3.7)$$

$$b'(z', t') = \operatorname{Ri}_0 \operatorname{erf} \frac{\sqrt{\pi}}{2} \frac{z'}{h'_b(t')} \quad (3.8)$$

$$h'_b(t') = \sqrt{1 + \frac{\pi}{\operatorname{Re}_0 \operatorname{Pr}} t'} \quad (3.9)$$

and the profiles are shown in figure 3.1.

By construction the non-dimensional profiles span velocity and buoyancy differences of 2 and $2\operatorname{Ri}_0$. Shear and stratification are simple functions $\partial_z u' = h'_u{}^{-1}$, and $\partial_z b' = \operatorname{Ri}_0/h'_b$. The Richardson number

$$\operatorname{Ri}(t'; \operatorname{Ri}_0, \operatorname{Re}_0, \operatorname{Pr}) = \operatorname{Ri}_0 \frac{1 + \frac{\pi}{\operatorname{Re}_0} t'}{\sqrt{1 + \frac{\pi}{\operatorname{Re}_0 \operatorname{Pr}} t'}} \quad (3.10)$$

grows over time and depends on all three non-dimensional parameters Pr , Re_0 , and Ri_0 . This is partially because for $\operatorname{Pr} \neq 1$ the length scales of the two profiles diverge. Of note is that Ri increases in the long time limit even when density diffuses rapidly $\operatorname{Pr} \ll 1$.

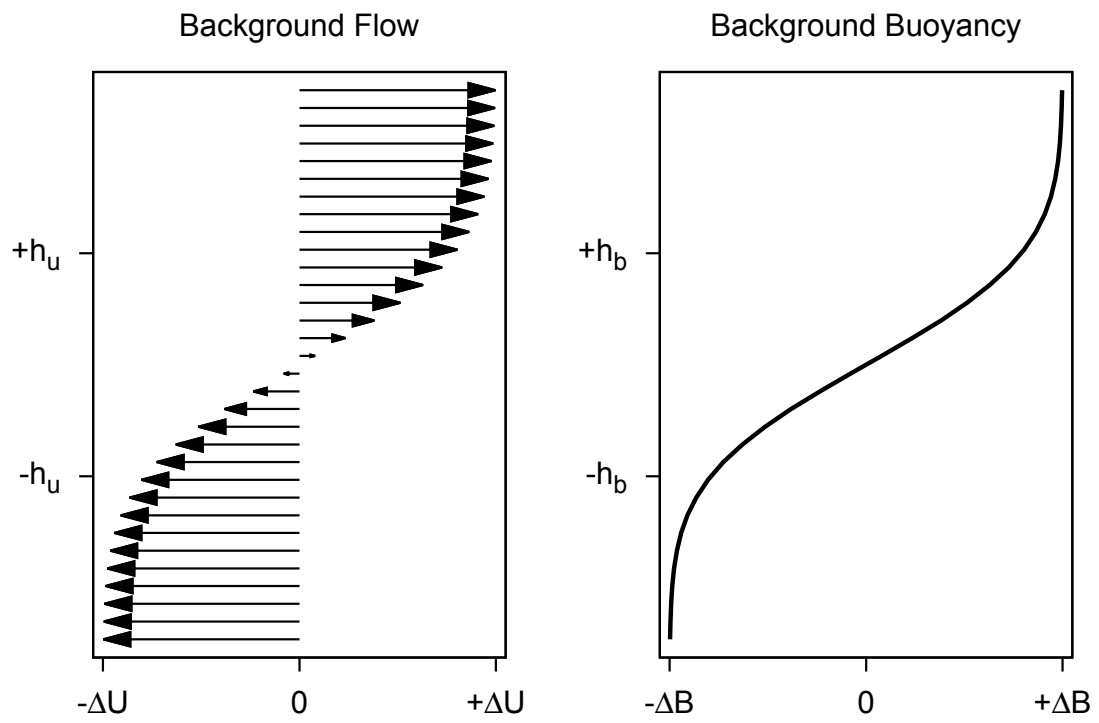


Figure 3.1: Background flow profiles

3.3 THE INSTABILITY

With the background flow well described in dimensionless units it can be easily linked to linear instability theory. The growth of instabilities imposes a strong upper bound on $\text{Ri} \leq \text{Ri}_c = 1/4$. This critical Richardson number Ri_c combined with (3.10) implies a finite time available for the growth of shear instability. Hazel (1972) calculated growth rates of modes for a range of Richardson numbers which can be used to estimate the total amplification possible in a shear layer. In the vicinity of the critical Richardson number the growth rate is well approximated by $\sigma \approx k(\text{Ri}_c - \text{Ri}_0)$, $k = 0.7588\Delta U/h$ (Hazel, 1972). The linear perturbations initially grow exponentially $\propto e^{\sigma' t'}$, where $\sigma' = h\sigma/\Delta U$.

3.3.1 OvertURNS

OvertURNS and mixing necessarily exist beyond the limits of linear instability theory. The predictions of exponential growth require deviations to be small relative to the background flow. In the linearized theory all measures of the perturbation magnitude (e.g. velocity, buoyancy, kinetic energy) are linked, this allows for many equivalent formulations of the perturbation parameter. For ease in visualization I choose to use isopycnal displacement $\|\Delta z'\|$ to quantify the size of the perturbation. Using the metric linear perturbation theory is valid for instabilities whose isopycnal displacements are smaller (usually much smaller) than the width of the shear layer. This criterion also provides a convenient division between small growing instabilities $\|\Delta z'\| < 1$ and large non-linear instabilities $\|\Delta z'\| > 1$. Using the growth rate from Hazel (1972), an initial perturbation $\Delta z'_0$ and a final perturbation $\|\Delta z'\| = 1$ gives a growth time

$$T \geq \frac{-\ln \|\Delta z'_0\|}{k(\text{Ri}_c - \text{Ri}_0)} \quad (3.11)$$

where I will focus on the equality with the goal of finding sufficient (but not necessary) conditions for an overturn.

3.3.2 Initial Perturbations

An important aspect of linear instabilities is that they act to selectively amplify preexisting motions of the fluid. To use (3.11) an additional set of assumptions must be used to posit what

deviations from the mean state $\|\Delta z'_0\|$ are initially present in the shear layer. Combining (3.10) and (3.11) with the requirement that $\text{Ri}_c \geq \text{Ri}(T')$ gives

$$\text{Ri}_c \geq \text{Ri}_0 \frac{1 - \frac{\pi}{\text{Re}_0} \frac{\ln \|\Delta z'_0\|}{k(\text{Ri}_c - \text{Ri}_0)}}{\sqrt{1 - \frac{\pi}{\text{Re}_0 \text{Pr}} \frac{\ln \|\Delta z'_0\|}{k(\text{Ri}_c - \text{Ri}_0)}}} \quad (3.12)$$

as a criterion for the development of overturns dependent on the three non-dimensional parameters and the initial size of the perturbation.

For stratified fluid motion here are two natural scales that are relevant, the Ozmidov $\ell'_O = \text{Ri}_0^{-3/4}$ and the Kolmogorov $\ell'_K = \text{Re}_0^{-3/4}$. The Ozmidov scale is less attractive, it represents the largest vertical motions in stratified flow and perturbations at that scale are essentially non-linear already. The Kolmogorov scale, especially in the large Re_0 limit, satisfies the smallness condition required by the perturbation theory as this scale is intended to represent the size of motions which are strongly damped by viscosity. For completeness I will compute some quantities with a hybrid perturbation size

$$\Delta z_0(a) = \ell'_K{}^a \ell'_O{}^{1-a} = \text{Re}_0^{-\frac{3}{4}a} \text{Ri}_0^{-\frac{3}{4}(1-a)} \quad (3.13)$$

where a is a free parameter allowing smooth variation from ℓ'_O when $a = 0$ to ℓ'_K for $a = 1$. With a set of initial displacements the division suggested by (3.12) is plotted in figure 3.2.

3.3.3 Limiting Cases

Using $\Delta z'_0 = \text{Re}^{-\frac{3}{4}}$ (i.e. Kolmogorov scale), equation (3.12) has natural variables $\frac{4k\text{Ri}_c}{3\pi} \frac{\text{Re}_0}{\ln \text{Re}_0}$ and $\frac{\text{Ri}_c}{\text{Ri}_c - \text{Ri}_0}$. Even in those variables the form of (3.12) is misleadingly complex, as in most geophysical flows $\text{Re}_0 \gg 1$. Expanding about small quantities $\frac{\text{Ri}_c - \text{Ri}_0}{\text{Ri}_c}$ and Re_0^{-1} yields a significant simplification

$$\frac{4k\text{Ri}_c}{3\pi} \frac{\text{Re}_0}{\ln \text{Re}_0} \approx \begin{cases} \frac{\text{Pr} - \frac{1}{2}}{\text{Pr}} \left(\frac{\text{Ri}_c}{\text{Ri}_c - \text{Ri}_0} \right)^2 & \text{Pr} > \frac{1}{2} \\ \left(\frac{\text{Ri}_c}{\text{Ri}_c - \text{Ri}_0} \right)^{\frac{3}{2}} & \text{Pr} = \frac{1}{2} \\ \frac{\text{Pr}}{1 - 2\text{Pr}} \left(\frac{\text{Ri}_c}{\text{Ri}_c - \text{Ri}_0} \right) & \text{Pr} < \frac{1}{2} \end{cases} \quad (3.14)$$

The discontinuity at Pr arises from the binomial expansion of the square root in the denominator.

For slowly diffusing buoyancy sources, such as salt (and to a lesser extent heat) in oceanic flows,

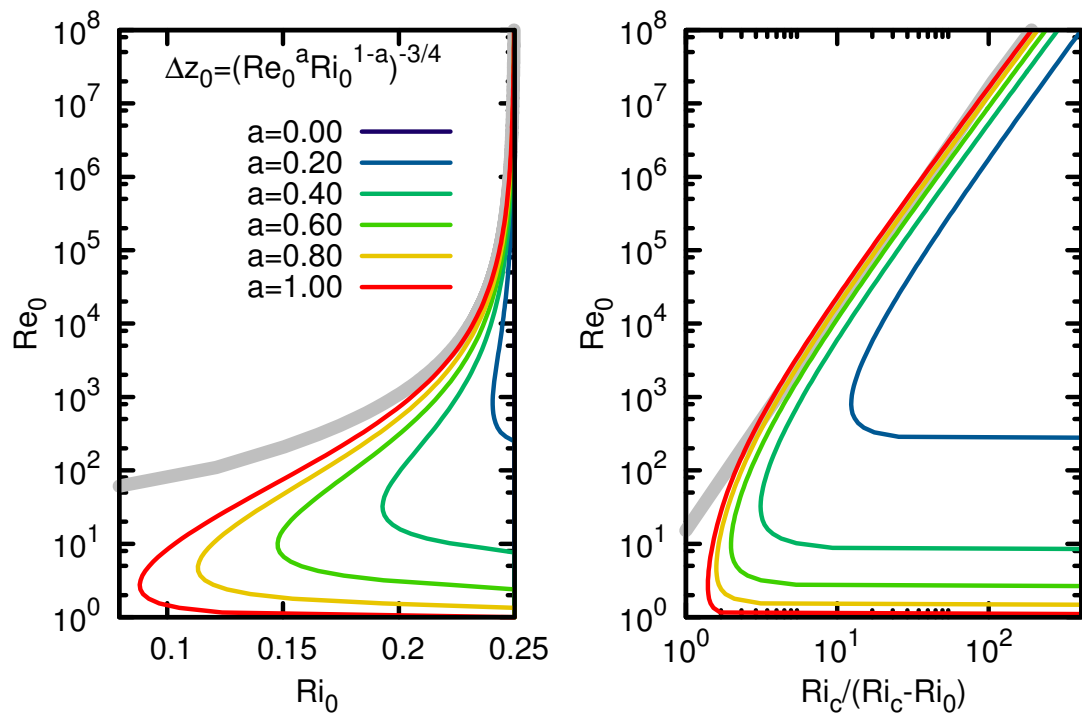


Figure 3.2: K-H billows cannot form to the right of each curve. All figures show results for $Pr = 1$ for comparison. The limiting curve is drawn in grey.

$\text{Pr} \gg 1$ a further simplification

$$\frac{4k\text{Ri}_c}{3\pi} \frac{\text{Re}_0}{\ln \text{Re}_0} \approx \left(\frac{\text{Ri}_c}{\text{Ri}_c - \text{Ri}_0} \right)^2 \quad (3.15)$$

which is plotted in grey in figure 3.2. Similarly for rapidly diffusing buoyancy sources $\text{Pr} \ll 1$ (heat in liquid mercury) the simplification allows for Ri_0 to be solved for

$$\text{Ri}_0 \approx \text{Ri}_c - \text{Pr} \frac{3\pi}{4k} \frac{\ln \text{Re}_0}{\text{Re}_0} \quad (3.16)$$

or in extreme limit of low Prandtl number or high Reynolds number $\text{Ri}_0 \approx \text{Ri}_c$.

3.4 CONCLUSIONS

The stronger constraint on mixing in unstable shear layers will help distinguish instability from turbulence. In particular an explicit criterion (3.14) is proposed. This stronger requirement for mixing is of use for the planning of modeling studies which are limited to intermediate Reynolds number to assure the development of a mixing event for given initial conditions (for example in chapter 2). A possible extension would parameterize preexisting turbulence by replacing molecular diffusivity ν and κ with effective turbulent diffusivity. The choice of turbulence parameterization is not straight forward but could be linked to observations of the internal wave field. For example estimating an effective Reynolds number by equating the effective Kolmogorv scale ℓ_k with the amplitude of internal wave displacements a wavelengths near the fastest growing mode $\lambda \approx 14h$ (Hazel, 1972).

4 OCEANIC TURBULENT ENERGY BUDGET USING LARGE EDDY SIMULATION OF
A WIND EVENT DURING DYNAMO

Martín S. Hoecker-Martínez,

William D. Smyth,

Eric D. Skyllingstad

Journal of Physical Oceanography

American Meteorological Society

45 Beacon Street

Boston, MA 02108-3693

#??

A Large Eddy Simulation (LES), driven by surface fluxes observed from R/V Revelle during boreal fall, 2011 in the Indian Ocean at 0°N , 80.5°E , was performed to identify the dominant processes governing subsurface turbulence and to quantify the resulting vertical property fluxes. In the simulation, wind accelerated the mixed layer, and shear mixed the momentum downward, deepening the mixed layer base. Turbulent kinetic energy gains due to shear production and Langmuir circulations are opposed by stirring the density field (buoyancy production) and frictional losses (dissipation). Strongest stirring of buoyancy follows precipitation events and penetrates to the base of the mixed layer.

We focus on the wind burst from November 24, 2011 where strong wind and wave forcing were observed. The LES model uses the Craik-Leibovich equations, adding Langmuir turbulence to the physics. The turbulent kinetic energy budget shows that waves influence only the uppermost few meters of the ocean. Below the wave-energized region, shear instability responds to the integrated momentum flux into the mixed layer, lagging the initial onset of the storm. Shear below the mixed layer persists after the storm has weakened and decelerates the surface jet slowly (compared with the acceleration at the peak of the storm). Slow loss of momentum from the mixed layer extends the effect of the surface wind burst by energizing the fluid at the base of the mixed layer, thereby prolonging heat uptake due to the storm. Ocean turbulence and air-sea fluxes contribute to the cooling of the mixed layer approximately in the ratio 1:3, consistent with observations.

4.1 INTRODUCTION

The intra-seasonal variability of SST, winds, and outgoing radiation in the equatorial eastern Indian Ocean is dominated by the 30-90 day period of the Madden Julian Oscillation (MJO; Hendon and Glick, 1997; Wheeler and Hendon, 2004; de Szoeke et al., 2015). The active phase of the MJO features an area of increased westerly wind anomalies (Madden and Julian, 1971, 1972) near the surface and strong precipitation at the equator propagating eastward at $\sim 5\text{m/s}$ (Zhang, 2005). These westerly wind anomalies, or wind bursts, last only 1-3 days (Zhang, 2013). Despite their short duration these wind bursts can account for the majority of the climatological momentum flux into the ocean. The mean wind forcing is weak $\lesssim 0.05\text{Pa}$ (Wyrтки, 1973; Schott and McCreary Jr., 2001) and highly variable. During a westerly wind burst, surface stress is typically $\sim 0.5\text{Pa}$ and

can reach values $> 0.8\text{Pa}$, in 1min averages. In addition to dominating the momentum exchange, the active phase of the MJO changes the nature of the air-sea heat and freshwater exchanges due to increased latent heat flux and precipitation at the surface(de Szoeke et al., 2015).

The intense surface fluxes associated with a westerly wind burst change the physics of heat, salt, and momentum transport within and below the ocean mixed layer. In the absence MJO suppressed phase, heat exchanges are dominated by a diurnal cycle of strong daytime solar heating $\sim 400\text{W/m}^2$ and weak $\lesssim 100\text{W/m}^2$ cooling with weak precipitation and winds (Moum et al., 2014; de Szoeke et al., 2015). In addition to direct heat, salt, and momentum fluxes, mixed layer transports are partially mediated by surface waves. Typical waves in the equatorial Indian Ocean are too shallow, 1–2m high with periods $> 10\text{sec}$ (Young, 1999; Chen et al., 2002; Sterl and Caires, 2005), to drive significant motion in the mixed layer. During a westerly wind burst, in addition to strong momentum flux, there is strong precipitation, net surface cooling of 300W/m^2 , and wave heights increasing to $\gtrsim 1.5\text{m}$ with periods as short as 3sec (Moum et al., 2014). The strong fluxes freshen, cool, and accelerate the surface water, while steep waves, shear, and buoyancy fluxes energize mixing mechanisms (figure 4.1) and exchange salt, heat and momentum with deeper water previously inaccessible to air-sea interaction. Observations during a westerly wind burst show the potential influence of a barrier layer on the exchange of heat across the mixed layer base (Chi et al., 2014; Moum et al., 2014).

There is some modulation of MJO properties associated with changes in sea surface temperature (SST), but a clear causal relationship has yet to be demonstrated (Lau and Waliser, 2012). Some theories of the MJO attempt include theses surface fluxes (Emanuel, 1987; Neelin et al., 1987) or parameterize them as damping term (Chang, 1977). Previous studies of the surface mixed layer heat budget during DYNAMO show a strong turbulent heat flux at the mixed layer base associated with westerly wind bursts (Chi et al., 2014).

In this study, our main goals are (1) to identify the most important subsurface mixing mechanisms and (2) to assess the relative importance of subsurface and atmospheric processes in determining the surface cooling that damps the storm. To this end, we explore atmosphere-ocean feedbacks and subsurface mixing processes in the MJO active phase using a Large Eddy Simulation (LES).

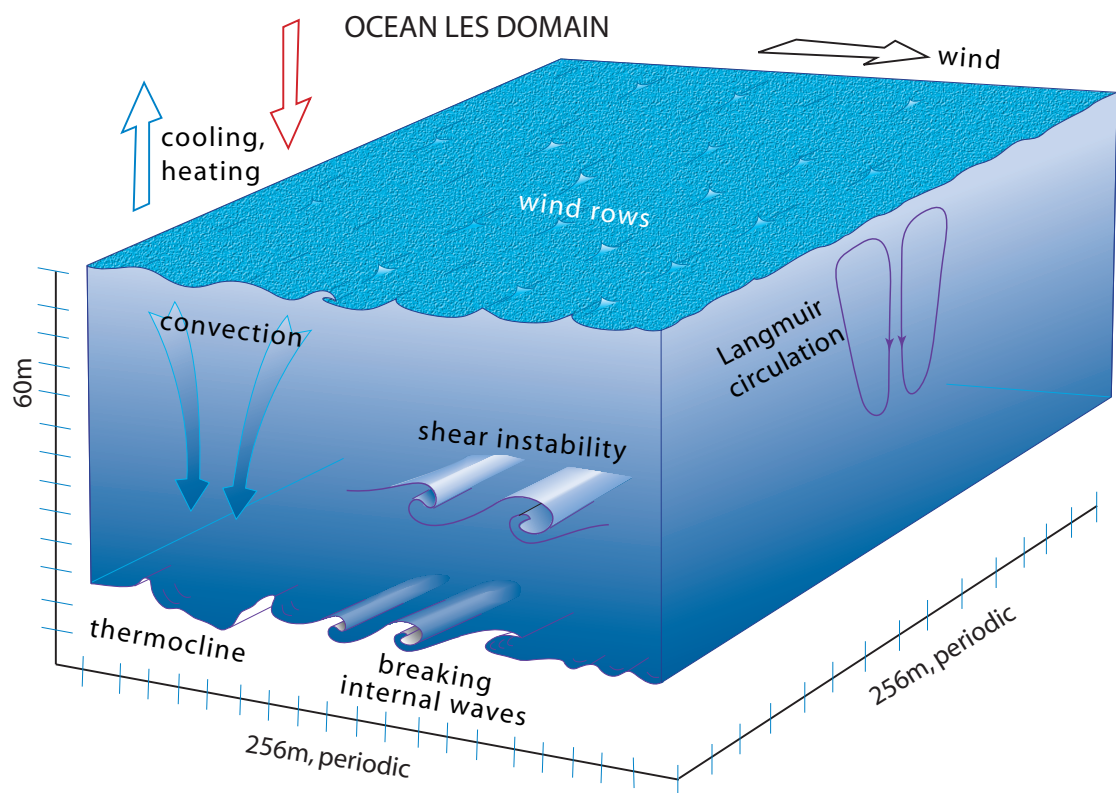


Figure 4.1: Schematic of the upper ocean LES model domain showing surface forcing and subsurface mixing processes.

After initial applications to the atmospheric boundary layer (Deardorff, 1972), LES was adapted for the ocean in the 1990s (Skylingstad and Denbo, 1995) and has been used in numerous studies since. (Skylingstad et al., 1999, ; hereafter S99) explored the limits of the technique by comparing LES-derived turbulence statistics with microstructure measurements in the context of a westerly wind burst. Several modeling studies using idealized (McWilliams et al., 1997; Wang and Müller, 2002; Harcourt and D’Asaro, 2008; Grant and Belcher, 2009; Noh et al., 2011) and empirical (Kukulka et al., 2009, 2010) forcing have contributed to the general understanding of upper ocean physics. LES of shallow mixed layers driven by strong wind forcing show that turbulence near the surface is driven mainly by shear associated with the Stokes drift of the surface waves (Langmuir turbulence; McWilliams et al., 1997). Langmuir circulation transports momentum and buoyancy more quickly than a simple shear driven mixed layer (Kukulka et al., 2009, 2010), rapidly mixing away shear near the surface (Noh et al., 2011). Away from the surface, Langmuir turbulence relies on the inertia of vertical motions of Langmuir cells (Grant and Belcher, 2009) because the driving Stokes shear decays rapidly with depth, unlike turbulence driven by convective or shear instability which need not depend on depth (Thorpe, 2004). The influence of the Langmuir turbulence is present in much of the mixed layer with the effect strongest in shallow mixed layers with weak underlying stratification (Noh et al., 2011). Langmuir turbulence may deposit momentum at the mixed layer base, setting the stage for enhanced shear production (Kukulka et al., 2010)

Observational estimates of surface heat flux, precipitation, and wind stress can be used to drive ocean LES of a dynamically evolving mixed layer and inform the analysis of the subsurface mixing mechanisms of a specific event. S99 did this for a westerly wind burst observed in the western Pacific using measurements from the Coupled Ocean-Atmosphere Response Experiment (COARE). Here we use the same approach to examine mixing during the DYNAMO westerly wind burst that occurred on November 24, 2011. From the model results we identify the primary mechanisms responsible for turbulence and quantify the time and depth dependence of the resulting fluxes driven by meteorological and oceanographic observations taken during the Dynamics of the Madden-Julian Oscillation (DYNAMO) field campaign (Yoneyama et al., 2013; Moum et al., 2014; de Szoeke et al., 2015), as well as concurrent measurements from the nearby RAMA mooring (the Research Moored Array for African-Asian-Australian Monsoon Analysis and prediction; McPhaden et al., 2009) to

estimate the ocean state and surface fluxes before and during a westerly wind burst.

We will first discuss how the boundary and initial conditions were extracted from the observational record (section 4.2) and estimate the relative influence of convection and Langmuir turbulence on the mixed layer before summarizing the numerical model (section 4.3). The simulation is used to partition turbulent energy production among Stokes, shear, and buoyancy driven production (section 4.44.4.2). Special attention is given to shear instability below the mixed layer (section 4.44.4.3). Vertical transports of momentum, heat, and salt are compared to the surface forcing (section 4.44.4.4). Results are compared with the COARE wind burst (section 4.5) and conclusions are summarized in section 4.6.

4.2 INITIAL OCEAN STATE AND AIR-SEA FLUXES DURING THE WIND BURST

Vertical profiles of horizontal velocity are obtained from the acoustic Doppler current profiler at the nearby equatorial RAMA mooring (McPhaden et al., 2009) at 80.5 E. Uniform currents are assumed above 12m due to the unreliability of near surface data. The Chameleon vertical microstructure profiler provides initial mean profiles of salinity and temperature (Moum et al., 1995, 2014; Pujiana et al., 2015). The observed flow field had a strong tidal signature that is not included in the model. To remove the resulting bias, isopycnal averages of velocity, temperature, salinity and depth are computed over the five days preceding the wind burst. The profiles are re-interpolated onto a regular depth grid for use as initial velocity, temperature and salinity profiles. Potential density is calculated using the Gibbs sea water package version 3.02 (McDougall and Barker, 2011) and referenced to surface pressure. Depth conservative temperature T_C , and absolute salinity S_A , as functions of density at surface pressure $\rho(T_C, S_A, P = P_{atm})$ are calculated by interpolating in density using the four nearest points with a cubic polynomial.

After the MJO suppressed phase that preceded the wind burst, the upper ocean was stable and the currents were weak. The initial profiles represent the average of the five days preceding the wind burst as described above (figure 4.2). At 20m there is a pycnocline, due mostly to a stable salinity gradient of $g\beta\partial_z S \sim 4 \times 10^{-4}\text{s}^{-2}$ embedded in weaker $g\alpha\partial_z T \sim 10^{-4}\text{s}^{-2}$ temperature gradient. In this stable halocline there is a maximum in the meridional shear. This pycnocline is the upper edge of a current extending from 20-50m carrying salty water into the southern hemisphere (figure 4.2).

Below the strong halocline, the salinity continues to increase but temperature is the dominant source of density stratification. Salinity reaches a maximum at 50m below which temperature gradient increases to $g\alpha\partial_z T \sim 4 \times 10^{-4}\text{s}^{-2}$. The near-surface current was dominated by its eastward component and exhibited very little shear except at $z = 20\text{m}$ (figure 4.2b, solid line).

Momentum fluxes are taken from one minute average wind speed observations measured aboard R/V Revelle. Surface heat and salt fluxes include contributions from the observed net precipitation and evaporation $P - E$, and the surface heat flux J_0 calculated using the observed winds, humidity, radiative fluxes, and air-sea temperature differential. Observations are converted to surface fluxes using COARE 3.5 rev. 3 (de Szoeke et al., 2015). The processed fluxes are then low pass filtered at one hour.

In situ air sea fluxes (de Szoeke et al., 2015) and subsurface profiles are available from the DYNAMO project from September 2011 through January 2012 while R/V Revelle was on station at 0 N, 80.5 E. The strongest measured heat flux at the base of the ocean mixed layer of the DYNAMO record are associated with the wind burst at the end of November 2011 (Chi et al., 2014). We choose to model the November 24, 2011 westerly wind burst because it exemplifies critical atmosphere-ocean feedbacks and was brief enough to be accessible to high resolution modeling.

The model is initialized on year-day 328 (November 24) at 00:00 UTC, shortly before local sunrise. The previous suppressed phase of the MJO was characterized by weak winds ($\tau \lesssim 0.1 \text{ N/m}^2$) and strong daytime heating ($\sim -400 \text{ W/m}^2$). On November 24 the zonal wind stress increased rapidly to $\tau \sim 0.5 \text{ N/m}^2$ (figure 4.3a) with peaks as high as 0.83 N/m^2 in 1 minute averages. This wind event was accompanied by significant precipitation (15mm/hr) and surface cooling ($+400\text{W/m}^2$) (figure 4.3b). The surface buoyancy flux (figure 4.4b) was dominated by its thermal component ($\sim 10^{-7}\text{m}^2/\text{s}^3$) except during rain squalls ($\sim 10^{-6}\text{m}^2/\text{s}^3$) when the saline component was as great or greater.

During the wind burst, the spectral distribution and vertical attenuation of the short wave radiative heat flux J were measured (Ohlmann, 2011) and found to be nearly constant. These were consistent with the Paulson and Simpson (1977) formula

$$J(z, t) = J(0, t) \left(A_1 e^{-z/\lambda_1} + (1 - A_1) e^{-z/\lambda_2} \right) \quad (4.1)$$

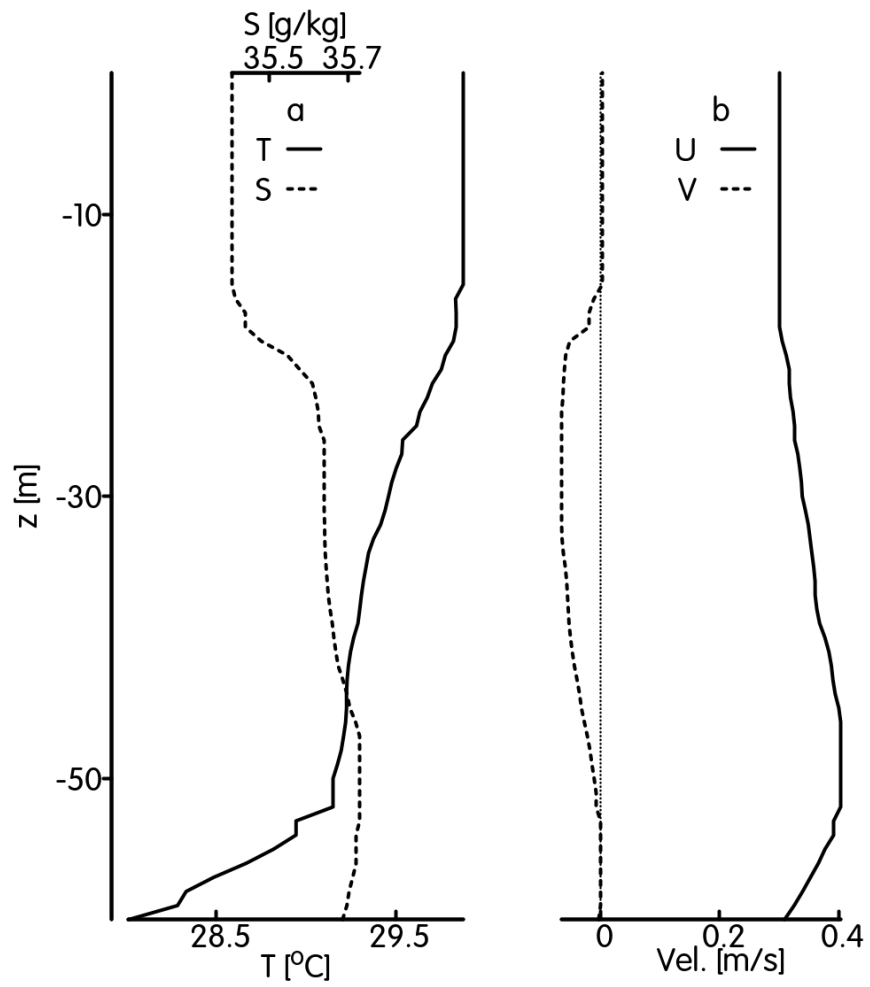


Figure 4.2: Upper ocean conditions prior to the wind burst. (a) Temperature (solid, lower axis) and salinity (dashed, upper axis) scaled to represent equal buoyancy increments, and (b) zonal (solid) and meridional (dashed) velocities

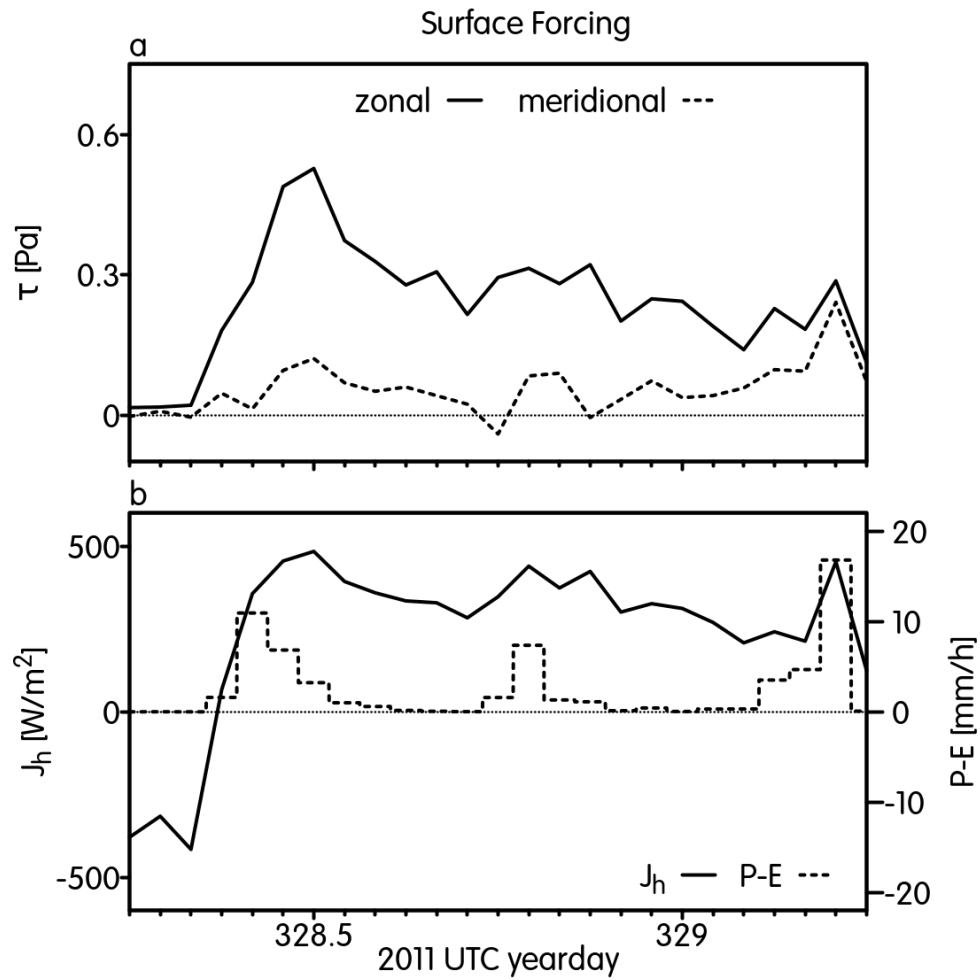


Figure 4.3: Surface fluxes used as upper boundary condition for LES: (a) zonal (solid) and meridional (dashed) momentum, (b) total surface heat flux (solid line, left axis) and fresh water flux (dashed line right axis)

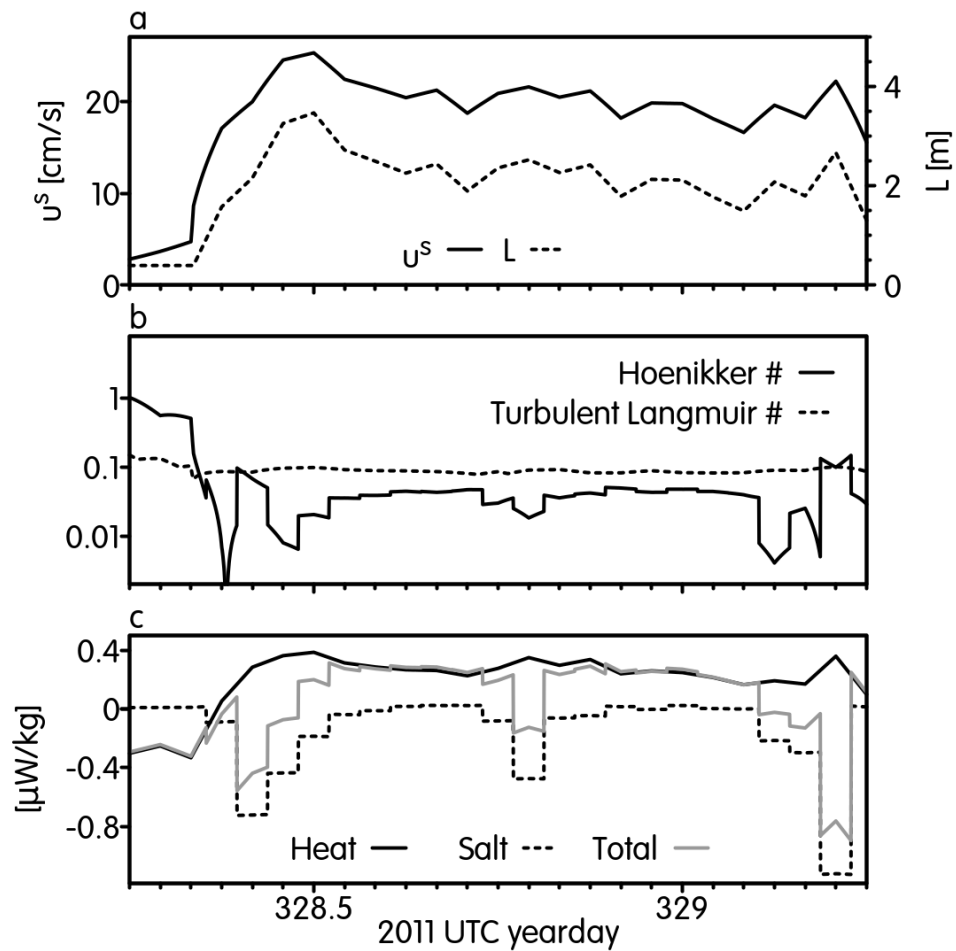


Figure 4.4: (a) Stokes drift u^s (solid, left axis) and Stokes e-folding length L (dashed, right axis). (b) Buoyancy fluxes due to surface heat (solid) and salt (dashed). (c) Hoenikker number (solid) and turbulent Langmuir number (dashed).

with coefficient $A_1 = 0.69$ with penetration depths $\lambda_1 = 1.1\text{m}$ and $\lambda_2 = 23\text{m}$.

Surface wave effects are parameterized as a function of \vec{U}_{wind} , the surface wind at 19.5m, by assuming an equilibrium sea state (Pierson and Moskowitz, 1964; Li and Garrett, 1993; Harcourt and D'Asaro, 2008). In this approximation, the Stokes drift velocity \vec{u}^s and the e-folding depth are given by:

$$\vec{u}^s = 0.0145 \vec{U}_{\text{wind}} e^{z/L} \quad (4.2)$$

$$L = 0.12 |\vec{U}_{\text{wind}}|^2 / g. \quad (4.3)$$

During the wind burst, the surface Stokes drift remained near 0.2ms^{-1} (figure 4.4a) while its vertical e-folding scale was 2-4 m). Both the turbulent Langmuir number $La_t = (u_S^2 \rho_0 / \tau)^{1/4}$ and the Hoenikker number $Ho = 4B_0 \rho_0 L / u_s \tau$ (where B_0 is the net surface buoyancy flux) were less than unity during the storm, indicating quantitatively that Langmuir turbulence is likely to have been a factor (Li and Garrett, 1995; McWilliams et al., 1997).

4.3 THE LES MODEL

The capabilities and limitations of upper ocean LES were established by S99, who simulated the ocean response to a westerly wind burst observed in the equatorial Pacific (Smyth et al., 1996a,b) and carried out statistical comparisons between the modeled turbulence and concurrent microstructure observations. Statistically, the turbulent kinetic energy dissipation rate, ϵ , was found to agree very well with the microstructure measurements under two conditions. First, a spin-up period of a few hours is required to produce realistic dissipation rates. Second, ϵ can be underestimated in strongly stratified layers where the model grid fails to resolve the Ozmidov scale. The resolution requirement for accurate turbulent fluxes is much less stringent since flux-carrying motions are resolved explicitly.

Our ocean LES model is essentially the same as that used by (S99)¹. The model equations include the surface waves by the inclusion of Stokes drift u_j^s , Coriolis effect, and buoyancy $b = -g \frac{\rho'}{\rho_0}$ due to variations in potential density $\rho' = \rho(T, S, P_{atm}) - \rho_0$ from temperature T , salinity S , and

¹ To estimate the e-folding depth of the Stokes drift, S99 used visual observations of the dominant swell instead of (3). Had (3) been used, the e-folding scale would have been smaller and the Langmuir turbulence would have been stronger and concentrated even more tightly at the surface. That would not have affected the conclusions.

atmospheric pressure P_{atm} using the equation of state from UNESCO (1981). The model does not include mixing due to surface wave breaking. The governing equations for velocity \vec{u} , temperature T , and salinity S are

$$\begin{aligned} \frac{\partial u_i}{\partial t} = & \quad \epsilon_{ijk} (u_j + u_j^s) (\epsilon_{klm} \nabla_l u_m + 2\Omega_k) \\ & - \nabla_i \left(p + \frac{1}{2} (u_j + u_j^s)^2 \right) + b\delta_{i3} \\ & + \alpha \nabla^{12} u_i + \nabla_j (\nu_t (\nabla_i u_j + \nabla_j u_i)) \end{aligned} \quad (4.4)$$

$$\nabla_j u_j = 0 \quad (4.5)$$

$$\frac{\partial T}{\partial t} = - (u_j + u_j^s) \nabla_j T + \nabla_j \text{Pr}^{-1} \nu_t \nabla_j T - \frac{1}{\rho c_p} \partial_z J \quad (4.6)$$

$$\frac{\partial S}{\partial t} = - (u_j + u_j^s) \nabla_j S + \nabla_j \text{Sc}^{-1} \nu_t \nabla_j S \quad (4.7)$$

where ϵ_{ijk} is the alternating tensor (not to be confused with the turbulent dissipation rate defined below), δ_{ij} is the identity tensor, $p = \frac{P}{\rho_0}$ is normalized pressure, Ω is planetary rotation, and ν_t is the eddy viscosity from the sub-grid scale model of the respective field. Profiles of the Stokes drift \vec{u}^s and radiative heat flux J are obtained from observations using (4.1–4.3).

The eddy viscosity ν_t is estimated using an anisotropic Smagorinsky closure (Ducros et al., 1996; Wilcox, 2006) detailed in the appendix. An additional hyper-viscosity term $\alpha \nabla^{12} u_i$ is included for numerical stability to remove variance at the grid-scale which is not absorbed by the Smagorinsky eddy viscosity. Both the turbulent Prandtl number Pr and Schmidt number Sc are assumed to be 0.6. The LES is conducted in a $256\text{m} \times 256\text{m} \times 60\text{m}$ horizontally periodic domain with 0.5m cubic cells. Equations (4.4–4.7) are advanced in time as in S99.

4.4 SIMULATION RESULTS

4.4.1 Spatial Organization of Turbulence

In our LES, subsurface turbulence develops immediately after the sharp increase in wind stress (figure 4.5). A few hours into the wind burst, the vertical velocity field shows considerable complexity, but at least two distinct, coherent flow geometries are evident (figure 4.5b). Near the surface, we see periodic bands of upwelling and downwelling. These are coherent over $50 - 150\text{m}$

and are spaced at 5 – 10m intervals. A range of orientations is visible, but the longest bands are oriented $\sim 20^\circ$ from the zonal, as expected for Langmuir cells (Leibovich, 1983; McWilliams et al., 1997; Thorpe, 2004). At the base of the surface mixed layer ($\sim 30\text{m}$ depth) are upwelling and downwelling bands oriented at $\sim 70^\circ$ north of zonal with wavelength 128m (half the domain extent). In this section we will diagnose the driving mechanisms of the modeled turbulence and quantify the resulting vertical fluxes. In the process, we will explain the patterns seen in figure 4.5.

4.4.2 Turbulent Kinetic Energy

As we are interested in turbulent mixing processes, the simplest metric is the mean turbulent kinetic energy tke (figure 4.5a). To derive the governing equation for $\langle tke \rangle_{x,y} = \langle \frac{1}{2} u'_i u'_i \rangle_{x,y}$, we decompose velocity u_i , pressure p , buoyancy b , and diffusivity ν_t into a horizontal mean $\langle \star \rangle_{x,y} \equiv \frac{1}{L_x L_y} \int_0^{L_x} \int_0^{L_y} \star \, dx dy$ and a perturbation $\star' = \star - \langle \star \rangle_{x,y}$. The momentum equation (4.4) is multiplied by u'_i and averaged over x and y , resulting in

$$\begin{aligned} \frac{\partial \langle tke \rangle_{x,y}}{\partial t} = & \overbrace{\begin{aligned} & - \langle w' u'_j \rangle_{x,y} \partial_z u_j^s \\ & - \langle w' u'_j \rangle_{x,y} \partial_z \langle u_j \rangle_{x,y} \\ & \langle w' b' \rangle_{x,y} - \langle \epsilon \rangle_{x,y} \end{aligned}}^{\text{generation/dissipation}} \\ & \overbrace{-\partial_z \langle w' tke + w' p' + sgs \rangle_{x,y}}^{\text{transport}} \\ & \overbrace{+\alpha \langle u_i \nabla^{12} u_i \rangle_{x,y}}^{\text{hyperviscosity}} \end{aligned} \quad (4.8)$$

where

$$\begin{aligned} \epsilon = & + \langle \nu_t \rangle_{x,y} \left\langle (\nabla_j u'_i) (\nabla_i u'_j) + (\nabla_j u'_i)^2 \right\rangle_{x,y} \\ & + \left\langle \nu'_t \left[(\nabla_j u'_i) (\nabla_i u'_j) + (\nabla_j u'_i)^2 \right] \right\rangle_{x,y} \\ & + \langle \nu'_t \nabla_i w' + \nu'_t \partial_z u'_i \rangle_{x,y} \partial_z \langle u_i \rangle_{x,y} \end{aligned} \quad (4.9)$$

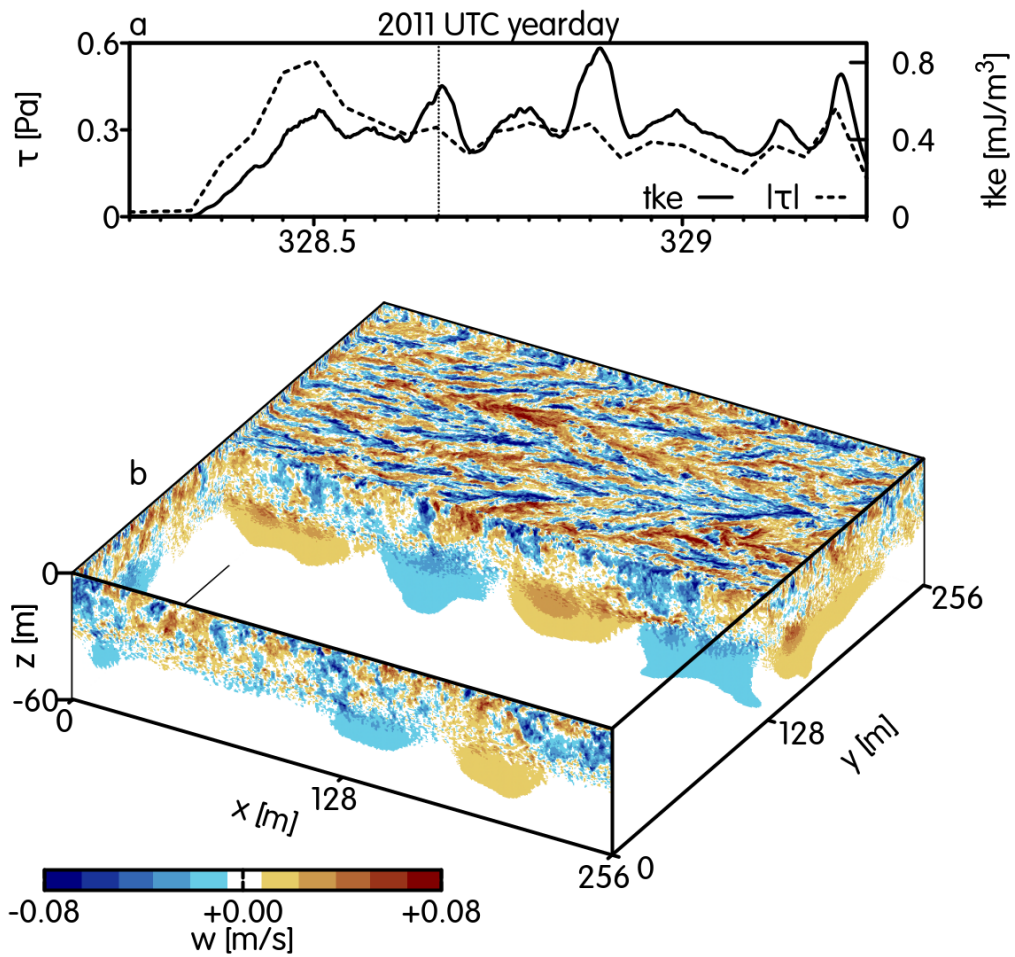


Figure 4.5: a) Surface stress $|\tau|$ and volume averaged turbulent kinetic energy tke . b) Snapshot of the vertical velocity $w(x, y, z)$ at day 328.67 shown by the dotted line on (a). The block of values $0\text{m} < y \leq 256\text{m}$ are rendered transparent for clarity. The upper surface shown is $z = -2\text{m}$.

is the viscous dissipation rate and

$$\begin{aligned}
sgs = & + \langle \nu_t \rangle_{x,y} \partial_z \left[\langle tke \rangle_{x,y} + \langle w'w' \rangle_{x,y} \right] \\
& - \langle \nu'_t (\partial_z tke + \nabla_i u'_i w') \rangle_{x,y} \\
& - \left[\langle \nu'_t u'_i \rangle_{x,y} \partial_z \langle u_i \rangle_{x,y} \right]
\end{aligned} \tag{4.10}$$

is the sub-grid-scale flux.

We distinguish between four generation/dissipation mechanisms and three transport mechanisms of turbulent kinetic energy. Surface waves interact with turbulent eddies through the shear of the Stokes drift. We refer to this process as Stokes production $StP = \partial_z u^s \langle u'w' \rangle_{x,y}$. Where Stokes production dominates, the turbulence is referred to as Langmuir turbulence (McWilliams et al., 1997). Similarly, the mean shear can exchange energy with turbulent eddies through the mechanism of shear production $SP = \partial_z \bar{u} \langle u'w' \rangle_{x,y}$. The conversion of potential energy to turbulent kinetic energy is quantified in the buoyancy production term $BP = \langle b'w' \rangle_{x,y}$. Eddy viscosity dissipates turbulent kinetic energy at the rate ϵ . The model distinguishes between resolved advection of turbulent kinetic energy $\langle w'tke \rangle_{x,y}$, pressure work $\langle w'p' \rangle_{x,y}$, and transport at sub-grid scales $\langle sgs \rangle_{x,y}$.

The sources and sinks are isolated by taking the vertical mean $\langle \star \rangle_z = \frac{1}{L_z} \int_{-L_z}^0 \star dz$ of equation 4.8

$$\begin{aligned}
\frac{d \langle tke \rangle_{x,y,z}}{dt} = & \overbrace{- \left\langle \langle u'_i w' \rangle_{x,y} \frac{\partial \langle u_i^s \rangle_{x,y}}{\partial z} \right\rangle_z}^{\text{Stokes}} \\
& \overbrace{- \left\langle \langle u'_i w' \rangle_{x,y} \frac{\partial \langle u_i \rangle_{x,y}}{\partial z} \right\rangle_z}^{\text{Shear}} \\
& \overbrace{+ \langle b'w' \rangle_{x,y,z}}^{\text{Buoyancy}} \quad \overbrace{- \langle \epsilon \rangle_{x,y,z}}^{\text{Dissipation}} \\
& \overbrace{+ \alpha \langle u_i \nabla^{12} u_i \rangle_{x,y,z}}^{\text{hyperviscosity}}.
\end{aligned} \tag{4.11}$$

In this vertically-averaged form, tke is generated by Stokes and shear production in roughly equal

proportion (figure 4.6b, red and dark blue curves), with the former dominating early in the wind burst and the latter dominating later. The vertically-averaged buoyancy production (figure 4.6b, light blue curve) was negative, fluctuating between 10% and 20% of the shear production. This is consistent with typical oceanic values of the flux Richardson number (Osborn, 1980). The hyperviscosity term is small, indicating that the Smagorinsky sub-grid model is effectively absorbing the downscale energy cascade.

As the simulation progresses, turbulence spreads downward; by the end of the 30 hour simulation turbulence has spread throughout the upper 40m. The evolution of tke features several maxima (figure 4.5a) originating at the surface and extending as deep as $\sim 30\text{m}$ (figure 4.6a). These coincide with extrema in all of the vertically integrated production terms (figure 4.6b). Close examination of figure 4.5a shows that these peaks correspond to wind maxima. The wind stress changes by $\sim 25\%$ from hour to hour (figure 4.3a, 4.5a) and these variations influence tke production through multiple routes. In the Li-Garrett parameterization (4.2,4.3), both the speed and the penetration depth of the Stokes drift increase with the wind and therefore so does the Stokes production term (figure 4.6b, dark blue and 4.7a). Wind also directly drives the mean shear and hence the shear production (figure 4.6b, red and 4.7b). The final tke maximum (day 329, hour 6) corresponded to a shift in the wind direction, with the result that the Stokes production acted to reduce tke , in competition with the positive shear production.

Langmuir turbulence is confined the upper 5m throughout the simulation (figure 4.7a). The fact that Langmuir turbulence appears so rapidly is due in part to the assumption that the waves are always in equilibrium with the wind (4.2, 4.3 ; Li and Garrett, 1993). In a more realistic model, the wave field, and the attendant Langmuir turbulence, might require more time to become established after the onset of strong winds. Some of this intense tke was advected downward and deposited at 3 – 12m depth (figure 4.8a). The reversal of StP near the end of the simulation (figure 4.6b) is also evident here.

The increased surface stress accelerated the near-surface current, so that the shear at its base (figure 4.9a) descended rapidly to about 20m depth, generating a layer of positive SP over the same layer (figure 4.7b). The strongest shear coincided with a sharp pycnocline (maximum of N^2 , figure 4.9b), which was due to a warm fresh surface layer (figure 4.2a and accompanying

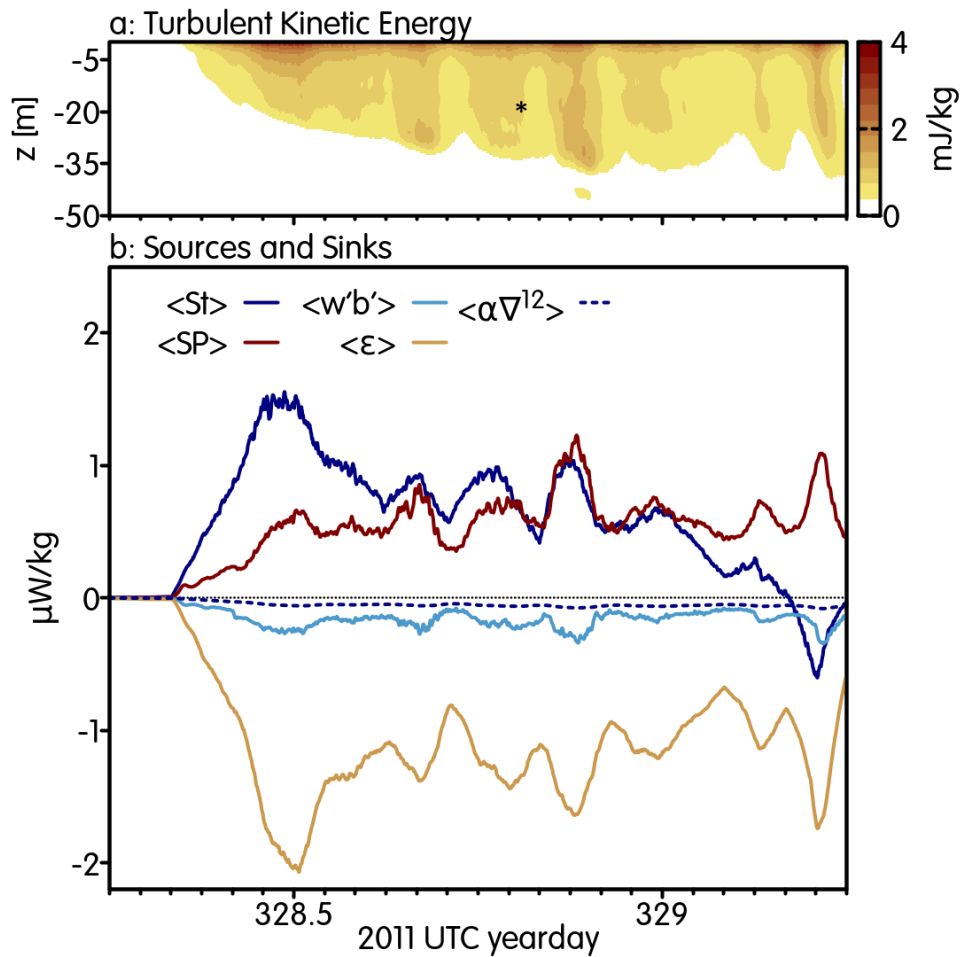


Figure 4.6: Turbulent kinetic energy and depth averaged sources and sinks. (a) Depth time profiles of turbulent kinetic energy. The asterisk indicates a particular rain event described in the text. (b) Sources of turbulent kinetic energy: Stokes drift $\langle St \rangle$ (blue solid), shear production $\langle SP \rangle$ (red), buoyancy production $\langle w'b' \rangle$ (cyan), dissipation $\langle \epsilon \rangle$ (yellow), hyper-viscosity $\langle \alpha \nabla^{12} \rangle$ (blue dashed).

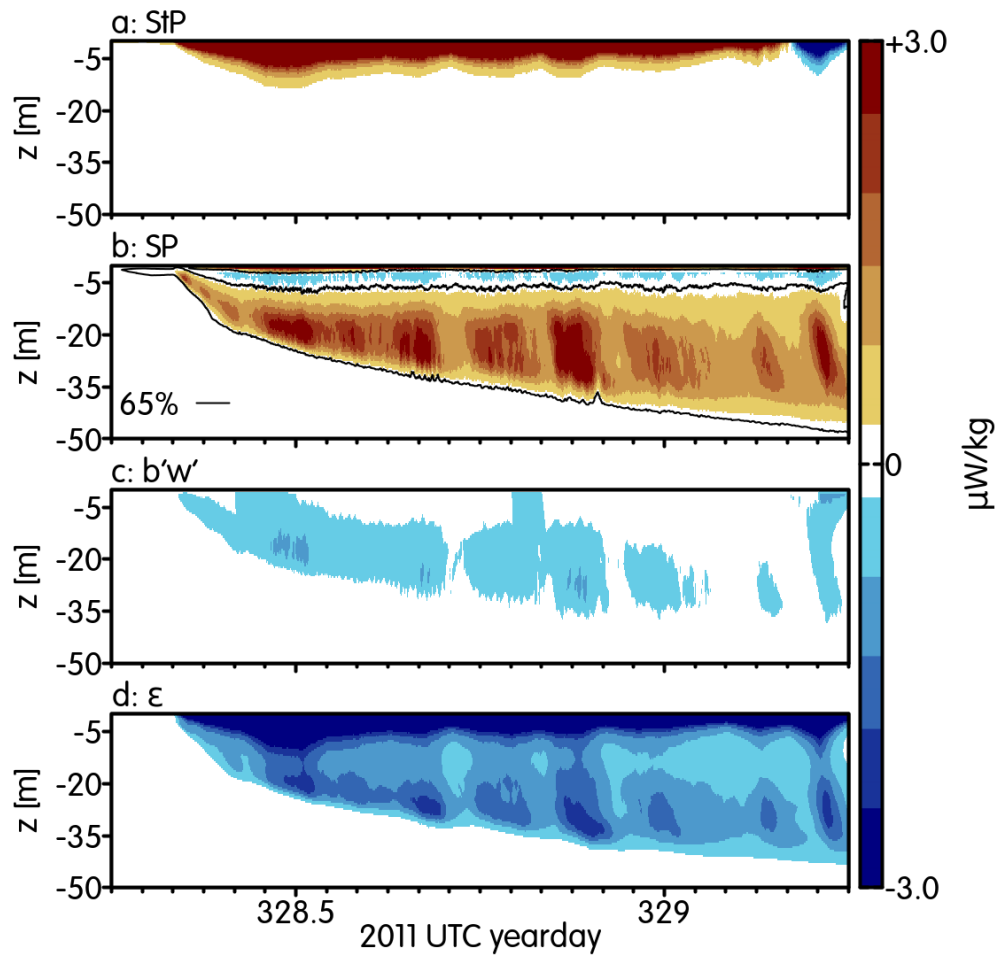


Figure 4.7: Sources and sinks of turbulent kinetic energy as functions of depth and time: (a) Stokes production $\langle \text{StP} \rangle$ with the upper 65th percentile outlined in black for later reference (see also figure 4.10), (b) shear production $\langle \text{SP} \rangle$, (c) buoyancy production $\langle w'b' \rangle$, and (d) dissipation $\langle \epsilon \rangle$.

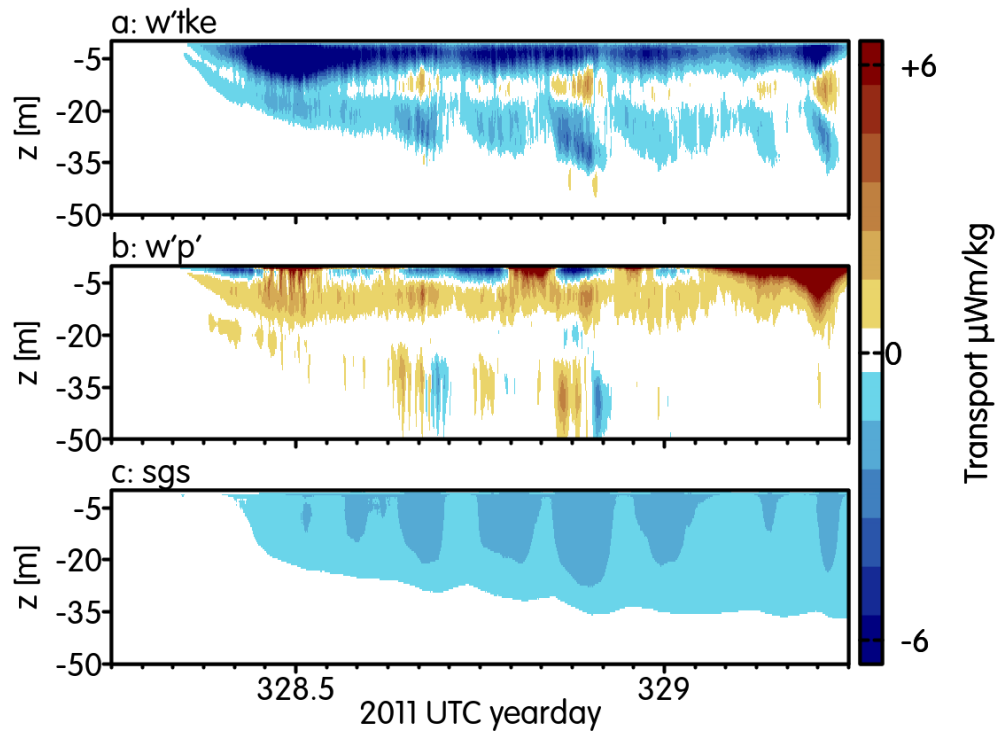


Figure 4.8: Turbulent kinetic energy and fluxes as functions of depth and time: (a) turbulent kinetic energy $\langle tke \rangle$, advection $\langle w'tke \rangle$, (b) pressure work $\langle p'w' \rangle$, and (c) transport by the sub grid-scale model.

discussion). Turbulence mixed the stable stratification, doing work against gravity and generating negative BP in the same layer (figure 4.7c). Dissipation ϵ is of comparable magnitude to generation throughout the simulation (figure 4.7d), and suggests turbulence rapidly adjusts to the relatively slowly changing driving fluxes and mean flow.

Turbulent kinetic energy is transported vertically via resolved advection, pressure work and sub-grid scale processes. Resolved advection of kinetic energy ($\langle w'tke \rangle$ figure 4.8a) serves to move *tke* downward from the strong production region at the surface and away from regions of shear production late in the simulation. The pressure work ($\langle w'p' \rangle$ figure 4.8b) is limited to the region of strong Stokes drift influence. It has variable direction. It is consistently upward below regions of strong Stokes production and becomes positive late in the simulation as the Stokes production changes sign. The sub-grid scale diffusive flux is small and generally diffuses *tke* downward (*sgs* figure 4.8c).

4.4.3 Marginal shear instability below the mixed layer

Below the Stokes penetration depth, turbulence is governed largely by a competition between shear and buoyancy. These influences are quantified here using the squared shear:

$$S^2 = \left(\frac{\partial}{\partial z} \langle u \rangle_{x,y} \right)^2 + \left(\frac{\partial}{\partial z} \langle v \rangle_{x,y} \right)^2 \quad (4.12)$$

and the squared buoyancy frequency

$$N^2 = -\frac{g}{\rho_0} \frac{\partial}{\partial z} \langle \rho \rangle_{x,y}. \quad (4.13)$$

The ability of turbulence to overcome gravity is consistent with the fact that the gradient Richardson number, $Ri = N^2/S^2$, was small in this layer. The transfer of kinetic energy from the mean shear to small eddies require that Ri be smaller than a critical value which is approximately 1/4 (Miles, 1961; Howard, 1961; Thorpe and Liu, 2009). That condition is satisfied in a layer surrounding 20m depth (figure 4.9c). At day 328.67, the time of the snapshot shown in figure 4.5, the shear magnitude S was maximum at 28m depth. At this depth, the direction of the shear vector was $\sim 20^\circ$. The large upwelling and downwelling bands evident in figure 4.5 are oriented

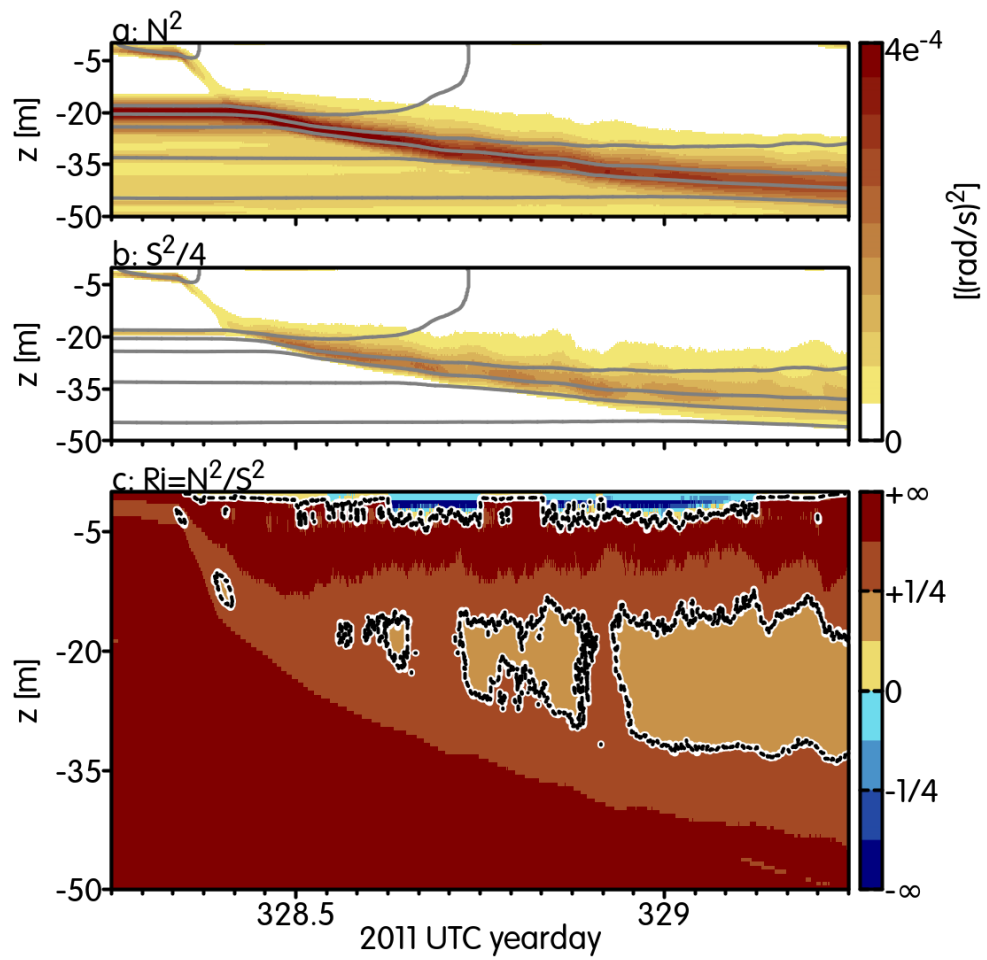


Figure 4.9: Isopycnals ($\Delta\rho = 100g/kg$) overlaid on (a) stratification N^2 and (b) shear squared divided by four $S^2/4$. (c) Mean Richardson number profiles, blue colors show unstable stratification, red colors are stable stratification with regions of dynamic instability outlined by the black and white contour.

perpendicular to the shear direction, just as one would expect for shear instability (Smyth et al., 2013). The mechanics of shear and buoyancy production are discussed further in section 4.44.4.3.

Marginal instability is a diagnostic property of sheared, stratified turbulence, and is readily identified by the statistics of the gradient Richardson number. Specifically, Ri fluctuates about a critical value (often approximated as $1/4$) due to competing effects of forcing and dissipation (e.g. Smyth and Moum, 2013). Based on Ri , the evolving upper ocean can be segregated into three distinct regimes (figure 4.9c).

1. During the strong solar heating and weak winds prior to the onset of the westerly wind burst the full water column is stable ($Ri > 1/4$, dark red regions of figure 4.9c).
2. At night, between precipitation events, the model develops convectively unstable stratification in the upper 5m ($Ri < 0$, blue regions on figure 4.9c)
3. As the surface current accelerates, the shear descends and accumulates at the base of the mixed layer. The increasing shear at the base of the mixed layer is evident by the region of dynamical instability ($Ri \lesssim 1/4$, yellow and orange regions of 4.9c) that thickens and descends following the onset of the wind burst .

Region (3) coincides with the largest values of the shear production term in the tke equation (figure 4.7b, and 4.10b). The proximity of the mean Ri to $1/4$ in that region indicates marginal instability.

We next examine the statistics of Ri conditioned on the shear production rate. Figure 4.10 shows the fraction of time-depth regions defined by specified ranges of SP and Ri . SP bins are chosen so that each bin contains 2.5% of the time-depth points, while Ri bins are logarithmically spaced. The fraction of time-depth points in each SP/ Ri bin is shown in figure 4.10b. The region of significant SP is conveniently defined to include the uppermost 35% of values, whose time-depth boundary is contoured in figure 4.7b. Ri abundance shows a marked shift in this region (figure 4.10). The cumulative fraction of the upper 35% of SP values (figure 4.10a, solid line) shows the Ri clustered near a central value slightly in excess of $1/4$. In regions of weak SP, the Ri distribution (figure 4.10a, dashed line) is broader and centered near unity, suggesting that shear instability is rare.

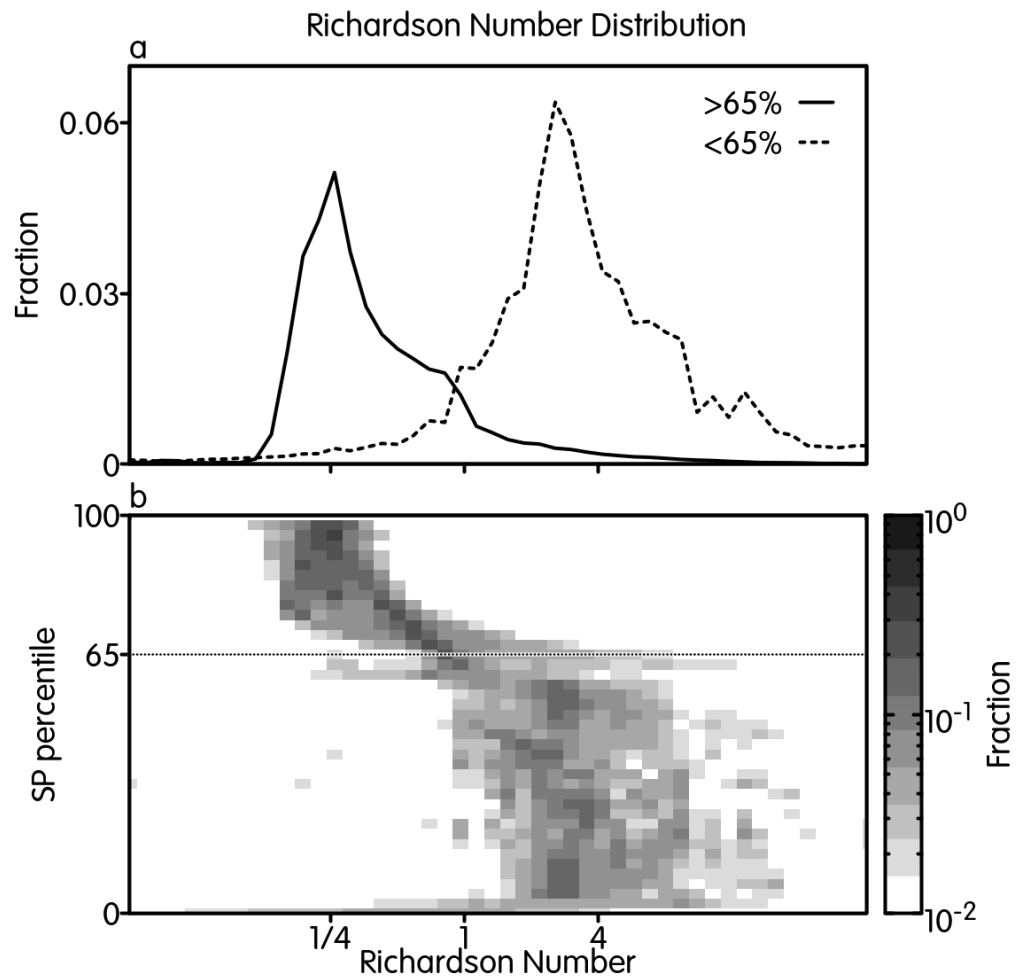


Figure 4.10: Distributions of Richardson number Ri : (a) fraction of time-depth points above (solid) and below (dashed) the 65th percentile of shear production as a function of Ri , (b) fraction of time depth points as a function of Ri and shear production percentile

These characteristics of the Ri distribution correspond well with observations of marginal instability associated with deep cycle turbulence in the equatorial Pacific, another example of forced-dissipative turbulence driven by the dynamic instability of sheared, stratified flow (Smyth and Moum, 2013).

4.4.4 Turbulent Fluxes

We focus on vertical fluxes across three particular surfaces. The first is the air-sea interface, $z = 0$, where fluxes were inferred from the DYNAMO observations. The other two are alternative definitions of the lower boundary of what we casually call the “mixed layer” in our model. Both are defined using the density difference $\Delta\rho$ between the depth of interest and the surface. The first choice is $\Delta\rho = 0.01\text{kg m}^{-3}$ (Moum et al., 2014). Above this depth, vertical fluid motion is essentially unhindered by buoyancy, so that the layer’s temperature is nearly the SST. For clarity, we will refer to this layer as the surface layer (SL); it is equivalent the “diurnal mixed layer” employed, for example, by Smyth et al. (1996a,b, 2013). We will also consider the choice $\Delta\rho = 0.1\text{kg/m}^3$. This depth is relatively stable, and is in particular resistant to rapid shoaling during rain events. It has been used recently to explore the subsurface heat budget during DYNAMO (Chi et al., 2014). We refer to the corresponding layer $\Delta\rho < 0.1\text{kg/m}^3$ as the “mixed layer” (ML).

Prior to the wind burst, the turbulent heat flux is negative as sun-warmed surface water is mixed downward (figure 4.11). With the onset of strong winds, the heat flux adjacent to the surface changes from negative to positive, indicating a downward flux of surface water cooled, mainly, by the latent heat release due to wind-enhanced evaporation. After wind onset, a region of strong downward heat flux forms at the surface and descends rapidly to $\sim 15\text{m}$ depth, then gradually to $\sim 35\text{m}$. This coincides with the ML base and also with region 3, identified in the previous subsection, in which shear instability is active. The resulting turbulence transports cool water from the thermocline upward, exchanging it with water warmed at the surface prior to the wind burst. At the base of the SL, the modeled turbulent flux is approximately 1/3–1/2 of the surface flux (figure 4.11b, solid curves). This ratio is consistent with the observational estimate by Moum et al. (2014). At the base of the ML, the modeled heat flux is usually slightly larger, with values fluctuating in the range $-300 \pm 100\text{W/m}^2$. For comparison, in the observational analyses of Chi et al. (2014), a smoothed estimate of this flux (based on a budget residual) decreased from

zero to around -300W/m^2 over several days after the beginning of the storm (figure 4.12).

Like the heat flux, the salt flux shows a maximum near the ML base (see below). The flux is positive (i.e. upward), since salty deep water is mixed with fresh surface water. Near surface flux events correspond to rain. The SL and ML bases bracket the salt flux maximum, so that values across those surfaces are nearly equal. On average the salt flux in that layer is slightly higher than the surface value, suggesting that some salt is being mixed up from below, most likely from the barrier layer around 20m depth (figure 4.2a, dashed curve) consistent with observations (Moum et al., 2014).

Sporadic rain events associated with the MJO active phase replenish the saline stratification that existed prior to the wind burst. The renewed fresh layer causes the SL base to shoal as a stratified fresh layer at the surface is formed (e.g. asterisk on figures 4.6 and 4.12). The fresh layer insulates the underlying water from the surface momentum flux, leading to a rapid decrease of turbulence around 20m depth in figure 4.6 near the initial halocline. Smyth et al. (1997) have described several similar events observed during COARE. The fresh layer persists until near-surface turbulence is able to re-entrain the fluid that had been part of the mixed layer before the downpour, leading to a resumption of turbulence around 20m depth.

The model resolution is chosen so that the resolved turbulent momentum flux dominates the momentum budget (i.e. the sub-grid scale fluxes are relatively small). As the wind event begins, an area of strong momentum flux forms near the surface driven by Stokes production (figure 4.7a) and accelerates the upper 10 – 20m (figure 4.13). A large fraction of the momentum is deposited near the ML base (Kukulka et al., 2010). During these events, the resulting shear is the cause of the low Richardson number and high shear production in this region (section 4.44.4.3), and also of the intense heat and salt fluxes discussed above.

There is little lag between the surface stress and the momentum flux through the mixed layer. Below the ML base, the turbulent momentum flux lags the surface stress, as illustrated by the curved plumes of intense momentum flux in figure 4.13. While the present LES covers only the first 24 hours of the wind burst, observations suggest that this deep turbulence remains active long after the wind subsides, potentially impacting the subsequent switch to the suppressed phase of the MJO (Moum et al., 2014).

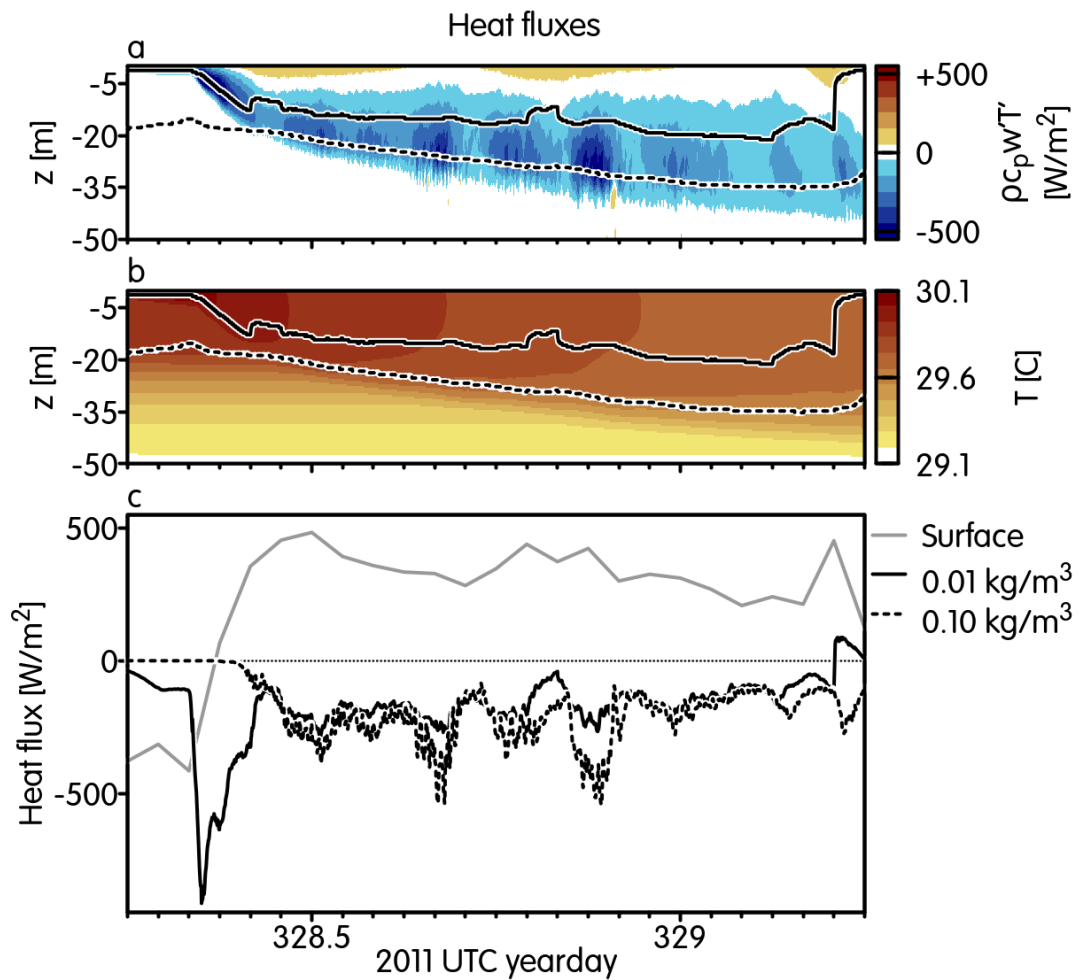


Figure 4.11: Mixed layer depths ($\Delta\sigma = 0.01, 0.10$ kg/m³) are plotted with: (a) Resolved heat flux $\langle w'T' \rangle$ as a function of depth and time. (b) Mean temperature. (c) Surface heat flux (grey) and heat flux at the, surface layer (black) and mixed layer (dashed) depths.

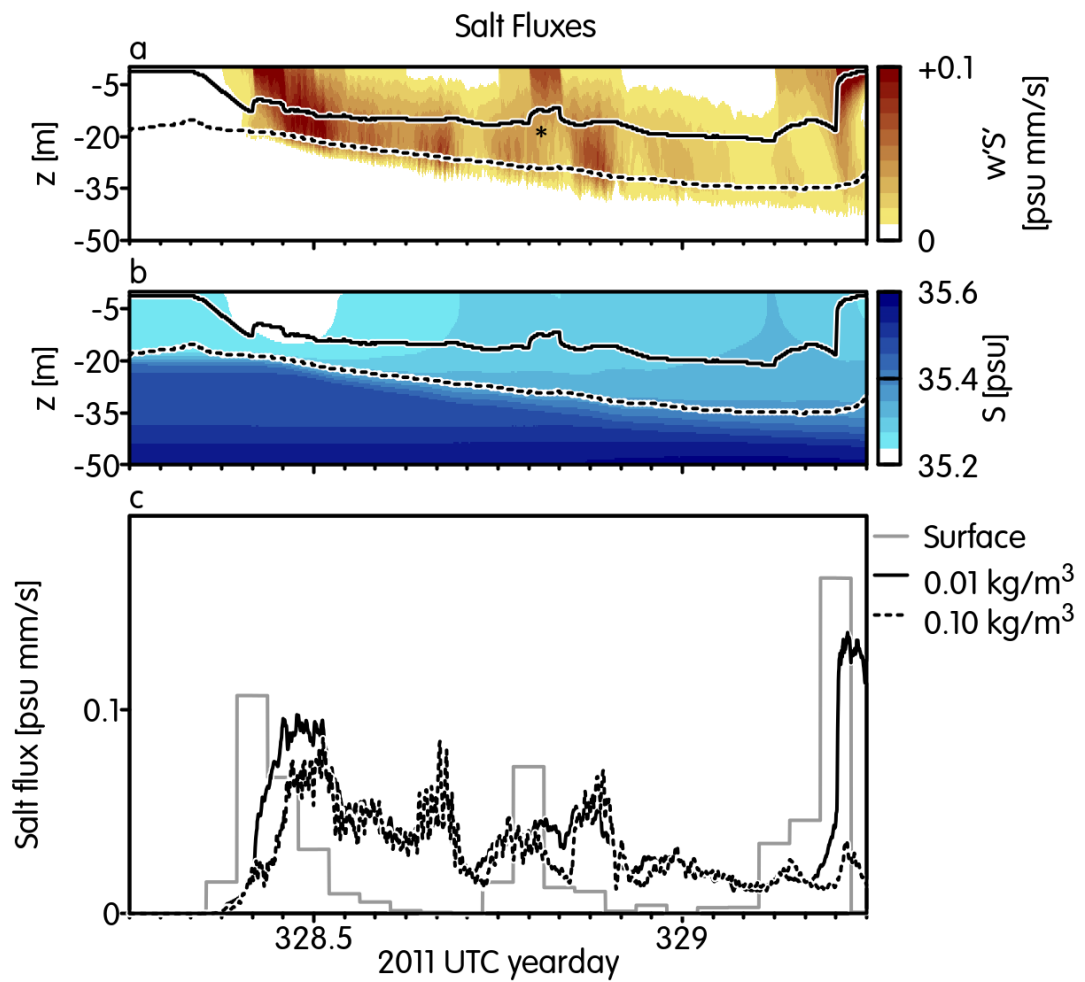


Figure 4.12: Mixed layer depths ($\Delta\sigma = 0.01, 0.10 \text{ kg/m}^3$) are plotted with: (a) Resolved salt flux $\langle w'S' \rangle$ as a function of depth and time. The asterisk indicates a particular rain event described in the text. (b) Mean salinity. (c) Surface salinity flux (grey) and salinity flux at the, surface layer (black) and mixed layer (dashed) depths.

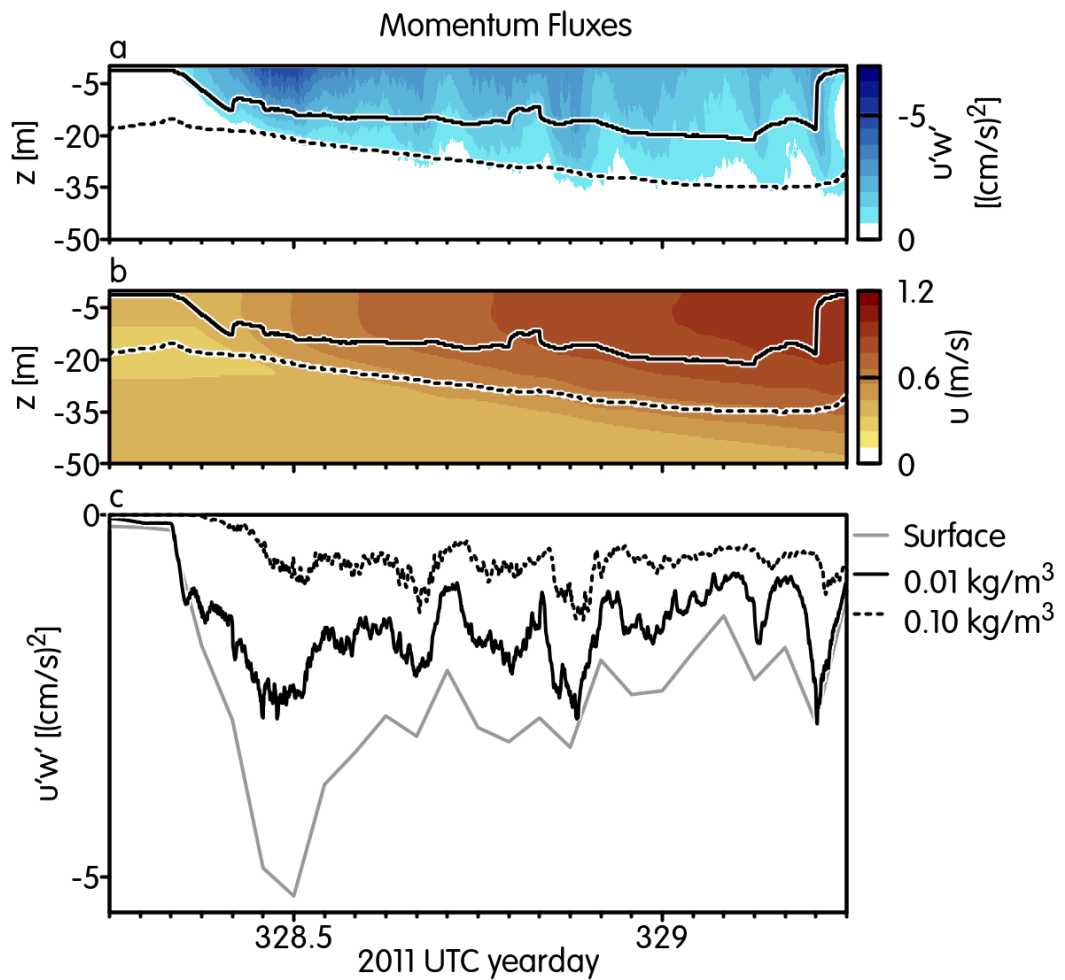


Figure 4.13: Mixed layer depths ($\Delta\sigma = 0.01, 0.10 \text{ kg/m}^3$) are plotted with: (a) Resolved momentum flux $\langle u'w' \rangle$ as a function of depth and time (b) Mean zonal velocity. (c) Surface momentum flux (grey) and momentum flux at the, surface layer (black) and mixed layer (dashed) depths.

4.5 COMPARISON WITH THE COARE WIND BURST

Direct measurements of turbulence during WWB are rare due to the technical difficulty of making small-scale measurements in heavy weather. Such observations have been made once previously, in the western Pacific warm pool as part of COARE. Here, we will compare the two cases. The COARE wind burst lasted about 3 days, as in the present case, S99 extended those observations using LES modeling the second day. The observation site was slightly south of the equator (2S), but was close enough that the inertial period was long compared with the duration of the WWB, so that Coriolis effects were negligible over the modeled interval. During that time, the wind was mostly westerly (veering to northwesterly during the last few hours) with magnitude around 0.15Nm^{-2} . Because wind stress was significant prior to the modeling period, the initial surface mixed layer was about 50m deep.

In comparison, the DYNAMO wind burst was brief and intense, lasting only 24 hours, with wind stress rising from zero to 0.6Nm^{-2} . The wind burst followed a lengthy calm period associated with the MJO suppressed phase (Moum et al., 2014), with the result that the upper ocean was well stratified and the surface mixed layer was only a few meters deep.

Both the COARE and DYNAMO simulations lasted ~ 24 hours. In each case, the net surface heat flux changed from a daytime value around -400Wm^{-2} to a night time value $+400\text{Wm}^{-2}$, turbulent kinetic energy production in the upper few meters was dominated by Stokes production (figure 4.7a, S99 figure 7a), and shear production was strong at the mixed layer base as it descended in late afternoon and early evening before relaxing to a quasi-stationary state. There was an order of magnitude difference in the quasi-equilibrium value of shear production: 10^{-7}W/kg in COARE versus 10^{-6}W/kg in DYNAMO. This difference is consistent with the combination of stronger winds and shallower mixed layer in DYNAMO.

In COARE, buoyancy production was significantly positive down to 30-40 m depth (S99 figure 7c), whereas in DYNAMO the convectively unstable layer was restricted to the upper 2-3 m (figure 4.9). This is consistent with the difference in Hoenikker number: $Ho \sim 1$ for COARE and $Ho \sim 0.1$ for DYNAMO. At the mixed layer base, in both cases, buoyancy production was smaller than shear production, typically by a factor consistent with a flux Richardson number in the usual range 0.2-0.3. Like shear production, the turbulent kinetic energy dissipation rate at the base of

the nocturnal mixed layer was an order of magnitude larger in DYNAMO (10^{-6}W/kg) than in COARE (10^{-7}W/kg). As in COARE, the DYNAMO modeled dissipation rates were consistent with observations, typically to within a factor two. A fraction of the turbulence observed in DYNAMO was biogenic, and therefore has no counterpart in the LES (Pujiana et al., 2015). At the mixed layer base that fraction was a few tens of percent at most, and it therefore does not alter the approximate agreement noted here.

The turbulent heat flux at the mixed layer base defined by $\Delta\sigma = 0.01\text{kg/m}^3$ reached maximum values around 60Wm^{-2} in COARE (S99, figure 18d). In DYNAMO, the heat flux at the mixed layer base was generally larger (figure 4.11).

4.6 CONCLUSIONS AND DISCUSSION

We conduct LES of the upper ocean response to a westerly wind burst that occurred in the equatorial Indian ocean in boreal fall, 2011 as part of an active MJO phase. During the long period of relative calm and strong solar heating preceding the wind burst, a layer of strong stable stratification was established at the base of a shallow surface mixed layer. In the simulation, the upper ocean reacts to the strong surface forcing with enhanced turbulent kinetic energy production and expansion of the mixed layer. Parameterized Stokes drift forcing responded instantaneously (by construction) to the rapid change in wind stress. The resulting Langmuir turbulence mixed a layer extending to $\gtrsim 5\text{m}$. Within this layer the vertical kinetic energy was consistent with the surface layer Langmuir number (La_{SL}) scaling of Harcourt and D’Asaro (2008) with an observed range of $\text{La}_{\text{SL}} = 1 - 2.5$.

Subsequently the wind-driven mixed layer deepens by entrainment to about 30m. Turbulence at and below the mixed layer base is consistent with generation by shear instability. Convective turbulence is not a factor. Instead, the Langmuir and shear-driven turbulence generate potential energy at a rate consistent with a flux Richardson number of 0.1-0.2 typical of ocean mixing (Osborn, 1980; Moum, 1996). The near surface is dominated by Stokes production while shear production dominates turbulent kinetic energy production near the mixed layer base (figure 4.7). Mixed layer depth (figures 4.11, 4.12, 4.13) is initially comparable to the penetration depth of the Stokes drift (figure 4.3) due to stratification prior to the MJO active phase (figure 4.2). During

the wind burst, surface buoyancy and momentum fluxes (figure 4.3) are quickly communicated into the mixed layer by Langmuir turbulence before shear or convective instabilities can grow as expected due to the low Hoenikker and turbulent Langmuir numbers (figure 4.4, 4.11, 4.12, 4.13). As the mixed layer extends beyond the Stokes penetration depth, mixing shifts into a region where shear dominates production of turbulent kinetic energy.

In the simulation, the heat flux across the mixed layer base is about half as strong as the sum of latent, radiative and sensible fluxes at the surface. The resulting drop of $\sim 0.5\text{C}^\circ$ in sea surface temperature, which tends to quench atmospheric convection, was therefore controlled in substantial measure by subsurface processes. Observations show a similar drop in SST (Chi et al., 2014; Moum et al., 2014). The large downward heat flux occurs despite of a pre-existing saline barrier layer at the top of the thermocline (Chi et al., 2014; Moum et al., 2014). This suggests that processes transporting heat through the mixed layer base should be accounted for in order to capture MJO physics in large-scale models.

Relative to the COARE wind burst previously observed in the Pacific (S99), the DYNAMO event involved a brief, intense forcing applied to a previously stable upper ocean. The result was relatively strong turbulence concentrated in a shallow layer in which shear from Stokes drift and the mean flow dominated over the convection that was important in the COARE observation.

The significant contribution of surface waves to the surface turbulent kinetic energy budget highlights the need for accurate characterization of the wave state. Careful attempts to model the influence of wave breaking (e.g. Sullivan et al., 2007) could further improve the fidelity of the model. Direct measurements of the sea surface height in were made as part of the DYNAMO campaign (Moum et al., 2014) and may be used in place of (4.2,4.3) for future studies of near-surface mixing.

5 CONCLUSIONS

These three projects now color how I look at vertical transport in the ocean. Despite the idealized geometry and narrow focus of chapters 2 and 3 they highlight how strongly the evolution of flow fields depends on a narrow range of parameters. This strong dependence is echoed in the contrast between convection in the COARE simulation (Skylingstad et al., 1999) with the wave driven surface layer during the westerly wind burst in DYNAMO (chapter 4). The primary focus of all three questions is to quantify the flows influence on large scale changes in biophysical conditions.

5.1 BIOLOGICAL CONVERGENCE

The importance of an organisms motility and response to the flow stands out in the peak aggregation rate (2.22). The relative importance of physical and biological components is alluded to in by the strong dependence on relative motility V_b but this single parameter is an oversimplification of the dynamics. The divergence-less flow is unable to spontaneously generate gradients. The organisms swimming orientation is free to converge or diverge as is rotates (2.8). These two simple systems when coupled lead to strong aggregation (figure 2.10) because of an additional freedom in the biological fluxes that is not present in the flow field.

In the system described in chapter 2 organisms are reduced to a simple automata whose behavior is a function of the flow field (2.17). The gyrotactic model implicitly limits the size of the organisms for which it is applicable (appendix A.3). Despite these strong restrictions on size and motility it is the biological motion that changes the concentration.

The simplicity of the biological model (2.17) is contrasted with the sophisticated fluid model (appendix A.1) which resolves the full scale of fluid motion. The complex flow geometry is always constrained by incompressibility and can only amplify gradients. In light of the strong assumptions in idealizing the organism it is difficult to generalize the results quantitatively. Given the primacy of the biological parameters in this simple biological system it is reasonable to postulate that in organisms that exhibit swimming behavior aggregation is more strongly dependent on that behavior than the nature of the flow field in which they are embedded.

5.2 INSTABILITY AND TURBULENCE

Chapter 2 focused on simulating organisms transit through overturning K-H billows to test if the vortices would allow for the Stommel (1949) trapping mechanism. Ensuring overturns required an exploration of Re_0 Ri_0 space. The analysis of a idealized shear layer in chapter 3 was performed after chapter 2 with the hope that it would allow for more efficient usage of computer time.

The simulations in chapter 2 were at low Reynolds numbers due to computational constraints. As is common in computational fluid dynamics simulation results are extrapolated to oceanic Re_0 regimes. The mean flow decay estimated in chapter 3 enforces an upper limit for the accessible range of dynamically interesting Ri_0 of these simulations.

A method to alleviate the decay is to add a momentum flux at the upper and lower domain boundaries. By adding an energy source to the DNS boundaries a steady state can emerge. This approach allows for much smaller initial perturbations and does not require an a priori choice of wave number tuned to the instability. Steady state mixing statistics can be calculated and compared with the active shear production at the mixed layer base like those in figure 4.10 to better explore the dynamics marginal instability. The introduction of a significant momentum flux at the upper boundary of a shear layer is reminiscent of the dynamic exchange between the Langmuir cell driven upper layer and shear driven layer observed in 4.7.

BIBLIOGRAPHY

- Alford, M. H., 2003: Improved global maps and 54-year history of wind-work on ocean inertial motions. *Journal of Geophysical Research*, **30** (8), 1424, doi:10.1029/2002GL016614.
- Asai, T., 1970: Stability of a plane parallel flow with variable vertical shear and unstable stratification. *Journal of the Meteorological Society of Japan*, **48**, 129–139.
- Batchelor, G. K., 1969: Computation of the energy spectrum in homogeneous twodimensional turbulence. *Physics of Fluids*, **12** (12), II-233–II-239, doi:http://dx.doi.org/10.1063/1.1692443, URL http://scitation.aip.org/content/aip/journal/pof1/12/12/10.1063/1.1692443.
- Battjes, J. A., 1988: Surf-zone dynamics. *Annu. Rev. Fluid Mech.*, **20** (1), 257–291, doi:10.1146/annurev.fl.20.010188.001353, URL http://dx.doi.org/10.1146/annurev.fl.20.010188.001353.
- Benoit-Bird, K. J., T. J. Cowles, and C. E. Wingard, 2009: Edge gradients provide evidence of ecological interactions in planktonic thin layers. *Limnology and Oceanography*, **54** (4), 1382–1392.
- Bevington, P., and D. Robinson, 1969: *Data reduction and error analysis for the physical sciences*, Vol. 336. McGraw-Hill New York.
- Birch, D. A., W. R. Young, and P. J. S. Young, 2008: Thin layers of plankton: formation by shear and diffusion. *Deep Sea Research Part I*, **55** (3), 277–295, doi:10.1016/j.dsr.2007.11.009.
- Birol, A. K., P. A. Rochford, and H. E. Hurlburt, 2000: An optimal definition for ocean mixed layer depth. *Journal of Geophysical Research: Oceans*, **105** (C7), 16 803–16 821, doi:10.1029/2000JC900072.
- Boffetta, G., and R. E. Ecke, 2011: Two-dimensional turbulence. *Annu. Rev. Fluid Mech.*, **44** (1), 427–451, doi:10.1146/annurev-fluid-120710-101240, URL http://dx.doi.org/10.1146/annurev-fluid-120710-101240.
- Brainerd, K. E., and M. C. Gregg, 1995: Surface mixed and mixing layer depths. *Deep Sea Research Part I: Oceanographic Research Papers*, **42** (9), 1521–1543, URL http://www.sciencedirect.com/science/article/pii/096706379500068H.
- Brucker, K. A., and S. Sarkar, 2007: Evolution of an initially turbulent stratified shear layer. *Physics of Fluids*, **19** (10), 105 105, doi:10.1063/1.2756581.
- Burden, R. L., and J. D. Faires, 2004: *Numerical Analysis*. 8th ed., Brooks Cole.
- Carpenter, J. R., E. W. Tedford, E. Heifetz, and G. A. Lawrence, 2013: Instability in stratified shear flow: Review of a physical interpretation based on interacting waves. *Appl. Mech. Rev.*, **64** (6), 060 801–060 801–17, doi:10.1115/1.4007909.
- Caulfield, C., and W. Peltier, 1994: Three dimensionalization of the stratified mixing layer. *Physics of Fluids*, **6**, 3803–3805.
- Caulfield, C., and W. Peltier, 2000: The anatomy of the mixing transition in homogeneous and stratified free shear layers. *Journal of Fluid Mechanics*, **413**, 1–47.
- Chang, C.-P., 1977: Viscous internal gravity waves and low-frequency oscillations in the tropics. *J. Atmos. Sci.*, **34** (6), 901–910, doi:10.1175/1520-0469(1977)034<0901:VIGWAL>2.0.CO;2.

- Chen, G., B. Chapron, R. Ezraty, and D. Vandemark, 2002: A global view of swell and wind sea climate in the ocean by satellite altimeter and scatterometer. *J. Atmos. Oceanic Technol.*, **19** (11), 1849–1859, doi:10.1175/1520-0426(2002)019<1849:AGVOSA>2.0.CO;2.
- Cheriton, O. M., M. A. McManus, D. Van Holiday, C. F. Greenclaw, P. L. Donaghay, and T. J. Cowles, 2007: Effects of mesoscale physical processes on thin zooplankton layers at four sites along the west coast of the U.S. *Estuaries and Coasts*, **30** (4), 575–590.
- Chi, N.-H., R.-C. Lien, E. A. D’Asaro, and B. B. Ma, 2014: The surface mixed layer heat budget from mooring observations in the central Indian ocean during Madden–Julian oscillation events. *Journal of Geophysical Research: Oceans*, **119** (7), 4638–4652, doi:10.1002/2014JC010192.
- Childress, S., M. Levandowsky, and E. A. Spiegel, 1975: Pattern formation in a suspension of swimming microorganisms: equations and stability theory. *Journal of Fluid Mechanics*, **69** (03), 591–613, doi:10.1017/S0022112075001577.
- Churnside, J. H., and P. L. Donaghay, 2009: Thin scattering layers observed by airborne lidar. *ICES Journal of Marine Science*, **66** (4), 778–789.
- Clever, R., and F. Busse, 1992: Three-dimensional convection in a horizontal fluid layer subjected to a constant shear. *Journal of Fluid Mechanics*, **234** (1), 511–527.
- Corcos, G. M., and F. S. Sherman, 1976: Vorticity concentration and the dynamics of free shear layers. *Journal of Fluid Mechanics*, **73** (2), 241.
- Corcos, G. M., and F. S. Sherman, 1984: The mixing layer: deterministic models of a turbulent flow. part 1. introduction and the two-dimensional flow. *Journal of Fluid Mechanics*, **139**, 29–65, doi:10.1017/S0022112084000252.
- Cox, S., 1996: The onset of thermal convection between poorly conducting horizontal boundaries in the presence of a shear flow. *SIAM Journal on Applied Mathematics*, **56** (5), 1317–1328.
- Cronin, M. F., and M. J. McPhaden, 2002: Barrier layer formation during westerly wind bursts. *J. Geophys. Res.*, **107** (C12), 8020–, URL <http://dx.doi.org/10.1029/2001JC001171>.
- Crowe, C. T., T. R. Troutt, and J. N. Chang, 1996: Numerical models for two-phase turbulent flows. *Annual Review of Fluid Mechanics*, **28**, 11–43.
- Dale, A. C., J. A. Barth, M. D. Levine, and J. A. Austin, 2008: Observations of mixed layer restratification by onshore surface transport following wind reversal in a coastal upwelling region. *Journal of Geophysical Research*, **113** (C01010), doi:10.1029/2007JC004128.
- de Szoeke, S. P., J. B. Edson, J. R. Marion, C. W. Fairall, and L. Bariteau, 2015: The MJO and air-sea interaction in TOGA COARE and DYNAMO. *J. Climate*, **28**, 597–622, doi:10.1175/JCLI-D-14-00477.1.
- Deardorff, J. W., 1972: Numerical investigation of neutral and unstable planetary boundary layers. *Journal of the Atmospheric Sciences*, **29** (1), 91–115.
- Deksheniaks, M., P. Donaghay, J. Sullivan, J. Rines, T. Osborn, and M. Twardowski, 2001: Temporal and spatial occurrence of thin phytoplankton layers in relation to physical processes. *Marine Ecology Progress Series*, **223**, 61–71.

- Domaradzki, J. A., and R. W. Metcalfe, 1988: Direct numerical simulations of the effects of shear on turbulent Rayleigh- benard convection. *Journal of Fluid Mechanics*, **193**, 499–531.
- Drazin, P. G., 2002: *Introduction to Hydrodynamic Instability*. Cambridge texts in applied mathematics, Cambridge Univ. Press, 40 West 20th Street, New York, NY 10011-4211 USA.
- Ducros, F., P. Comte, and M. Lesieur, 1996: Large-eddy simulation of transition to turbulence in a boundary layer developing spatially over a flat plate. *Journal of Fluid Mechanics*, **326**, 1–36, doi:10.1017/S0022112096008221.
- Durham, W. M., E. Climent, and R. Stocker, 2011: Gyrotaxis in a steady vortical flow. *Physical Review Letters*, **106** (23), 238 102, doi:10.1103/PhysRevLett.106.238102.
- Durham, W. M., J. O. Kessler, and R. Stocker, 2009: Disruption of vertical motility by shear triggers formation of thin phytoplankton layers. *Science*, **323**, 1067–1070, doi:10.1126/science.1167334.
- Egbert, G. D., A. F. Bennett, and M. G. G. Foreman, 1994: Topex/poseidon tides estimated using a global inverse model. *J. Geophys. Res.*, **99** (C12), 24 821–24 852, URL <http://dx.doi.org/10.1029/94JC01894>.
- Emanuel, K. A., 1987: An air-sea interaction model of intraseasonal oscillations in the tropics. *J. Atmos. Sci.*, **44** (16), 2324–2340, doi:10.1175/1520-0469(1987)044<2324:AASIMO>2.0.CO;2.
- Ferrari, R., and C. Wunsch, 2008: Ocean circulation kinetic energy: Reservoirs, sources, and sinks. *Annu. Rev. Fluid Mech.*, **41** (1), 253–282, doi:10.1146/annurev.fluid.40.111406.102139.
- Fjørtoft, R., 1953: On the changes in the spectral distribution of kinetic energy for twodimensional, nondivergent flow. *Tellus A*, **5** (3).
- Franks, P. J. S., 1995: Thin layers of phytoplankton: a model of formation by near-inertial wave shear. *Deep Sea Research Part I: Oceanographic Research Papers*, **42** (1), 75–83, doi:DOI:10.1016/0967-0637(94)00028-Q.
- Frigo, M., and S. G. Johnson, 2005: The design and implementation of FFTw3. *Proceedings of the IEEE*, **93** (2), 216–231.
- Fung, J. C. H., 2000: Residence time of inertial particles in a vortex. *Journal of Geophysical Research*, **105** (C6), 14 261–14 272.
- Geyer, W. R., A. C. Lavery, M. E. Scully, and J. H. Trowbridge, 2010: Mixing by shear instability at high reynolds number. *Geophys. Res. Lett.*, **37** (22), n/a–n/a, URL <http://dx.doi.org/10.1029/2010GL045272>.
- Geyer, W. R., and J. D. Smith, 1987: Shear instability in a highly stratified estuary. *Journal of Physical Oceanography*, **17** (10), 1668–1679, doi:10.1175/1520-0485(1987)017<1668:SIIAHS>2.0.CO;2.
- Grant, A. L. M., and S. E. Belcher, 2009: Characteristics of Langmuir turbulence in the ocean mixed layer. *J. Phys. Oceanogr.*, **39** (8), 1871–1887, doi:10.1175/2009JPO4119.1, URL <http://dx.doi.org/10.1175/2009JPO4119.1>.
- Harcourt, R. R., and E. A. D’Asaro, 2008: Large-eddy simulation of Langmuir turbulence in pure wind seas. *J. Phys. Oceanogr.*, **38** (7), 1542–1562, doi:10.1175/2007JPO3842.1.

- Hazel, P., 1972: Numerical studies of the stability of inviscid stratified shear flows. *Journal of Fluid Mechanics*, **51** (01), 39–61, doi:10.1017/S0022112072001065.
- Hendon, H. H., and J. Glick, 1997: Intraseasonal air-sea interaction in the tropical Indian and Pacific oceans. *Journal of climate*, **10** (4), 647–661.
- Hopkins, M. M., and L. J. Fauci, 2002: A computational model of the collective fluid dynamics of motile micro-organisms. *Journal of Fluid Mechanics*, **455**, 149–174.
- Howard, L., 1961: Note on a paper of John W. Miles. *Journal of Fluid Mechanics*, **10** (04), 509–512.
- Hwang, J. H., H. Yamazaki, and C. R. Rehmann, 2006: Buoyancy generated turbulence in stably stratified flow with shear. *Physics of Fluids*, **18** (4), 045104, doi:10.1063/1.2193472.
- Ihcak, M., 2014: Energetics and mixing efficiency of lock-exchange flow. *Ocean Modelling*, (0), –, doi:10.1016/j.ocemod.2014.08.003, URL <http://www.sciencedirect.com/science/article/pii/S1463500314000997>.
- Inoue, R., and W. D. Smyth, 2009: Efficiency of mixing forced by unsteady shear flow. *Journal of Physical Oceanography*, **39** (5), 1150–1166, doi:10.1175/2008JPO3927.1.
- Jacobitz, F. G., and S. Sarkar, 1998: The effect of nonvertical shear on turbulence in a stably stratified medium. *Physics of Fluids*, **10** (5), 1158–1168.
- Jacobitz, F. G., and S. Sarkar, 1999: A direct numerical study of transport and anisotropy in a stably stratified turbulent flow with uniform horizontal shear. *Flow, Turbulence and Combustion*, **63**, 343–360.
- Jones, M. S., L. Le Baron, and T. J. Pedley, 1994: Biflagellate gyrotaxis in a shear flow. *Journal of Fluid Mechanics*, **281**, 137–158.
- Julian, P. R., W. M. Washington, L. Hembree, and C. Ridley, 1970: On the spectral distribution of large-scale atmospheric kinetic energy. *J. Atmos. Sci.*, **27** (3), 376–387, doi:10.1175/1520-0469(1970)027<0376:OTSDOL>2.0.CO;2, URL [http://dx.doi.org/10.1175/1520-0469\(1970\)027<0376:OTSDOL>2.0.CO;2](http://dx.doi.org/10.1175/1520-0469(1970)027<0376:OTSDOL>2.0.CO;2).
- Kessler, J. O., 1986: Individual and collective fluid dynamics of swimming cells. *Journal of Fluid Mechanics*, **173**, 191–205.
- Klaassen, G., and W. Peltier, 1985: The onset of turbulence in finite-amplitude Kelvin–Helmholtz billows. *Journal of Fluid Mechanics*, **155** (-1), 1–35.
- Klaassen, G., and W. Peltier, 1991: The influence of stratification on secondary instability in free shear layers. *Journal of Fluid Mechanics*, **227** (-1), 71–106.
- Koshyk, J. N., and K. Hamilton, 2001: The horizontal kinetic energy spectrum and spectral budget simulated by a high-resolution troposphere-stratosphere-mesosphere gcm. *J. Atmos. Sci.*, **58** (4), 329–348, doi:10.1175/1520-0469(2001)058<0329:THKESA>2.0.CO;2, URL <http://journals.ametsoc.org/doi/abs/10.1175/1520-0469%282001%29058%3C0329%3ATHKESA%3E2.0.CO%3B2>.
- Kukulka, T., A. J. Plueddemann, J. H. Trowbridge, and P. P. Sullivan, 2009: Significance of Langmuir circulation in upper ocean mixing: Comparison of observations and simulations. *Geophys. Res. Lett.*, **36** (10), n/a–n/a, URL <http://dx.doi.org/10.1029/2009GL037620>.

- Kukulka, T., A. J. Plueddemann, J. H. Trowbridge, and P. P. Sullivan, 2010: Rapid mixed layer deepening by the combination of Langmuir and shear instabilities: A case study. *J. Phys. Oceanogr.*, **40** (11), 2381–2400, doi:10.1175/2010JPO4403.1, URL <http://dx.doi.org/10.1175/2010JPO4403.1>.
- Large, W. G., J. C. McWilliams, and S. C. Doney, 1994: Oceanic vertical mixing: A review and a model with a nonlocal boundary layer parameterization. *Rev. Geophys.*, **32** (4), 363–403, URL <http://dx.doi.org/10.1029/94RG01872>.
- Lau, W. K., and D. E. Waliser, Eds., 2012: *Intraseasonal variability in the atmosphere-ocean climate system*. Springer.
- Leibovich, S., 1983: The form and dynamics of Langmuir circulations. *Annual Review of Fluid Mechanics*, **15** (1), 391–427.
- Lewis, D. M., 2003: The orientation of gyrotactic spheroidal micro-organisms in a homogeneous isotropic turbulent flow. *Proceedings of the Royal Society of London A*, **459**, 1293–1323.
- Li, M., and C. Garrett, 1993: Cell merging and the jet/downwelling ratio in Langmuir circulation. *Journal of Marine Research*, **51**.
- Li, M., and C. Garrett, 1995: Is Langmuir circulation driven by surface waves or surface cooling? *Journal of Physical Oceanography*, **25** (1), 64–76.
- Lvov, Y. V., and N. Yokoyama, 2009: Nonlinear wave-wave interactions in stratified flows: Direct numerical simulations. *Physica D: Nonlinear Phenomena*, **238** (8), 803–815, doi:DOI:10.1016/j.physd.2009.01.016.
- Madden, R. A., and P. R. Julian, 1971: Detection of a 40-50 day oscillation in the zonal wind in the tropical pacific. *J. Atmos. Sci.*, **28** (5), 702–708, doi:10.1175/1520-0469(1971)028<0702:DOADOI>2.0.CO;2.
- Madden, R. A., and P. R. Julian, 1972: Description of global-scale circulation cells in the tropics with a 40-50 day period. *J. Atmos. Sci.*, **29** (6), 1109–1123, doi:10.1175/1520-0469(1972)029<1109:DOGSCC>2.0.CO;2.
- McDougall, T. J., and P. M. Barker, 2011: *Getting started with TEOS-10 and the Gibbs Seawater (GSW) Oceanographic Toolbox*. Scientific Committee on Oceanic Research / International Association for the Physical Sciences of the Oceans Working Group 127, 28 pp.
- McPhaden, M. J., and Coauthors, 2009: RAMA: The Research moored array for African-Asian-Australian Monsoon Analysis and prediction. *Bull. Amer. Meteor. Soc.*, **90** (4), 459–480, doi:10.1175/2008BAMS2608.1.
- McWilliams, J. C., P. P. Sullivan, and C.-H. Moeng, 1997: Langmuir turbulence in the ocean. *Journal of Fluid Mechanics*, **334** (1), 1–30.
- Miles, J. W., 1961: On the stability of heterogeneous shear flows. *Journal of Fluid Mechanics*, **10**, 496–508.
- Miller, C. B., and P. A. Wheeler, 2012: *Biological oceanography*. John Wiley & Sons.
- Moore, G. W. K., K. Alverson, and I. A. Renfrew, 2002: A reconstruction of the air sea interaction associated with the weddell polynya. *Journal of Geophysical Research*, **32**, 1685–1698.

- Moum, J., 1996: Energy-containing scales of turbulence in the ocean. *Journal of Geophysical Research*, **101**, 14 095–14 109.
- Moum, J., D. Farmer, W. D. Smyth, L. Armi, and S. Vagle, 2003: Structure and generation of turbulence at interfaces strained by internal solitary waves propagating shoreward over the continental shelf. *Journal of Physical Oceanography*, **33** (10), 2093–2112.
- Moum, J., M. Gregg, R. Lien, and M. Carr, 1995: Comparison of turbulence kinetic energy dissipation rate estimates from two ocean microstructure profilers. *Journal of Atmospheric and Oceanic Technology*, **12**, 346–366.
- Moum, J. N., J. D. Nash, and W. D. Smyth, 2011: Narrowband oscillations in the upper equatorial ocean. Part I: Interpretation as shear instabilities. *Journal of Physical Oceanography*, **41**, 397–411.
- Moum, J. N., and Coauthors, 2014: Air-sea interactions from westerly wind bursts during the November 2011 MJO in the Indian Ocean. *Bulletin of the American Meteorological Society*.
- Müller, P., 2006: *The Equations of Oceanic Motions*. Cambridge Univ. Press.
- Mundy, C. J., and D. G. Barber, 2001: On the relationship between spatial patterns of sea ice type and the mechanisms which create and maintain the north water (now) polynya. *Atmosphere Ocean*, **39** (3), 327–341.
- Munk, W., and C. Wunsch, 1998: Abyssal recipes II: energetics of tidal and wind mixing. *Deep-Sea Research*, **45**, 1977–2010.
- Neelin, J. D., I. M. Held, and K. H. Cook, 1987: Evaporation-wind feedback and low-frequency variability in the tropical atmosphere. *J. Atmos. Sci.*, **44** (16), 2341–2348, doi:10.1175/1520-0469(1987)044<2341:EWFALF>2.0.CO;2.
- Noh, Y., G. Goh, and S. Raasch, 2011: Influence of Langmuir circulation on the deepening of the wind-mixed layer. *J. Phys. Oceanogr.*, **41** (3), 472–484, doi:10.1175/2010JPO4494.1, URL <http://dx.doi.org/10.1175/2010JPO4494.1>.
- Ohlmann, C., 2011: Personal Communication.
- Osborn, T., 1980: Estimates of the local rate of vertical diffusion from dissipation measurements. *Journal of Physical Oceanography*, **10** (1), 83–89.
- Özgökmen, T. M., I. Traian, and P. F. Fischer, 2009: Large eddy simulation of stratified mixing in a three-dimensional lock-exchange system. *Ocean Modeling*, **26** (3-4), 134–155, doi:10.1016/j.ocemod.2008.09.006.
- Patnaik, P. C., F. S. Sherman, and G. M. Corcos, 1976: A numerical simulation of Kelvin-Helmholtz waves of finite amplitude. *Journal of Fluid Mechanics*, **73** (2), 215.
- Paulson, C. A., and J. J. Simpson, 1977: Irradiance measurements in the upper ocean. *Journal of Physical Oceanography*, **7** (6), 952–956.
- Pedley, T. J., N. A. Hill, and J. O. Kessler, 1988: The growth of bioconvection patterns in a uniform suspension of gyrotactic micro-organisms. *Journal of Fluid Mechanics*, **195**, 223–237, doi:10.1017/S0022112088002393.

- Pedley, T. J., and J. O. Kessler, 1987: The orientation of spheroidal microorganisms swimming in a flow field. *Proceedings of the Royal Society of London B*, **231 (1262)**, 47–70.
- Pedley, T. J., and J. O. Kessler, 1990: A new continuum model for suspensions of gyrotactic micro-organisms. *Journal of Fluid Mechanics*, **212**, 155–182, doi:10.1017/S0022112090001914.
- Pedley, T. J., and J. O. Kessler, 1992: Hydrodynamic phenomena in suspensions of swimming microorganisms. *Annual Review of Fluid Mechanics*, **24 (1)**, 313–358.
- Pedlosky, J., 1987: *Geophysical fluid dynamics*. 2nd ed., Springer Science & Business Media.
- Pedlosky, J., 1998: *Ocean Circulation Theory*. Springer.
- Pierson, W. J., and L. Moskowitz, 1964: A proposed spectral form for fully developed wind seas based on the similarity theory of S. A. Kitaigorodskii. *Journal of Geophysical Research*, **69 (24)**, 5181–5190, doi:10.1029/JZ069i024p05181.
- Pope, S., 2000: *Turbulent Flows*. Cambridge Univ. Press.
- Press, W. H., B. P. Flannery, S. A. Teukolsky, and W. T. Vetterling, 1992: *Numerical Recipes: The Art of Scientific Computing*. 2nd ed., Cambridge University Press, Cambridge (UK) and New York.
- Pujiana, D., W. Smyth, J. Moum, and S. Warner, 2015: Distinguishing ichthyogenic turbulence from geophysical turbulence. *J. Geophys. Res.*, submitted.
- Schmidtke, S., G. C. Johnson, and J. M. Lyman, 2013: MIMOC: A global monthly isopycnal upper-ocean climatology with mixed layers. *Journal of Geophysical Research: Oceans*, **118 (4)**, 1658–1672.
- Schott, F. A., and J. P. McCreary Jr., 2001: The monsoon circulation of the Indian Ocean. *Progress in Oceanography*, **51 (1)**, 1–123, doi:10.1016/S0079-6611(01)00083-0, URL <http://www.sciencedirect.com/science/article/pii/S0079661101000830>.
- Scott, R., and F. Wang, 2005: Direct evidence of an oceanic inverse kinetic energy cascade from satellite altimetry. *Journal of Physical Oceanography*, **35 (9)**, 1650–1666.
- Scotti, A., B. Butman, R. C. Beardsley, P. S. Alexander, and S. Anderson, 2005: A modified beam-to-earth transformation to measure short-wavelength internal waves with an acoustic Doppler current profiler. *Journal of Atmospheric and Oceanic Technology*, **22 (5)**, 583–591.
- Seim, H., and M. Gregg, 1994: Detailed observations of a naturally occurring shear instability. *Journal of Geophysical Research*, **99 (C5)**, 10 049–10 073, doi:10.1029/94JC00168.
- Skyllingstad, E. D., and D. W. Denbo, 1995: An ocean large-eddy simulation of Langmuir circulations and convection in the surface mixed layer. *J. Geophys. Res.*, **100 (C5)**, 8501–8522, URL <http://dx.doi.org/10.1029/94JC03202>.
- Skyllingstad, E. D., W. D. Smyth, J. N. Moum, and H. Wijesekera, 1999: Upper-ocean turbulence during a westerly wind burst: A comparison of large-eddy simulation results and microstructure measurements. *Journal of physical oceanography*, **29 (1)**, 5–28.
- Smith, S. D., R. D. Muench, and C. H. Pease, 1990: Polynyas and leads: An overview of physical processes and environment. *Journal of Geophysical Research*, **95 (C6)**, 9461–9479.

- Smyth, W. D., 2003: Secondary Kelvin-Helmholtz instability in weakly stratified shear flow. *Journal of Fluid Mechanics*, **497**, 67–98, doi:10.1017/S0022112003006591.
- Smyth, W. D., D. Hebert, and J. N. Moum, 1996a: Local ocean response to a multiphase westerly wind burst: 1. dynamic response. *Journal of Geophysical Research: Oceans*, **101 (C10)**, 22 495–22 512, doi:10.1029/96JC02005.
- Smyth, W. D., D. Hebert, and J. N. Moum, 1996b: Local ocean response to a multiphase westerly wind burst: 2. thermal and freshwater responses. *Journal of Geophysical Research: Oceans*, **101 (C10)**, 22 513–22 533, doi:10.1029/96JC02006.
- Smyth, W. D., J. Moum, and J. D. Nash, 2011: Narrowband oscillations in the upper equatorial ocean. Part II: Properties of shear instabilities. *Journal of Physical Oceanography*, **41**, 412–428.
- Smyth, W. D., and J. N. Moum, 2001: Three-dimensional (3d) turbulence. *Encyclopedia of Ocean Sciences*, Academic Press, doi:10.1006/rwos.2001.0134.
- Smyth, W. D., and J. N. Moum, 2013: Marginal instability and deep cycle turbulence in the eastern equatorial Pacific Ocean. *Geophysical Research Letters*, **40 (23)**, 6181–6185, doi:10.1002/2013GL058403.
- Smyth, W. D., J. N. Moum, and D. R. Caldwell, 2001: The efficiency of mixing in turbulent patches: inferences from direct simulations and microstructure observations. *Journal of Physical Oceanography*, **31**, 1969–1992.
- Smyth, W. D., J. N. Moum, L. Li, and S. A. Thorpe, 2013: Diurnal shear instability, the descent of the surface shear layer, and the deep cycle of equatorial turbulence. *J. Phys. Oceanogr.*, **43 (11)**, 2432–2455, doi:10.1175/JPO-D-13-089.1, URL <http://dx.doi.org/10.1175/JPO-D-13-089.1>.
- Smyth, W. D., and W. R. Peltier, 1993: Two-dimensional turbulence in homogeneous and stratified shear layers. *Geophysical and Astrophysical Fluid Dynamics*, **69 (1)**, 1–32.
- Smyth, W. D., P. O. Zavialov, and J. N. Moum, 1997: Decay of turbulence in the upper ocean following sudden isolation from surface forcing. *J. Phys. Oceanogr.*, **27 (5)**, 810–822, doi:10.1175/1520-0485(1997)027<0810:DOTITU>2.0.CO;2.
- Soloviev, A., and R. Lukas, 2003: Observation of wave-enhanced turbulence in the near-surface layer of the ocean during TOGA COARE. *Deep Sea Research Part I*, **50 (3)**, 371–395, doi: DOI:10.1016/S0967-0637(03)00004-9.
- Spigel, R., J. Imberger, and K. Rayner, 1986: Modeling the diurnal mixed layer. *Limnology and Oceanography*, **31 (3)**, 533–556.
- Stacey, M. T., M. A. McManus, and J. V. Steinbuck, 2007: Convergences and divergences and thin layer formation and maintenance. *Limnology and Oceanography*, **52 (4)**, 1523–1532.
- Staquet, C., 1995: Two-dimensional secondary instabilities in a strongly stratified shear layer. *Journal of Fluid Mechanics*, **296**, 73–126.
- Steinbuck, J., M. Stacey, M. McManus, O. Cheriton, and J. Ryan, 2009: Observations of turbulent mixing in a phytoplankton thin layer: Implications for formation, maintenance, and breakdown. *Limnology and Oceanography*, **54 (4)**, 1353–1368.

- Sterl, A., and S. Caires, 2005: Climatology, variability and extrema of ocean waves: the web-based knmi/era-40 wave atlas. *International Journal of Climatology*, **25** (7), 963–977, doi:10.1002/joc.1175.
- Stern, M. E., 1965: Interaction of a uniform wind stress with a geostrophic vortex. *Deep Sea Research and Oceanographic Abstracts*, **12** (3), 355–367, URL <http://www.sciencedirect.com/science/article/pii/0011747165900070>.
- Stommel, H., 1949: Trajectories of small bodies sinking slowly through convection cells. *Journal of Marine Research*, **8**, 25–29.
- Suanda, S. H., 2009: Diurnal wind-driven processes on the northern Monterey bay inner shelf. M.S. thesis, College of Oceanic and Atmospheric Sciences, Oregon State University, 104 COAS Administration Building Corvallis, OR 97331-5503.
- Sullivan, J. M., P. L. Donaghay, and J. E. B. Rines, 2010a: Coastal thin layer dynamics: Consequences to biology and optics. *Continental Shelf Research*, **30** (2010), 50–65, doi:10.1016/j.csr.2009.07.009.
- Sullivan, J. M., and Coauthors, 2010b: Layered organization in the coastal ocean: An introduction to planktonic thin layers and the LOCO project. *Continental Shelf Research*, **30** (1), 1–6, doi:10.1016/j.csr.2009.09.001.
- Sullivan, P. P., J. C. McWilliams, and W. K. Melville, 2007: Surface gravity wave effects in the oceanic boundary layer: Large-eddy simulation with vortex force and stochastic breakers. *Journal of Fluid Mechanics*, **593**, 405–452.
- Talley, L. D., 2003: Shallow, intermediate, and deep overturning components of the global heat budget. *J. Phys. Oceanogr.*, **33** (3), 530–560, doi:10.1175/1520-0485(2003)033<0530:SIADOC>2.0.CO;2, URL [http://dx.doi.org/10.1175/1520-0485\(2003\)033<0530:SIADOC>2.0.CO;2](http://dx.doi.org/10.1175/1520-0485(2003)033<0530:SIADOC>2.0.CO;2).
- Tennekes, H., and J. L. Lumley, 1972: *A First Course in Turbulence*. The MIT Press.
- Thorn, G. J., and R. N. Bearon, 2010: Transport of spherical gyrotactic organisms in general three-dimensional flow fields. *Physics of Fluids*, **22** (4), 041902, doi:10.1063/1.3381168.
- Thorpe, S., 1973: Experiments on instability and turbulence in a stratified shear flow. *Journal of Fluid Mechanics*, **61** (04), 731–751.
- Thorpe, S., 2004: Langmuir circulation. *Annu. Rev. Fluid Mech.*, **36**, 55–79.
- Thorpe, S. A., 1977: Turbulence and mixing in a Scottish loch. *Phil. Trans. R. Soc. A*, **286** (1334), 125–181.
- Thorpe, S. A., 2002: The axial coherence of Kelvin-Helmholtz billows. *Quarterly Journal of the Royal Meteorological Society*, **128** (583), 1529–1542, doi:10.1002/qj.200212858307.
- Thorpe, S. A., and Z. Liu, 2009: Marginal instability? *J. Phys. Oceanogr.*, **39** (9), 2373–2381, doi:10.1175/2009JPO4153.1, URL <http://dx.doi.org/10.1175/2009JPO4153.1>.
- Torney, C., and Z. Neufeld, 2007: Transport and aggregation of self-propelled particles in fluid flows. *Physical Review Letters*, **99**, 078101, doi:10.1103/PhysRevLett.99.078101.
- UNESCO, 1981: Tenth report of the joint panel on oceanographic tables and standards. 25 pp.

- van Haren, H., and L. Gostiaux, 2010: A deep-ocean Kelvin-Helmholtz billow train. *Geophysical Research Letters*, **37** (3), L03 605.
- Van Meurs, P., 1998: Interactions between near-inertial mixed layer currents and the mesoscale: The importance of spatial variabilities in the vorticity field*. *Journal of physical oceanography*, **28** (7), 1363–1388.
- Vinnichenko, N. K., 1970: The kinetic energy spectrum in the free atmosphere—1 second to 5 years. *Tellus*, **22** (2), 158–166, URL <http://dx.doi.org/10.1111/j.2153-3490.1970.tb01517.x>.
- Wang, D., and P. Müller, 2002: Effects of equatorial undercurrent shear on upper-ocean mixing and internal waves. *J. Phys. Oceanogr.*, **32** (3), 1041–1057, doi:10.1175/1520-0485(2002)032<1041:EOEUSO>2.0.CO;2, URL [http://dx.doi.org/10.1175/1520-0485\(2002\)032<1041:EOEUSO>2.0.CO;2](http://dx.doi.org/10.1175/1520-0485(2002)032<1041:EOEUSO>2.0.CO;2).
- Wheeler, M. C., and H. H. Hendon, 2004: An all-season real-time multivariate MJO index: Development of an index for monitoring and prediction. *Monthly Weather Review*, **132** (8), 1917–1932.
- Wilcox, D. C., 2006: *Turbulence Modeling for CFD*. 3rd ed., DCW Industries, Inc., 5354 Palm Drive, La Cañada, Ca 91011.
- Winters, K. B., J. A. MacKinnon, and B. Mills, 2004: A spectral model for process studies of rotating, density-stratified flows. *Journal of Atmospheric and Oceanic Technology*, **21**, 69–94.
- Woods, J. D., 1968: Wave-induced shear instability in the summer thermocline. *Journal of Fluid Mechanics*, **32** (04), 791–800.
- Wunsch, C., 1998: The work done by the wind on the oceanic general circulation. *J. Phys. Oceanogr.*, **28** (11), 2332–2340, doi:10.1175/1520-0485(1998)028<2332:TWDBTW>2.0.CO;2, URL [http://dx.doi.org/10.1175/1520-0485\(1998\)028<2332:TWDBTW>2.0.CO;2](http://dx.doi.org/10.1175/1520-0485(1998)028<2332:TWDBTW>2.0.CO;2).
- Wunsch, C., and R. Ferrari, 2004: Vertical mixing, energy, and the general circulation of the oceans. *Annu. Rev. Fluid Mech.*, **36** (1), 281–314, doi:10.1146/annurev.fluid.36.050802.122121, URL <http://dx.doi.org/10.1146/annurev.fluid.36.050802.122121>.
- Wyrtki, K., 1973: An equatorial jet in the Indian Ocean. *Science*, **181** (4096), 262–264.
- Yoneyama, K., C. Zhang, and C. N. Long, 2013: Tracking pulses of the Madden-Julian oscillation. *Bulletin of the American Meteorological Society*, **94** (12), 1871–1891.
- You, Y., 1995: Salinity variability and its role in the barrier-layer formation during toga-coare. *J. Phys. Oceanogr.*, **25** (11), 2778–2807, doi:10.1175/1520-0485(1995)025<2778:SVAIRI>2.0.CO;2, URL [http://dx.doi.org/10.1175/1520-0485\(1995\)025<2778:SVAIRI>2.0.CO;2](http://dx.doi.org/10.1175/1520-0485(1995)025<2778:SVAIRI>2.0.CO;2).
- Young, I., 1999: Seasonal variability of the global ocean wind and wave climate. *International Journal of Climatology*, **19** (9), 931–950.
- Zhang, C., 2005: Madden-Julian oscillation. *Reviews of Geophysics*, **43** (2).
- Zhang, C., 2013: Madden-Julian oscillation: Bridging weather and climate. *Bulletin of the American Meteorological Society*, **94** (12), 1849–1870.

APPENDICES

A TRAPPING OF GYROTACTIC ORGANISMS IN AN UNSTABLE SHEAR LAYER

Martín S. Hoecker-Martínez,

William D. Smyth

Continental Shelf Research

Journals Customer Service

3251 Riverport Lane

Maryland Heights, MO 63043, USA

#36

A.1 NUMERICAL IMPLEMENTATION

To simplify the imposing boundary conditions a linear function is removed from the buoyancy field

$$b' = b - N^2 z \quad (\text{A.1})$$

with N^2 determined by the condition that $b' = 0$ at the upper and lower boundaries. For realistic ocean conditions this large scale stratification is stable and adds a quadratic term to the hydrostatic pressure field. If we define a perturbation pressure

$$p' = p + \frac{1}{2} N^2 z^2 \quad (\text{A.2})$$

then we recover the original differential equation with the additional term representing the large scale stratification

$$\frac{\partial u_i}{\partial t} = -u_j \nabla_j u_i - \nabla_i p' + b' \delta_{3i} + \nu \nabla^2 u_i \quad (\text{A.3})$$

$$\frac{\partial b'}{\partial t} = -u_j \nabla_j b' - N^2 u_3 + \kappa \nabla^2 b' \quad (\text{A.4})$$

$$\nabla^2 p' = -(\nabla_i u_j)(\nabla_j u_i) + \frac{\partial b'}{\partial x_3}. \quad (\text{A.5})$$

In these reduced variables we can impose boundary conditions which correspond to a free shear layer in a nearly two layer fluid using a Fourier decomposition (Winters et al., 2004). A transform in wave-number space reduces the equations (A.3) and (A.5) to

$$\begin{aligned} e^{-\nu k^2 t} \frac{\partial}{\partial t} \left(e^{\nu k^2 t} \mathcal{F}(u_i) \right) \\ = -ik_j \mathcal{F}(u_j u_i) - ik_i \mathcal{F}(p') + \mathcal{F}(b') \delta_{3i} \end{aligned} \quad (\text{A.6})$$

$$\begin{aligned} e^{-\kappa k^2 t} \frac{\partial}{\partial t} \left(e^{\kappa k^2 t} \mathcal{F}(b') \right) \\ = -ik_j \mathcal{F}(u_j b') - N^2 \mathcal{F}(u_3) \end{aligned} \quad (\text{A.7})$$

$$\mathcal{F}(p') = \frac{-k_i k_j \mathcal{F}(u_j u_i) - ik_3 \mathcal{F}(b')}{k^2} \quad (\text{A.8})$$

where integrating factors of $e^{\nu k^2 t}$ and $e^{\kappa k^2 t}$ have been used for the diffusive terms in velocity u_i and buoyancy b' respectively and products in advective terms are calculated in real space and transformed into Fourier space. The FFTW routines of Frigo and Johnson (2005) are used to perform the numerical Fourier transform.

The time stepping algorithm used is an explicit predictor corrector and is accurate to second order (Burden and Faires, 2004). All variables are advanced in Fourier space. Operating in Fourier space allows for exact solution of the diffusive terms by use of integrating factors [see (A.6, A.7)]. Advective terms are calculated in real space and then transformed back into Fourier space. Pressure is not used as a prognostic variable since it arises from the time derivative of incompressibility $\frac{\partial}{\partial t} \nabla_i u_i = 0$ and numerical rounding errors may allow for the flow to accrue significant divergence over time. Instead pressure is solved implicitly by projection. The new velocity field u is obtained from the possibly divergent field u^* by solving

$$\mathcal{F}(u_i) = \mathcal{F}(u_i^*) + k_i \frac{k_j \mathcal{F}(u_j^*)}{k^2} \quad (\text{A.9})$$

at each fractional time step for every non-zero wavenumber \vec{k} . This removes any divergence introduced into the flow at that time step.

The underlying fluid model is validated comparing growth rates from Hazel (1972) at high Reynolds number, $\text{Re} = 1500$, to approximate inviscid flow and high Richardson number, $\text{Ri} = 0.17$. After the initial buoyancy anomaly rings down in Figure A.1, $t \times \Delta U / h = 40$, the layer thickness has grown by $\pi t \Delta U / 2h \text{RePr}$ and the growth rate decreases by $\approx 4\%$. The growing Kelvin-Helmholtz instability is similar to the simulations of Corcos and Sherman (1976) and Patnaik et al. (1976), which supports their claims that the evolution of the flow is insensitive to the initial perturbation or the exact form of the shear layer. Their initial velocity profile was an error function with initial perturbations tuned to the fastest growing mode.

The random perturbation introduced at $t = 0$ can cause spurious mixing if it is too large. To test whether the stratification is strongly influenced by the perturbation, an integral length scale $h(t)$ is calculated using horizontal averages of buoyancy

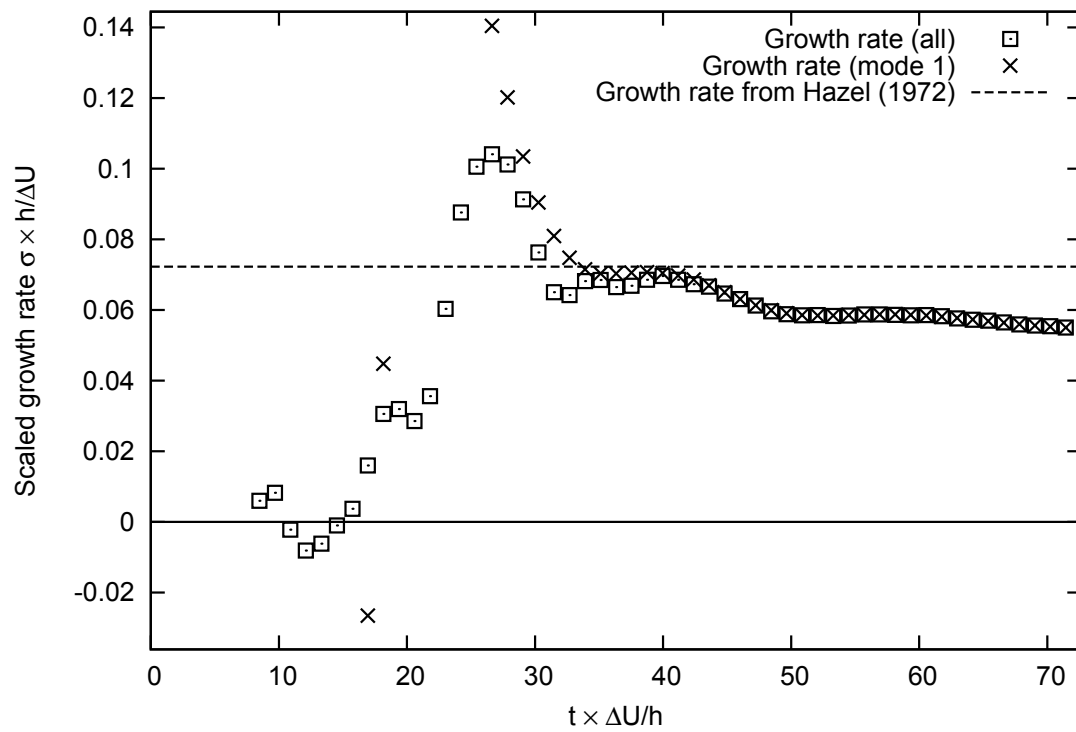


Figure A.1: Growth rates of buoyancy anomalies as a function of normalized time $t/\tau = t\Delta U/h$ from run k

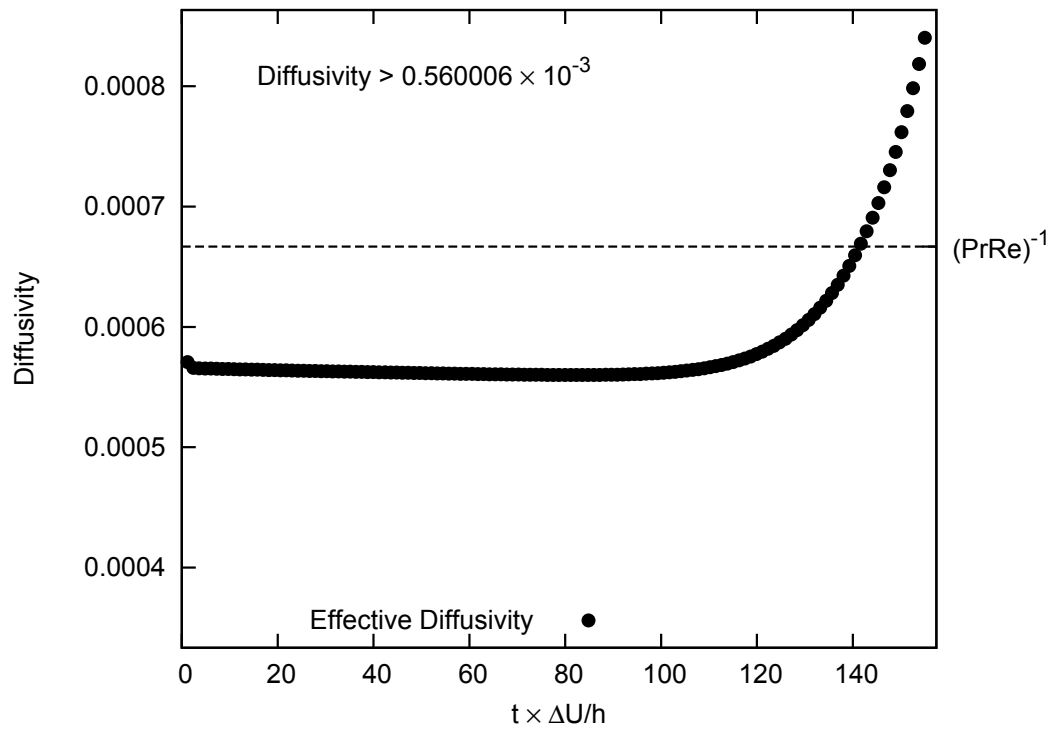


Figure A.2: Effective diffusivity from run k

$$h(t) = \int_{-\frac{L_z}{2}}^{\frac{L_z}{2}} 1 - \left(\frac{\bar{b}}{\Delta b} \right)^2 dz, \quad (\text{A.10})$$

which initially evaluates to the length h in the expression of the initial density profile (2.5). If the profile evolution is purely diffusive a similarity solution may be found following Pope (2000) using the boundary conditions on b and the value of the vertical derivative at the center of the shear layer

$$\frac{1}{\pi} \frac{d}{d\tau} \left(\frac{h^2}{h_0^2} \right) \approx \frac{\kappa}{\Delta U_0 h_0} = (\text{Pr Re})^{-1}. \quad (\text{A.11})$$

The scaled derivative of h^2 from the run k is shown in Figure A.2 is initially constant characteristic of diffusive mixing. This run is chosen as it is closest to realistic conditions and is the jumping off point for our extrapolations to the oceanic parameter regime.

A.2 THE EFFECTS OF CELL ELLIPTICITY

The above analysis assumed a spherical shape for the organisms. Pedley and Kessler (1992) give the torsional balance for an elliptical gyrotactic object. Ellipticity couples the particle orientation to the strain field via the viscous torque given by

$$\begin{aligned} \tau'_i = & \rho\nu V (\alpha_{\parallel} p_i p_j + \alpha_{\perp} (\delta_{ij} - p_i p_j)) \times \\ & \left(\frac{1}{2} \epsilon_{jkl} \nabla_k u_l - \Omega_j + \alpha_0 \epsilon_{jkl} p_k e_{lm} p_m \right) \end{aligned} \quad (\text{A.12})$$

where α_0 is the ellipticity defined as

$$\alpha_0 = \frac{1 - r^2}{1 + r^2} \quad (\text{A.13})$$

with r is the ratio of the major and minor axes and $\alpha_{\parallel, \perp}$ are non-dimensional numbers which quantify the resistance to relative rotation about an axis parallel or perpendicular to the symmetry axis. For a sphere $\alpha_{\parallel} = \alpha_{\perp} = 6$. V is the volume and p is the vector pointing in the direction of swimming (assumed to be up in quiescent fluid).

Following the argument for spherical gyrotaxis of small objects the net torque must vanish. If we assume motion is restricted to an x - z plane we can further simplify the expression since the angular velocity and the vorticity only have one component $\Omega_2, \epsilon_{2ij} \nabla_j u_k$. The orientation also

has no component in that direction $p_2 = 0$. Using the subscripts $\{a, b, c, \dots\}$ to denote the two dimensions in the problem,

$$0 = -\ell\epsilon_{2ab}p_a g_b + \nu\alpha_{\perp} \left(\frac{1}{2}\epsilon_{2ab}\nabla_a u_b - \Omega_2 + \alpha_0\epsilon_{2ab}p_a e_{bc}p_c \right) \quad (\text{A.14})$$

if the co-ordinate system x_i is oriented along the principal axes of the strain rate tensor so that $e_{ab}x_b = (\lambda^1 x_1, 0, \lambda^3 x_3)$ where the angle between x_3 and the z -axis is ϕ and the angle between the orientation and x_3 is θ . Since the flow is two dimensional and incompressible the eigenvalues are equal in magnitude and opposite in sign a rotated version of the term in simple gyrotaxis can be recovered.

$$\Omega = (g\ell \sin(\theta - \phi)) / (\alpha_{\perp}\nu) + \frac{1}{2}\epsilon_{2ab}\nabla_a u_b + \alpha_0\lambda \sin(2\theta) \quad (\text{A.15})$$

Assuming that the fluid vorticity is essentially a shear $\epsilon_{2ab}\nabla_a u_b = S$ and using the gyrotactic restoration rate $B = 3\nu/\ell g$ from Kessler (1986)

$$\Omega = \frac{1}{2}S \left(\frac{1}{BS} \sin(\theta - \phi) + 1 + \frac{2\alpha_0\lambda}{S} \sin(2\theta) \right). \quad (\text{A.16})$$

The first two terms are simply a recasting of (2.8). In the third term $\sin(2\theta)$ and the shape term α_0 are bounded by ± 1 . To estimate the relative importance of the ellipticity term, an estimate must be made for the ratio $2\lambda/S$. The simulations of Staquet (1995) and Smyth (2003) all achieved ratios of strain to shear λ/S below $1/40$. This is much smaller than the instability criterion for gyrotaxis of spherical particles $1/BS \sim 1$. We conclude that for nearly stable organisms in a Kelvin-Helmholtz instability, the influence of ellipticity may be ignored.

A.3 THE EFFECTS OF INERTIA ON CELL MOTION

Kessler (1986) and Hopkins and Fauci (2002) derive (2.7) for the angular acceleration of a small gyrotactic organism. For (2.8) to be valid the size of the organism must be below a threshold. To estimate the size of object for whom inertial effects may be ignored we need to estimate the timescale for inertial rotary motion. For objects that are small relative to the size of flow features

the response time of orientation may be estimated using the homogeneous equation

$$I\vec{\alpha} = +\frac{4\pi}{3}r^3\rho\left(\vec{L}\times\vec{g}\right) - 8\pi\rho\nu r^3\vec{\Omega}. \quad (\text{A.17})$$

The moment of inertia tensor is given by $I = K\rho r^5$ where the tensor K is a geometric constant whose principal values are of order unity. If we restrict the motion to an x - z plane the tensor K becomes a scalar. Following Kessler (1986) the moment arm of the center of mass should be proportional to the radius of the organism $\ell = \lambda r$

$$K\rho r^5\frac{d^2\theta}{dt^2} = -\frac{4\pi}{3}\rho r^4 g\lambda\sin\theta - 8\pi\rho\nu r^3\frac{d\theta}{dt}. \quad (\text{A.18})$$

Expanding the sine near the equilibrium, a solution of the form $\theta \propto e^{\sigma t}$ can be found with two modes

$$\sigma = -\frac{4\pi\nu}{Kr^2}\left(1 \pm \sqrt{1 - \frac{g\lambda Kr^3}{12\pi\nu^2}}\right). \quad (\text{A.19})$$

Using a binomial expansion we find a gravitational mode and an inertial mode.

$$\sigma = \begin{cases} -\frac{8\pi\nu}{Kr^2} \rightarrow \infty & \text{as } r \rightarrow 0 \\ -\frac{g\lambda r}{6\nu} \rightarrow 0 & \text{as } r \rightarrow 0 \end{cases}. \quad (\text{A.20})$$

The inertial mode decays rapidly while the slowly decaying mode gives the relationship the governing equation for a system where viscous and gravitational torques are balanced.

$$6\nu\frac{d\theta}{dt} = -g\ell\theta \quad (\text{A.21})$$

For the binomial expansion to be valid the radius of the particle must satisfy

$$r \ll \left(\frac{12\pi\nu^2}{g\lambda K}\right)^{1/3}. \quad (\text{A.22})$$

which for oceanic values of viscosity $\nu \approx 10^{-6}\text{m}^2/\text{s}$ and using a mass offset from Kessler (1986) $\lambda \approx 0.01$ implies $r \ll 1\text{mm}$. As size approaches this limit inertial effects must be included (e.g. Hopkins and Fauci (2002)). Below this threshold value inertial effects may be ignored and (2.8)

may be used. Any organism that is small enough to satisfy (A.22) is smaller than Kolmogorov scale of oceanic flow features $r \ll \eta$ for all but the most extreme mixing events $\epsilon \sim 10^{-4}$ W/kg Soloviev and Lukas (2003)].

B LARGE EDDY SIMULATION TURBULENCE CLOSURE

Martín S. Hoecker-Martínez,

William D. Smyth,

Eric D. Skyllingstad

Journal of Physical Oceanography

American Meteorological Society

45 Beacon Street

Boston, MA 02108-3693

#??

The sub-grid scale fluxes use a Smagorinsky (first-order) closure model which gives the eddy velocity

$$\nu_t(\vec{x}) = 14 \times 10^{-5} \Delta x \sqrt{\frac{\langle \Delta u_{HP}^2(\vec{x}, \vec{r}) \rangle_{\|\vec{r}\|=\Delta x}}{\kappa^3}} \quad (\text{B.1})$$

$$\Delta u_{HP}^2(\vec{x}, \vec{r}) = \|\vec{u}_{HP}(\vec{x}) - \vec{u}_{HP}(\vec{x} + \vec{r})\|^2 \quad (\text{B.2})$$

in terms of the variance of the (high pass filtered) velocity Δu_{HP}^2 and the grid spacing Δx (Ducros et al., 1996; Wilcox, 2006). In the presence of large scale gradients the unfiltered velocity overestimates the local kinetic energy. To filter out large scale gradients we use a discrete Laplacian whose vertical second derivative term has been neglected to remove the influence of strong vertical gradients supported by stratification

$$\begin{aligned} \nabla_H^2(u) &= \frac{u}{4} \begin{pmatrix} +\delta(x + \Delta x) - 2\delta(x) + \delta(x - \Delta x) \\ +\delta(y + \Delta y) - 2\delta(y) + \delta(y - \Delta y) \end{pmatrix}. \end{aligned} \quad (\text{B.3})$$

This is analogous to the method of (Ducros et al., 1996) for bounded flows in which the wall normal direction is neglected and a two dimensional Laplacian is used to remove large scale gradients. The resulting filter transfer function

$$\nabla_H^2(u) = u(k, l) \left(\sin^2 \left(\frac{k\Delta x}{2} \right) + \sin^2 \left(\frac{l\Delta y}{2} \right) \right) \quad (\text{B.4})$$

is of order unity at the Nyquist wave-number of the simulation (the average value of the filter transfer function for a cubic grid, $\Delta x = \Delta y$ at $\|k_{Ny}\| = \frac{2\pi}{\Delta x}$ is 1.3). The Laplacian is iterated three times

$$u_{HP} = \nabla_H^2 (\nabla_H^2 (\nabla_H^2 (u))) \quad (\text{B.5})$$

to strongly suppress the influence of large scales. In addition to Smagorinsky sub-grid scale viscosity a high order hyper-viscosity term is included in equation 4.4 with a constant coefficient $\alpha = 0.001$. This prevents aliasing by damping the smallest scales of motion.

C EDDY PERTURBATIONS ON EKMAN PUMPING

In an extreme departure from the rest of the ideas in this thesis I am going to explore the interaction of meso-scale eddies with wind forcing. The goal of this approximation is to parse the terms into an ordered list thereby allowing for incremental improvement. The scale separation of atmospheric and oceanic length scales allows significant simplification but a few terms remain dependent of the curl of the ocean velocity, and the change of planetary vorticity (β -effect). The ordering the resulting terms is somewhat ambiguous but the most important terms are highlighted. As contrast the example of fast ocean eddies and weak winds is also calculated.

C.1 DEFINITIONS AND ASSUMPTIONS

To examine the deviations of air-sea interaction it is useful to define air velocity u^a , ocean velocity u^o , and relative velocity

$$u_i^r = u_i^a - u_i^o \quad (\text{C.1})$$

The simplest approximation for wind stress is a drag coefficient

$$\tau_i = \rho_a C_D u_i^r \sqrt{u_j^r u_j^r} \quad (\text{C.2})$$

Define total Ekman pumping as a function of ocean density ρ_0 , surface stress, and total vorticity ($f + \nabla \times \mathbf{u}^o$) assuming the low Rossby number scaling of Stern (1965) holds

$$W = \frac{1}{\rho_o} \nabla \times \left(\frac{\tau}{f + \nabla \times \mathbf{u}^o} \right) \quad (\text{C.3})$$

C.2 STRONG WINDS

Assuming characteristic air speed $S = \sqrt{\langle u_i^a u_i^a \rangle}$ is much larger than the characteristic ocean speed $s = \sqrt{\langle u_i^o u_i^o \rangle}$ define a scaled ocean and air velocity

$$o_i = \frac{u_i^o}{s} \quad (\text{C.4})$$

$$a_i = \frac{u_i^a}{S} \quad (\text{C.5})$$

Writing τ_i as a function of o_i and s

$$\tau_i = \rho_a C_D S^2 \left(a_i - \frac{s}{S} o_i \right) \sqrt{a_j a_j - 2 \frac{s}{S} a_j o_j - \left(\frac{s}{S} \right)^2 o_j o_j} \quad (\text{C.6})$$

Writing W as a function of o_i , and s

$$W = \frac{1}{\rho_o} \epsilon_{3jk} \nabla_j \left(\frac{\rho_a C_D S^2 \left(a_k - \frac{s}{S} o_k \right) \sqrt{a_m a_m - 2 \frac{s}{S} a_m o_m - \left(\frac{s}{S} \right)^2 o_m o_m}}{f + \epsilon_{3lm} \nabla_l s o_m} \right) \quad (\text{C.7})$$

Scaling the Coriolis parameter by the current speed seeking to form a Rossby number $\text{Ro} = s/f\ell$ of the eddy and removing the uniform scaling factors for velocity S from the derivative we are left with a function of a small parameters $r = s/S$, o_i , and a_i

$$W = C_D S \frac{\rho_a}{\rho_o} \frac{\ell}{r} \epsilon_{3jk} \nabla_j \left(\frac{(a_k - r o_k) \sqrt{a_m a_m - 2 r a_m o_m + r^2 o_m o_m}}{\frac{f\ell}{s} + \ell \epsilon_{3lm} \nabla_l o_m} \right) \quad (\text{C.8})$$

distribute the derivatives across the multiplication and division

$$W = C_D S \frac{\rho_a}{\rho_o} \left(\begin{aligned} & + \frac{1}{r} \frac{\sqrt{a_m a_m - 2 r a_m o_m + r^2 o_m o_m} \ell \epsilon_{3jk} \nabla_j (a_k - r o_k)}{\frac{f\ell}{s} + \ell \epsilon_{3lm} \nabla_l o_m} \\ & + \frac{1}{r} \frac{(a_k - r o_k) \ell \epsilon_{3jk} \nabla_j (a_m a_m - 2 r a_m o_m + r^2 o_m o_m)}{2 \left(\frac{f\ell}{s} + \ell \epsilon_{3lm} \nabla_l o_m \right) (a_m a_m - 2 r a_m o_m + r^2 o_m o_m)^{\frac{3}{2}}} \\ & - \frac{1}{r} \frac{(a_k - r o_k) \sqrt{a_m a_m - 2 r a_m o_m + r^2 o_m o_m} \ell \epsilon_{3jk} \nabla_j \left(\frac{f\ell}{s} + \ell \epsilon_{3lm} \nabla_l o_m \right)}{\left(\frac{f\ell}{s} + \ell \epsilon_{3lm} \nabla_l o_m \right)^2} \end{aligned} \right) \quad (\text{C.9})$$

rewriting the magnitude of the scaled relative wind $\sqrt{a_m a_m - 2 r a_m o_m + r^2 o_m o_m}$ wherever it appears outside a derivative as $|\vec{a} - r \vec{o}|$ for brevity

$$W = C_D S \frac{\rho_a}{\rho_o} \left(\begin{aligned} & + \frac{1}{r} \frac{|\vec{a} - r \vec{o}|}{\frac{f\ell}{s} + \ell \epsilon_{3lm} \nabla_l o_m} \ell \epsilon_{3jk} \nabla_j (a_k - r o_k) \\ & + \frac{1}{r} \frac{(a_k - r o_k)}{\frac{f\ell}{s} + \ell \epsilon_{3lm} \nabla_l o_m} \frac{\ell \epsilon_{3jk} \nabla_j (a_m a_m - 2 r a_m o_m + r^2 o_m o_m)}{2 |\vec{a} - r \vec{o}|^3} \\ & - \frac{1}{r} \frac{(a_k - r o_k) |\vec{a} - r \vec{o}|}{\left(\frac{f\ell}{s} + \ell \epsilon_{3lm} \nabla_l o_m \right)^2} \ell \epsilon_{3jk} \nabla_j \left(\frac{f\ell}{s} + \ell \epsilon_{3lm} \nabla_l o_m \right) \end{aligned} \right) \quad (\text{C.10})$$

remove common factor of $|\vec{a} - r \vec{o}| / \left(\frac{f\ell}{s} + \ell \epsilon_{3lm} \nabla_l o_m \right)$

$$W = \frac{C_D S \frac{\rho_a}{\rho_o} |\vec{a} - r \vec{o}|}{\frac{f\ell}{s} + \ell \epsilon_{3lm} \nabla_l o_m} \left(\begin{aligned} & + \frac{1}{r} \ell \epsilon_{3jk} \nabla_j (a_k - r o_k) \\ & + \frac{1}{r} \frac{(a_k - r o_k) \ell \epsilon_{3jk} \nabla_j (a_m a_m - 2 r a_m o_m + r^2 o_m o_m)}{2 |\vec{a} - r \vec{o}|^4} \\ & - \frac{1}{r} \frac{(a_k - r o_k) \ell \epsilon_{3jk} \nabla_j \left(\frac{f\ell}{s} + \ell \epsilon_{3lm} \nabla_l o_m \right)}{\left(\frac{f\ell}{s} + \ell \epsilon_{3lm} \nabla_l o_m \right)} \end{aligned} \right) \quad (\text{C.11})$$

The leading term scales using Rossby number and the Ekman pumping relation (C.3) assumes small Rossby number and taking the $\text{Ro} \rightarrow 0$ limit is informative

$$\frac{C_D S \frac{\rho_a}{\rho_o} |\vec{a} - r\vec{o}|}{\frac{f\ell}{s} + \ell\epsilon_{31m} \nabla_{10m}} \approx \frac{C_D S \frac{\rho_a}{\rho_o} \text{Ro}}{1 + \text{Ro}} \approx C_D S \frac{\rho_a}{\rho_o} \text{Ro} \text{ as } \text{Ro} \rightarrow 0 \quad (\text{C.12})$$

If we then expand collected terms, group derivatives with ℓ , for clarity terms involve variation of the scaled wind \vec{a} are red and variation in the Coriolis parameter f are blue. Individual terms are given their scaling in the limit of small r and small Rossby number simplification.

$$W = \frac{C_D S \frac{\rho_a}{\rho_o} |\vec{a} - r\vec{o}|}{\frac{f\ell}{s} + \ell\epsilon_{31m} \nabla_{10m}} \left(\begin{array}{ccc} & \text{Scaled} & \text{Ro} \ll 1 \\ +\frac{1}{r} \ell \epsilon_{3jk} \nabla_j a_k & \frac{1}{r} \frac{\ell}{L} & \frac{1}{r} \frac{\ell}{L} \\ -\ell \epsilon_{3jk} \nabla_j o_k & 1 & 1 \\ +\frac{1}{r} \frac{a_k a_m \ell \epsilon_{3jk} \nabla_j (a_m)}{|\vec{a} - r\vec{o}|^4} & \frac{1}{r} \frac{\ell}{L} & \frac{1}{r} \frac{\ell}{L} \\ -\frac{a_k o_m \ell \epsilon_{3jk} \nabla_j (a_m)}{|\vec{a} - r\vec{o}|^4} & \frac{\ell}{L} & \frac{\ell}{L} \\ -\frac{a_k a_m \ell \epsilon_{3jk} \nabla_j (o_m)}{|\vec{a} - r\vec{o}|^4} & 1 & 1 \\ +r \frac{a_k o_m \ell \epsilon_{3jk} \nabla_j (o_m)}{|\vec{a} - r\vec{o}|^4} & r & r \\ -\frac{o_k a_m \ell \epsilon_{3jk} \nabla_j (a_m)}{|\vec{a} - r\vec{o}|^4} & \frac{\ell}{L} & \frac{\ell}{L} \\ +r \frac{o_k o_m \ell \epsilon_{3jk} \nabla_j (a_m)}{|\vec{a} - r\vec{o}|^4} & r \frac{\ell}{L} & r \frac{\ell}{L} \\ +r \frac{o_k a_m \ell \epsilon_{3jk} \nabla_j (o_m)}{|\vec{a} - r\vec{o}|^4} & r & r \\ -r^2 \frac{o_k o_m \ell \epsilon_{3jk} \nabla_j (o_m)}{|\vec{a} - r\vec{o}|^4} & r^2 & r^2 \\ -\frac{1}{r} \frac{a_k \ell \epsilon_{3jk} \nabla_j \left(\frac{f\ell}{s} \right)}{\frac{f\ell}{s} + \ell\epsilon_{31m} \nabla_{10m}} & \frac{1}{r} \frac{1}{\text{Ro}_{\text{eq}}} \frac{\text{Ro}}{1 + \text{Ro}} & \frac{1}{r} \frac{\text{Ro}}{\text{Ro}_{\text{eq}}} \\ -\frac{1}{r} \frac{a_k \ell \epsilon_{3jk} \nabla_j (\ell \epsilon_{31m} \nabla_{10m})}{\frac{f\ell}{s} + \ell\epsilon_{31m} \nabla_{10m}} & \frac{1}{r} \frac{\text{Ro}}{1 + \text{Ro}} & \frac{1}{r} \text{Ro} \\ +\frac{o_k \ell \epsilon_{3jk} \nabla_j \left(\frac{f\ell}{s} \right)}{\frac{f\ell}{s} + \ell\epsilon_{31m} \nabla_{10m}} & \frac{1}{\text{Ro}_{\text{eq}}} \frac{\text{Ro}}{1 + \text{Ro}} & \frac{\text{Ro}}{\text{Ro}_{\text{eq}}} \\ +\frac{o_k \ell \epsilon_{3jk} \nabla_j (\ell \epsilon_{31m} \nabla_{10m})}{\frac{f\ell}{s} + \ell\epsilon_{31m} \nabla_{10m}} & \frac{\text{Ro}}{1 + \text{Ro}} & \text{Ro} \end{array} \right) \quad (\text{C.13})$$

an equatorial Rossby $\text{Ro}_{\text{eq}} = s/\beta\ell^2$ number is used in the scaling. The theory of Stern (1965) assumes a small Rossby number, hence we include a small Rossby approximation to each scaling. Geostrophic air speeds are typically greater than the ocean speeds and $r < 1$ over much of the world ocean, similarly oceanic eddy length scales ℓ are smaller than atmospheric scales L and the ratio will be small $\ell/L < 1$. Both o_i and a_i have been scaled so that we may estimate them as order unity and derivatives with division by the appropriate length scale. Many of the terms which scale as the inverse speed ratio r^{-1} may be ignored when the oceanic length scale is smaller than the atmospheric length scale. Two inverse speed ratio r^{-1} terms are not suppressed by the separation of atmospheric and oceanic length scales. The first

comes about by variation of the vorticity perpendicular to the wind

$$W_{\text{NL}} = -C_D S \frac{\rho_a}{s \rho_o} |\vec{a} - r\vec{o}| \overbrace{a_k \ell \epsilon_{3jk} \nabla_j (\ell \epsilon_{3lm} \nabla_l o_m)}^{\text{Variation of } \vec{\nabla} \times \vec{u}_o \perp \vec{u}_a} \propto \left(\frac{C_D S \frac{\rho_a}{\rho_o} \text{Ro}}{1 + \text{Ro}} \right) \frac{\text{Ro} \frac{S}{s}}{1 + \text{Ro}} \quad (\text{C.14})$$

The other involves the β effect and if the ratio $\beta\ell/f \sim r$ with a zonal wind can be of order 1.

$$W_\beta = \frac{C_D S \frac{\rho_a}{\rho_o} |\vec{a} - r\vec{o}|}{\frac{f\ell}{s} + \ell \epsilon_{3lm} \nabla_l o_m} \frac{1}{r} \overbrace{\ell \vec{a} \times \vec{\nabla} \left(\frac{f\ell}{s} \right)}^{\text{for zonal wind } = \beta\ell^2/s} \propto \left(\frac{C_D S \frac{\rho_a}{\rho_o} \text{Ro}}{1 + \text{Ro}} \right) \frac{\frac{\text{Ro}}{\text{Ro}_{\text{eq}}} \frac{S}{s}}{1 + \text{Ro}} \quad (\text{C.15})$$

The term involving the β effect term may be ignored only if the wind direction is parallel to the gradient of f (ie meridional) or if the ratio $\beta\ell/f \leq r^2$. The NL term may be ignored if $\text{Ro} < r$. If all these conditions are satisfied this leaves two terms surviving to zeroth order in r , the curl of the oceanic velocity inducing a negative curl in the relative wind,

$$W_{\text{awesome}} = -C_D S \frac{\rho_a}{\rho_o} \frac{|\vec{a} - r\vec{o}|}{\frac{f\ell}{s} + \ell \epsilon_{3lm} \nabla_l o_m} \ell \epsilon_{3jk} \nabla_j o_k \propto \frac{C_D S \frac{\rho_a}{\rho_o} \text{Ro}}{1 + \text{Ro}} \quad (\text{C.16})$$

and a perturbation due to variation in the apparent magnitude of the relative wind due to variations the dependence of air sea momentum transfer on the square of relative velocity

$$W_{\text{wicked}} = -C_D S \frac{\rho_a}{\rho_o} \frac{a_k a_m \ell \epsilon_{3jk} \nabla_j (o_m)}{\left(\frac{f\ell}{s} + \ell \epsilon_{3lm} \nabla_l o_m \right) |\vec{a} - r\vec{o}|^3} \propto \frac{C_D S \frac{\rho_a}{\rho_o} \text{Ro}}{1 + \text{Ro}} \quad (\text{C.17})$$

C.3 WEAK WINDS

in the case where wind speeds are much smaller than ocean speeds the ratio of speeds becomes a large parameter $r > 1$. This can be accommodated in equation C.13 by factoring r out of $|\vec{a} - r\vec{o}|$ wherever it appears so that the magnitude is unity in the limit $r \rightarrow \infty$. Note that the common factor now scales with ocean velocity s not air velocity S and all of the terms which arise from changes in the magnitude of the apparent wind are strongly suppressed. The convention where terms involving variation of the scaled wind \vec{a} are red and variation in the Coriolis parameter f are blue is retained. Individual terms are given their

scaling in the limit of large r and small Rossby number simplification.

$$W = \frac{C_{Ds} \frac{\rho_a}{\rho_o} |\vec{a}/r - \vec{o}|}{\frac{f\ell}{s} + \ell\epsilon_{3lm} \nabla_l o_m} \left(\begin{array}{ccc} & \text{Scaled} & \text{Ro} \ll 1 \\ +\frac{1}{r} \ell\epsilon_{3jk} \nabla_j a_k & \frac{1}{r} \frac{\ell}{L} & \frac{1}{r} \frac{\ell}{L} \\ -\ell\epsilon_{3jk} \nabla_j o_k & 1 & 1 \\ +\frac{1}{r^5} \frac{a_k a_m \ell\epsilon_{3jk} \nabla_j (a_m)}{|\vec{a}/r - \vec{o}|^4} & \frac{1}{r^5} \frac{\ell}{L} & \frac{1}{r^5} \frac{\ell}{L} \\ -\frac{1}{r^4} \frac{a_k o_m \ell\epsilon_{3jk} \nabla_j (a_m)}{|\vec{a}/r - \vec{o}|^4} & \frac{1}{r^4} \frac{\ell}{L} & \frac{1}{r^4} \frac{\ell}{L} \\ -\frac{1}{r^4} \frac{a_k a_m \ell\epsilon_{3jk} \nabla_j (o_m)}{|\vec{a}/r - \vec{o}|^4} & \frac{1}{r^4} & \frac{1}{r^4} \\ +\frac{1}{r^3} \frac{a_k o_m \ell\epsilon_{3jk} \nabla_j (o_m)}{|\vec{a}/r - \vec{o}|^4} & \frac{1}{r^3} & \frac{1}{r^3} \\ -\frac{1}{r^4} \frac{o_k a_m \ell\epsilon_{3jk} \nabla_j (a_m)}{|\vec{a}/r - \vec{o}|^4} & \frac{1}{r^4} \frac{\ell}{L} & \frac{1}{r^4} \frac{\ell}{L} \\ +\frac{1}{r^3} \frac{o_k o_m \ell\epsilon_{3jk} \nabla_j (a_m)}{|\vec{a}/r - \vec{o}|^4} & \frac{1}{r^3} \frac{\ell}{L} & \frac{1}{r^3} \frac{\ell}{L} \\ +\frac{1}{r^3} \frac{o_k a_m \ell\epsilon_{3jk} \nabla_j (o_m)}{|\vec{a}/r - \vec{o}|^4} & \frac{1}{r^3} & \frac{1}{r^3} \\ -\frac{1}{r^2} \frac{o_k o_m \ell\epsilon_{3jk} \nabla_j (o_m)}{|\vec{a}/r - \vec{o}|^4} & \frac{1}{r^2} & \frac{1}{r^2} \\ -\frac{1}{r} \frac{a_k \ell\epsilon_{3jk} \nabla_j \left(\frac{f\ell}{s}\right)}{\frac{f\ell}{s} + \ell\epsilon_{3lm} \nabla_l o_m} & \frac{1}{r} \frac{1}{\text{Ro}_{\text{eq}}} \frac{\text{Ro}}{1+\text{Ro}} & \frac{1}{r} \frac{\text{Ro}}{\text{Ro}_{\text{eq}}} \\ -\frac{1}{r} \frac{a_k \ell\epsilon_{3jk} \nabla_j (\ell\epsilon_{3lm} \nabla_l o_m)}{\frac{f\ell}{s} + \ell\epsilon_{3lm} \nabla_l o_m} & \frac{1}{r} \frac{\text{Ro}}{1+\text{Ro}} & \frac{1}{r} \text{Ro} \\ +\frac{o_k \ell\epsilon_{3jk} \nabla_j \left(\frac{f\ell}{s}\right)}{\frac{f\ell}{s} + \ell\epsilon_{3lm} \nabla_l o_m} & \frac{1}{\text{Ro}_{\text{eq}}} \frac{\text{Ro}}{1+\text{Ro}} & \frac{\text{Ro}}{\text{Ro}_{\text{eq}}} \\ +\frac{o_k \ell\epsilon_{3jk} \nabla_j (\ell\epsilon_{3lm} \nabla_l o_m)}{\frac{f\ell}{s} + \ell\epsilon_{3lm} \nabla_l o_m} & \frac{\text{Ro}}{1+\text{Ro}} & \text{Ro} \end{array} \right) \quad (\text{C.18})$$

The leading order terms in W for the strong current case are

$$W = \frac{C_{Ds} \frac{\rho_a}{\rho_o} |\vec{a}/r - \vec{o}|}{\frac{f\ell}{s} + \ell\epsilon_{3lm} \nabla_l o_m} \left(\begin{array}{ccc} & \text{Scaled} & \text{Ro} \ll 1 \\ -\ell\epsilon_{3jk} \nabla_j o_k & 1 & 1 \\ +\frac{o_k \ell\epsilon_{3jk} \nabla_j \left(\frac{f\ell}{s}\right)}{\frac{f\ell}{s} + \ell\epsilon_{3lm} \nabla_l o_m} & \frac{1}{\text{Ro}_{\text{eq}}} \frac{\text{Ro}}{1+\text{Ro}} & \frac{\text{Ro}}{\text{Ro}_{\text{eq}}} \\ +\frac{o_k \ell\epsilon_{3jk} \nabla_j (\ell\epsilon_{3lm} \nabla_l o_m)}{\frac{f\ell}{s} + \ell\epsilon_{3lm} \nabla_l o_m} & \frac{\text{Ro}}{1+\text{Ro}} & \text{Ro} \end{array} \right) \quad (\text{C.19})$$

which include the same curl of the ocean velocity field found in the strong (but large scale) wind. The other two terms involve variation of planetary and relative vorticity perpendicular to the current direction.

D FRONT TRACKING

Tracking fronts is a common activity in oceanography. To that end it would be nice to extract a velocity from a set of crossing observations. You only need N observations to extract a N dimensional velocity but it is common to have more observations and an objective method for combining them is desirable. A similar method has been applied to acoustic Doppler current profilers (ADCP) by (Scotti et al., 2005), here I generalize the solution for use on an arbitrary planar front.

D.1 FRONT DEFINITION

To combine point measurements we must make assumptions about the geometry of the front, the simplest of these is that of a planar front. This is equivalent to assuming that the radius of curvature of the front is much larger than the size of observation array. Similarly we assume that the front travels at constant speed across the array of observations. With these assumption we can calculate the time at which the front crosses a point \vec{x}_i is given by

$$t_i + \tau_i = t_0 + \frac{\vec{x}_i \cdot \vec{u}}{\vec{u} \cdot \vec{u}} \quad (\text{D.1})$$

where t_0 is the time the front crosses the origin and τ_i is an error term. Taking the difference in arrival times between observations i , and j eliminates t_0 Re-indexing the differences Δt_k and $\Delta \vec{x}_k$ as a list allows this to be expressed as a matrix problem where $i = 1, 2, 3$ is the dimension and $k = 1, \dots, \frac{N(N-1)}{2}$ is the lag pair, also for simplicity introduce a reduced velocity $\vec{u}' = \frac{\vec{u}}{\vec{u} \cdot \vec{u}}$

$$\Delta t_k + \Delta \tau_k = \Delta x_{ki} u'_i \quad (\text{D.2})$$

Calculating the least square error estimate gives a matrix equation

$$u'_j = \Delta t_k \Delta x_{ik} (\Delta x_{jk} \Delta x_{ik})^{-1} \quad (\text{D.3})$$

where the velocity is recovered as $\vec{u} = \frac{\vec{u}'}{\vec{u}' \cdot \vec{u}'}$, assuming the matrix $\Delta x_{jk} \Delta x_{ik}$ has an inverse. With this in hand we can extract a front velocity \vec{u} from an arbitrary number of observations.

